Quantum Mechanical Wavepacket Calculations on Chemical Reactions

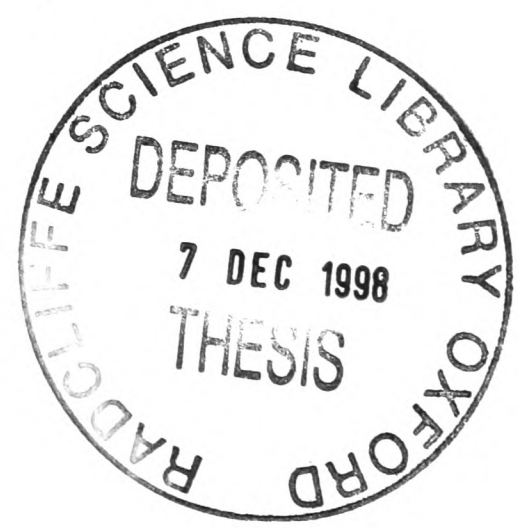
Bad. Copy

Caroline Russell

Lincoln College, Oxford

A thesis submitted in partial fulfilment of the requirements for the degree of Doctor of Philosophy of the University of Oxford

Trinity Term, 1998



Quantum mechanical wavepacket calculations on chemical reactions

Caroline Russell, Lincoln College

A thesis submitted in partial fulfilment of the requirements
for the degree of Doctor of Philosophy of the University of Oxford

Trinity Term, 1998

Abstract

The quantum mechanical time-dependent wavepacket method is introduced in the context of the field of chemical dynamics. The theory of the method is presented for two processes of interest in dynamics: molecular photodissociation, and reactive scattering. For the first of these processes, an expression is derived for the absorption spectrum of a molecule undergoing an electronic bound-continuum transition. For the second process, a time-dependent formulation is obtained for the S-matrix, and the "flux formulation" for the calculation of initial state-selected reaction probabilities (ISSRPs) is shown to be equivalent to summing over appropriate S-matrix elements.

The time-dependent wavepacket theory for molecular photodissociation is used in the calculation of the photodetachment spectrum of the FH_2^- anion. Spectra are calculated for two different energy resolutions, and previously unobserved structure is seen in the higher resolution spectrum. The structure is assigned by studying energy-dependent wavefunctions corresponding to each peak in the spectrum. Some peaks are assigned to direct scattering states, while others are assigned to quantum mechanical resonance states localised in the reactant and product valleys of the potential energy surface. The implication of this is that a high-resolution photodetachment experiment may provide the first experimental evidence for resonances in the $F + H_2$ reaction.

For reactive scattering, the time-dependent wavepacket method is used (in conjunction with the rotationally adiabatic approximation for $J > 0$ calculations) to calculate ISSRPs for various initial states of the nearly-thermoneutral ion-molecule reaction: $N^+(^3P)+H_2(^1\Sigma_g^+) \longrightarrow NH^+(X^2\Pi)+H(^2S)$. Dense resonance structure in the reaction probabilities for $J = 0$ is attributed to the influence of the deep wells in the potential energy surface for the reaction. The ISSRPs are used to calculate initial state-selected cross sections and rate constants which are compared with the results of some earlier trajectory calculations and with experimental data. The implications of the results for the astrophysical significance of the reaction are discussed.

Acknowledgements

I would like to thank my supervisor, Dr. David Manolopoulos, for his help and advice throughout my D.Phil..

I would also like to thank Prof. Mark Child for some useful discussions, Prof. Millard Alexander for allowing me time on his computers, and Prof. David Clary for suggesting the work on the $N^+ + H_2$ reaction.

It has been a pleasure to share an office with various colleagues over the last three years, and I would like to thank all the members of the Manolopoulos group for their company.

An EPSRC studentship is gratefully acknowledged.

Finally, I would like to express my sincere appreciation to my parents for supporting me throughout my education, and to Hans for all his encouragement.

Contents

1 Introduction **1**

1.1 Introduction to chemical dynamics 1

1.2 Theoretical methods in chemical dynamics 4

1.2.1 The Born-Oppenheimer approximation 4

1.2.2 Methods for dynamics calculations 7

1.3 The quantum mechanical time-dependent wavepacket method 8

1.3.1 Introduction 8

1.3.2 Previous applications 10

1.4 Structure of the thesis 14

2 Theory **16**

2.1 Quantum mechanical theory of molecular photodissociation 16

2.1.1 Fermi's Golden Rule 16

2.1.2 Bound-continuum transitions 17

2.1.3 The time-dependent wavepacket method 19

2.1.4 Photodissociation dynamics: recurrences and resonances 21

2.1.5 Summary 24

2.2 Quantum mechanical theory of chemical reactions 25

2.2.1 Introduction 25

2.2.2 A general expression for S-matrix elements 26

2.2.3 A time-dependent wavepacket formulation for the S-matrix 28

2.2.4 Causality argument applied to the S-matrix 29

2.2.5 The initial state-selected reaction probability (ISSRP) 31

2.2.6 The flux formulation for the ISSRP 32

2.2.7 Causality argument applied to the ISSRP 34

2.2.8 Summary 35

2.3 Approximate methods for higher total angular momenta 35

2.3.1 The initial state-selected reaction cross section 35

2.3.2 Translational energy dependence of the cross section 36

2.3.3 The initial state-selected rate constant 39

2.3.4 Introduction to higher total angular momenta 40

2.3.5 The centrifugal sudden (CS) approximation 40

2.3.6 The optimum centrifugal sudden (OCS) approximation 46

2.3.7 The rotationally adiabatic approximation (RAA) 48

2.3.8 Summary 50

2.4 Conclusions 50

3 Photodetachment Spectroscopy of FH_2^- 52

3.1 Anion photoelectron spectroscopy: "transition state spectroscopy" 52

3.2 The $F + H_2 \longrightarrow HF + H$ reaction 55

3.3 Method and computational details 59

3.3.1 Introduction 59

3.3.2 Methodology 60

3.3.3 Numerical details 65

3.4 Results: calculated photoelectron spectra 66

3.5 Analysis: energy-dependent wavefunctions 70

3.5.1 Method of analysis 70

3.5.2 Results and interpretation 71

3.6 Discussion: recent work on $F + H_2$ 80

3.7 Conclusions 83

4 Reactive Scattering Calculations on the $N^+ + H_2$ Reaction 85

4.1 The $N^+ + H_2 \longrightarrow NH^+ + H$ reaction 86

4.1.1 Introduction 86

4.1.2 Astrophysical significance 86

4.1.3 Chemistry literature 90

4.2 Method and computational details 96

4.2.1 Introduction 96

4.2.2 Methodology 98

4.2.3 Numerical details 114

4.3 Results and discussion 117

4.3.1 Initial state-selected reaction probabilities 117

4.3.2 Initial state-selected cross sections 123

4.3.3 Initial state-selected rate constants 129

4.3.4 Thermal rate constants 133

4.4 Conclusions 140

5 Summary 143

A Absorbing potentials 147

B Jacobi coordinates for a three-atom system 153

C Energy levels of an asymmetric top 155

References 158

Chapter 1 Introduction

1.1 Introduction to chemical dynamics

Chemical dynamics is the field which is concerned with the mechanism of elementary chemical processes on a molecular level [1]. The ultimate aim of this field is to understand chemical events in the gas phase *via* a study of the forces at work both within isolated molecules, and when atoms, ions and molecules interact with one another. In contrast to kinetics, in which one is interested simply in the rate of a particular process under a given set of conditions, the field of dynamics is concerned with a more detailed investigation into the way in which the process takes place.

Two areas which are of particular interest to chemical dynamicists are molecular photodissociation and reactive scattering. The first of these can be described schematically as

$$\mathrm{AB} \xrightarrow{h\nu} \mathrm{AB}^{\ddagger} \longrightarrow \mathrm{A} + \mathrm{B}, \tag{1.1}$$

where AB is a molecular species which dissociates upon the absorption of a photon of energy $h\nu$. This process is often termed a "half collision" event since the interesting nuclear dynamics is restricted to the splitting of the AB bond to form the fragments A and B. Questions which a dynamicist might ask about such a system could include "How long does $\mathrm{AB}^{\ddagger}$ exist before it falls apart to form A and B?", "Are the fragments A and B formed in rotationally or vibrationally excited states?", and "In what directions are the fragments A and B scattered, relative to the polarisation vector

of the electromagnetic radiation which caused the dissociation?".

It should be clear from these questions that in dynamics we are interested in *state-selected* quantities, rather than just an average over all the possible quantum states of the molecules. We might, for example, want to know the partial cross section [2] for photodissociation from an initial state i of AB (where i is a composite index representing all the quantum numbers of the molecule) into the final states j and k of the fragments A and B:

$$\mathrm{AB}(i) \xrightarrow{h\nu} \mathrm{AB}^{\ddagger} \longrightarrow \mathrm{A}(j) + \mathrm{B}(k). \tag{1.2}$$

Such a cross section would be described as a *state-to-state* photodissociation cross section. If, on the other hand, we were not interested in knowing the final states of the product fragments, but only in the total cross section from AB(i), this would be described as an *initial state-selected* cross section.

In contrast to molecular photodissociation, reactive scattering is described by

$$\mathrm{A} + \mathrm{BC} \longrightarrow \mathrm{ABC}^{\ddagger} \longrightarrow \mathrm{AB} + \mathrm{C}. \tag{1.3}$$

This is clearly a "full collision" event since the dynamics which must be understood consists both of the reactants coming together to form the "transition state", $\mathrm{ABC}^{\ddagger}$, and of the splitting of this entity to give the products, AB + C. The questions which might be asked about a reaction such as this could include "How does the probability of a reaction taking place when A and BC collide depend on their relative translational energy?", "Does the probability of reaction depend on the initial (for example, ro-vibrational) states of the reactants?", "Does the reaction proceed directly or *via* a long-lived complex of some sort?", and "How is energy distributed among the product molecules, AB and C?".

Again we see that we are interested in state-selected quantities. For the reaction

$$\mathrm{A}(i) + \mathrm{BC}(j) \longrightarrow \mathrm{ABC}^{\ddagger} \longrightarrow \mathrm{AB}(k) + \mathrm{C}(\ell), \tag{1.4}$$

we might, for example, be interested in the *state-to-state* reaction probability (the probability of reaction occurring between $\mathrm{A}(i)$ and $\mathrm{BC}(j)$ to form $\mathrm{AB}(k)$ and $\mathrm{C}(\ell)$), or on the other hand we might simply require a half state-selected quantity such as the *initial state-selected* reaction probability for which the final states of the product molecules are not specified.

Answers to questions in chemical dynamics, such as the examples given in this section, come from both experimental and theoretical research, and often progress can only be made when the two approaches are combined to solve a particular problem. In this thesis we focus on theoretical work, but it is hoped that the importance of experimental results will also become apparent.

The structure of the rest of this chapter is as follows. In section 1.2 we discuss the Born-Oppenheimer approximation in the context of dynamics calculations on chemical systems, and then give a brief overview of the different theoretical methods which can be used to carry out such calculations. We go on in section 1.3 to give a general description of the method used for the work presented in this thesis, the time-dependent wavepacket method, and to present some examples of earlier applications of the method. Finally, in section 1.4, we conclude the chapter with a short description of the structure of the rest of the thesis.

1.2 Theoretical methods in chemical dynamics

1.2.1 The Born-Oppenheimer approximation

The complete theoretical treatment of any chemical system, be it a molecule in isolation or a chemical reaction, requires the solution of the full Schrödinger equation for the system:

$$\mathcal{H}(\boldsymbol{x},\boldsymbol{y})|\Psi(\boldsymbol{x},\boldsymbol{y})\rangle = E|\Psi(\boldsymbol{x},\boldsymbol{y})\rangle, \tag{1.5}$$

where $\mathcal{H}(\boldsymbol{x},\boldsymbol{y})$ is the Hamiltonian for the system, $\boldsymbol{x}$ and $\boldsymbol{y}$ are the coordinates for the nuclei and the electrons respectively, $|\Psi(\boldsymbol{x},\boldsymbol{y})\rangle$ is the full wavefunction, and E is the eigenenergy.

Unfortunately, this equation cannot be solved for chemically-interesting systems without invoking an approximation. The standard method which is used exploits the different time scales of electronic and nuclear motion by assuming that when the nuclei in a system move, the electronic wavefunctions adjust almost instantaneously. This approximation, the well-known Born-Oppenheimer approximation, is made in the following way [3].

We begin by writing the full Hamiltonian as

$$\mathcal{H}(\boldsymbol{x},\boldsymbol{y}) = T^n(\boldsymbol{x}) + H^e(\boldsymbol{y},\boldsymbol{x}), \tag{1.6}$$

where $T^n(\boldsymbol{x})$ is the nuclear kinetic energy operator, and $H^e(\boldsymbol{y},\boldsymbol{x})$ is the electronic Hamiltonian (containing the electronic kinetic energy and the electronic and nuclear potential energy operators) at each value of the nuclear coordinates $\boldsymbol{x}$.

The full wavefunction from equation (1.5) can be expanded as

$$|\Psi(\boldsymbol{x},\boldsymbol{y})\rangle = \sum_k |\psi_k^e(\boldsymbol{y};\boldsymbol{x})\psi_k^n(\boldsymbol{x})\rangle, \tag{1.7}$$

where $|\psi_k^e(\boldsymbol{y};\boldsymbol{x})\rangle$ satisfies the electronic Schrödinger equation

$$H^e(\boldsymbol{y},\boldsymbol{x})|\psi_k^e(\boldsymbol{y};\boldsymbol{x})\rangle = V_k^e(\boldsymbol{x})|\psi_k^e(\boldsymbol{y};\boldsymbol{x})\rangle, \tag{1.8}$$

subject to the condition

$$\langle\psi_j^e(\boldsymbol{y};\boldsymbol{x})|\psi_k^e(\boldsymbol{y};\boldsymbol{x})\rangle_{\boldsymbol{y}} = \delta_{jk}, \tag{1.9}$$

and $V_k^e(\boldsymbol{x})$ is the kth adiabatic electronic potential energy surface for the system.

We proceed by substituting equation (1.7) into equation (1.5), and exploiting the orthonormality condition in equation (1.9), to yield the following set of coupled equations for the nuclear wavefunctions:

$$\sum_k \langle\psi_j^e(\boldsymbol{y};\boldsymbol{x})|T^n(\boldsymbol{x})|\psi_k^e(\boldsymbol{y};\boldsymbol{x})\psi_k^n(\boldsymbol{x})\rangle_{\boldsymbol{x}} + \left[V_j^e(\boldsymbol{x}) - E\right]|\psi_j^n(\boldsymbol{x})\rangle = 0. \tag{1.10}$$

This set of equations is exact, but is often too difficult to solve without making any approximations. In the Born-Oppenheimer approximation we assume that the electronic wavefunctions vary more slowly as a function of the nuclear coordinates than the nuclear wavefunctions, thus allowing us to ignore the derivatives of $|\psi_k^e(\boldsymbol{y};\boldsymbol{x})\rangle$ with respect to $\boldsymbol{x}$. In other words, the Born-Oppenheimer approximation removes the coupling of the nuclear wavefunctions to give

$$|\Psi(\boldsymbol{x},\boldsymbol{y})\rangle \approx |\psi_j^e(\boldsymbol{y};\boldsymbol{x})\psi_j^n(\boldsymbol{x})\rangle, \tag{1.11}$$

where

$$H_j^n(\boldsymbol{x})|\psi_j^n(\boldsymbol{x})\rangle = E|\psi_j^n(\boldsymbol{x})\rangle, \tag{1.12}$$

with

$$H_j^n(\boldsymbol{x}) = T^n(\boldsymbol{x}) + V_j^e(\boldsymbol{x}). \tag{1.13}$$

Equations (1.12) and (1.13) form the basis of the majority of dynamics calculations carried out to date, including the work presented in the subsequent chapters of this thesis. The approximation is appropriate for calculations on a system where the relevant adiabatic electronic potential energy surface, $V_j^e(\boldsymbol{x})$, is well separated in energy from all other surfaces of the same symmetry, but it can break down where this is not the case (for example around conical intersections), where so-called "multi-surface" effects become important. From this point on, however, we shall assume the applicability of the Born-Oppenheimer approximation, unless we explicitly state otherwise.

It is clear from this discussion that the work involved in carrying out a calculation on a chemical system is divided into two main stages:

- An *ab initio* calculation to solve the Schrödinger equation for the electrons for fixed positions of the nuclei (equation (1.8)), in order to obtain an adiabatic electronic potential energy surface, $V_j^e(\boldsymbol{x})$,
- Solution of the Schrödinger equation for the nuclear motion on the potential energy surface (equation (1.12)) to obtain the dynamical information.

The first of these constitutes the field of "electronic structure" calculations [4], and is outside the scope of this thesis. We shall concentrate here solely on the second stage of the process, the (nuclear) dynamics calculation, which is carried out once an appropriate electronic potential energy surface has been obtained.

1.2.2 Methods for dynamics calculations

A very wide range of methods can be used to carry out dynamics calculations on chemical systems. Classes of methods include statistical [5, 6], quasi-classical trajectory [7, 8, 9], semiclassical [10, 11], and fully quantum mechanical techniques [12, 13, 14, 15]. These vary in the level of approximation they make, and consequently in the expense of the calculations they entail. The work in this thesis uses a method which falls into the class of the "most exact" methods – a fully quantum mechanical treatment of the nuclear dynamics – and consequently we shall limit this introductory discussion to methods of this type.

Quantum mechanical methods for dynamics calculations (with a time-independent Hamiltonian) can themselves be divided into two categories [13]. Time-independent methods consist of solving the time-independent Schrödinger equation given in equation (1.12), which in simplified notation is

$$H\psi = E\psi, \tag{1.14}$$

while time-dependent methods solve the time-dependent Schrödinger equation

$$i\hbar\frac{\partial\psi}{\partial t} = H\psi. \tag{1.15}$$

These are entirely equivalent mathematically, but for a particular application one may be preferable to the other for reasons of ease of implementation.

Within the time-independent framework for dynamics calculations there exists a large variety of methods. For bound state calculations these methods essentially involve setting up the Hamiltonian matrix in an appropriate basis (with the correct boundary conditions) and then diagonalising it to obtain the eigenstates of the

system, while for scattering and photodissociation calculations they involve setting up the matrix of the operator $(E+i\epsilon-H)^{-1}$ and operating with it on an appropriate initial state vector. General reviews of time-independent methods can be found in references [13] and [14]; suffice it to say here that, for chemical systems, the coupled-channel method has been the most popular to date.

The calculations presented in the subsequent chapters of this thesis use a time-dependent quantum mechanical method: the time-dependent wavepacket method. The theoretical basis of this method, with particular reference to molecular photodissociation and reactive scattering, is presented in chapter 2. In the next section, however, we give a general description of the method, and then demonstrate its power and flexibility by giving a review of some of the interesting applications of the method which have already been reported in the chemical dynamics literature.

1.3 The quantum mechanical time-dependent wavepacket method

1.3.1 Introduction

As described in the previous section, the time-dependent wavepacket method involves solving the time-dependent Schrödinger equation (equation (1.15)) for the nuclear motion of a particular chemical system. This is a first-order differential equation in time, and for a time-independent Hamiltonian the formal solution is

$$\psi(t+\Delta t) = e^{-iH\Delta t/\hbar}\psi(t). \tag{1.16}$$

It is thus clear that in order to obtain the wavefunction $\psi(t+\Delta t)$ it is simply necessary to operate on $\psi(t)$ with the time-evolution operator, $e^{-iH\Delta t/\hbar}$.

Although the benchmark reaction, $OH + H_2$, has dominated the literature on time-dependent studies of four-atom reactions so far, some other systems are now also starting to attract interest. Two such examples are

$$HO + CO \longrightarrow H + CO_2, \tag{1.21}$$

for which both four-dimensional [64] and five-dimensional [65] calculations have been carried out, and

$$H_2 + CN \longrightarrow HCN + H, \tag{1.22}$$

which has very recently been studied in its full six internal (vibrational) dimensions [66].

Other applications

In addition to the applications described above, the time-dependent wavepacket method is also proving itself to be useful for calculations on several other types of dynamical phenomenon, for example vibrational predissociation [67, 68], and gas-surface reactions [15]. In the latter of these fields, the most exciting development is that it has recently become possible to carry out full six-dimensional calculations on the dissociative chemisorption of H_2 on copper surfaces [69, 70, 71].

In summary, we have given in this section a general introduction to the quantum mechanical time-dependent wavepacket method, and then described some recent applications of this method to problems in chemical dynamics.

1.4 Structure of the thesis

The structure of the remaining chapters of the thesis is as follows. In chapter 2, we derive the quantum mechanical time-dependent theory of the two chemical pro-

of the initial wavepacket will obviously be determined by the quantum state of the dissociating molecule. However, for a calculation on a reaction such as that in equation (1.4), we can construct the initial wavepacket to describe whatever initial quantum states of the reactants we are interested in. In addition to this, the initial wavepacket can be chosen to contain as wide or as narrow a range of relative translational energy of the reactants as desired (although there may be practical considerations which must be taken into account – see later). Because of this, dynamics information can be obtained over a whole range of energies from just one wavepacket propagation.

Time-dependent methods lend themselves particularly easily to the calculation of initial state-selected quantities for which one is not interested in the final state of the products. This point will be demonstrated in chapter 2, where the flux formulation for the calculation of initial state-selected reaction probabilities will be presented. However, in addition to being able to provide half state-selected quantities, the time-dependent wavepacket method can also be used to calculate state-to-state quantities. This is achieved simply by using an appropriate method of analysis in the third step of the calculation procedure. Examples of both half state-selected and state-to-state calculations that have been performed previously using the time-dependent wavepacket method will be given in the next section.

1.3.2 Previous applications

A recent review by Balakrishnan, Kalyanaraman and Sathyamurthy [15] has provided an extremely thorough account of the application of the time-dependent quantum mechanical approach to reactive scattering and related processes. For the pur-

poses of this thesis we shall not try to provide such a comprehensive description of every application, but rather to give some illustrative examples in order to show what has been achieved using this method thus far.

Photodissociation

The time-dependent approach to studying dynamical phenomena has proved extremely important in the field of photodissociation. The early work in this area was largely due to Heller [16, 17, 18, 19], who developed a *semiclassical* time-dependent method for calculating the absorption spectra for both bound and dissociative systems. The time-dependent method is ideal for the latter of these applications because it removes the need to calculate full reactive scattering wavefunctions in order to obtain photodissociation absorption spectra, and it also provides a physically-appealing framework within which to interpret the dynamics. Although we are concerned here with the *quantum mechanical* time-dependent method, the essence of the method is the same as in Heller's original formulation.

The quantum mechanical time-dependent method has been applied to an extremely large number of photodissociation problems [2, 15]. Calculations have been carried out both on a single potential energy surface and on coupled surfaces, and the method has become the standard way for tackling these calculations owing to the ease with which it can be implemented. Some examples of systems which have been studied recently in this way (including both initial state-selected and state-to-state studies) are the photodissociation of H_2O [20, 21, 22, 23, 24], O_3 [25, 26, 27, 28], HCO [29, 30], HOCl [31, 32, 33, 34], CH_2 [35, 36, 37, 38] and H_2O_2 [39, 40].

Three-atom reactions

We now move on to discuss reactive scattering calculations. Until the mid-1980s it was only possible to apply the time-dependent wavepacket method to collinear collisions of atoms and diatoms, and the H + H_2 reaction was the benchmark system for this early work [41]. However, a great deal of progress has been made since then, both because of improvements in the methods which are used, and also of course because of the increase in computer processing power.

Of the large number of recent applications of the time-dependent wavepacket method to atom-diatom reactions, probably the most significant was the work by Zhang and Zhang on the reaction

$$H(^2S) + O_2(^3\Sigma_g^-) \longrightarrow OH(^2\Pi) + O(^3P), \tag{1.17}$$

which was the first successful study of a reaction which has a deep well on its potential energy surface [42]. Prior to this study it was believed that time-dependent methods were only suitable for "direct" reactions for which converged results could be obtained within a relatively short propagation time, but Zhang and Zhang showed that it is possible to obtain converged initial state-selected reaction probabilities even when there are resonances with picosecond lifetimes to contend with. In subsequent studies on the same system, Dai and Zhang have successively calculated both state-to-state quantities [43], and bound and resonance state energies [44].

Other time-dependent wavepacket calculations which have been carried out recently on atom-diatom reactions include studies of the reaction

$$Li + HF \longrightarrow LiF + H, \tag{1.18}$$

by Gögtas *et al.* [45], and Zhu *et al.* [46], and also the reaction

$$O(^1D) + H_2 \longrightarrow OH + H, \tag{1.19}$$

which has been studied by Peng *et al.* [47], and Dai [48]. All of these calculations prove the effectiveness of using the time-dependent wavepacket method for reactions involving long-lived resonances.

Four-atom reactions

The last couple of years have seen the first exact quantum mechanical calculations on four-atom reactions, and the time-dependent wavepacket method has emerged as the preferred approach for such calculations due to its favourable scaling with the size of the system [15, 42, 49].

The benchmark reaction for four-atom systems is

$$OH + H_2 \longrightarrow H + H_2O, \tag{1.20}$$

which has also attracted many time-independent calculations [50, 51]. In the realm of time-dependent calculations, it was studied initially in calculations with reduced dimensionality [52, 53], and subsequently in its full dimensionality (six mathematical dimensions) [54, 55, 56, 57]. Both initial state-selected [52, 53, 54, 55] and state-to-state [56, 57] reaction probabilities have been calculated, although to date the state-to-state calculations have only been carried out for total angular momentum $J = 0$. Studies on variants of this reaction have included five-dimensional calculations of initial state-selected reaction probabilities for HD + OH [58, 59] and D_2 + OH [60], and six-dimensional calculations on the reverse reaction, H + H_2O [61, 62], and its isotopic variant, H + HOD [63].

Although the benchmark reaction, $OH + H_2$, has dominated the literature on time-dependent studies of four-atom reactions so far, some other systems are now also starting to attract interest. Two such examples are

$$HO + CO \longrightarrow H + CO_2, \tag{1.21}$$

for which both four-dimensional [64] and five-dimensional [65] calculations have been carried out, and

$$H_2 + CN \longrightarrow HCN + H, \tag{1.22}$$

which has very recently been studied in its full six internal (vibrational) dimensions [66].

Other applications

In addition to the applications described above, the time-dependent wavepacket method is also proving itself to be useful for calculations on several other types of dynamical phenomenon, for example vibrational predissociation [67, 68], and gas-surface reactions [15]. In the latter of these fields, the most exciting development is that it has recently become possible to carry out full six-dimensional calculations on the dissociative chemisorption of H_2 on copper surfaces [69, 70, 71].

In summary, we have given in this section a general introduction to the quantum mechanical time-dependent wavepacket method, and then described some recent applications of this method to problems in chemical dynamics.

1.4 Structure of the thesis

The structure of the remaining chapters of the thesis is as follows. In chapter 2, we derive the quantum mechanical time-dependent theory of the two chemical pro-

cesses which are of interest in this work: molecular photodissociation, and reactive scattering. For molecular photodissociation we derive an expression for the absorption spectrum of a system undergoing a bound-continuum transition. For reactive scattering we derive expressions for the S-matrix and for the initial state-selected reaction probability, and show how the latter can be used to obtain initial state-selected cross sections and rate constants. We end the chapter with a discussion of some commonly-used approximations for reactive scattering calculations with total angular momentum $J > 0$.

Chapter 3 is concerned with the field of anion photodetachment spectroscopy. We use the photodissociation theory described in chapter 2 to calculate the photoelectron spectrum of the FH_2^- anion at two different energy resolutions. The structure in the higher-resolution spectrum is assigned using a wavepacket technique, and the results are discussed with particular reference to quantum mechanical resonance states.

In chapter 4, we apply the quantum mechanical theory of reactive scattering which was derived in chapter 2 to the ion-molecule reaction

$$N^+(^3P) + H_2(^1\Sigma_g^+) \longrightarrow NH^+(X^2\Pi) + H(^2S).$$

In particular, we present initial state-selected reaction probabilities, cross sections, and rate constants, and compare our results with an earlier QCT calculation and with experimental data. We discuss our findings in the light of the astrophysical significance of the reaction.

Finally, chapter 5 provides a brief summary of the work which is presented in this thesis.

Chapter 2 Theory

In the introduction to the thesis we have motivated the use of the quantum mechanical time-dependent wavepacket method in the context of gas-phase chemical dynamics. The purpose of the present chapter is to present the theory underlying this method, and thus to provide the basis for all of the work presented in the subsequent chapters of the thesis.

The chapter is divided into four sections. In section 2.1, we present the quantum mechanical theory underlying molecular photodissociation; this is relevant to the work in chapter 3 on the photodetachment spectrum of FH_2^-. In section 2.2, we outline the quantum mechanical theory of reactive scattering, while in section 2.3 we introduce approximate methods that can be used in reactive scattering calculations for higher total angular momenta, $J > 0$. These two sections are relevant to the work in chapter 4 on the $N^+ + H_2$ reaction. Finally, section 2.4 contains some brief conclusions.

2.1 Quantum mechanical theory of molecular photodissociation

2.1.1 Fermi's Golden Rule

The starting point for the discussion of the theory of molecular photodissociation is the Fermi Golden Rule [72] expression for the absorption cross section of a species undergoing an electronic transition within the Born-Oppenheimer approximation

[2],

$$\sigma_i(\omega) = \frac{\pi\omega}{\hbar\epsilon_0 c}\sum_f \delta(\omega - \omega_{fi})|\langle\psi_f|\boldsymbol{\mu}_{fi}\cdot\mathbf{e}|\psi_i\rangle|^2. \tag{2.1}$$

In this expression, $\sigma_i(\omega)$ is the absorption cross section for transitions from the specified initial state $|\psi_i\rangle$ as a function of frequency ω, $|\psi_i\rangle$ and $|\psi_f\rangle$ are the initial and final ro-vibrational wavefunctions of the molecule, ω_{fi} is the frequency of the transition from $|\psi_i\rangle$ to $|\psi_f\rangle$, $\boldsymbol{\mu}_{fi}$ is the electric dipole transition matrix element for the electronic transition, and $\mathbf{e}$ is a unit vector in the direction of the electric field of the radiation. Complete derivations of equation (2.1) can be found in references [2] and [3], but in brief it requires a consideration of the interaction of the light (treated as a classical electromagnetic wave) with a gas molecule (treated quantum mechanically), and the following approximations go into the derivation:

- First order perturbation theory is used to treat the light-molecule interaction (this is a good approximation for the case in which the intensity of the light is not too high), and only the electric dipole interaction is considered.
- The light is treated as a classical electromagnetic wave, and its wavelength is assumed to be much larger than the dimensions of the molecule.
- The duration of the perturbation of the molecule by the light is assumed to be long enough for the molecule to experience a periodically-oscillating electric field.
- It is assumed that only one initial quantum state $|\psi_i\rangle$ is populated when the perturbation is switched on.

2.1.2 Bound-continuum transitions

In order to apply equation (2.1) to bound-continuum transitions (*i.e.*, to molecular photodissociation) as well as to bound-bound transitions, it is necessary to ma-

nipulate the right-hand side in such a way as to eliminate the discrete sum over final states [3]. The first step towards achieving this is to use the relationship between energy and angular frequency, $E = \hbar\omega$, along with the definition of the delta function,

$$f(x_0) = \int_{-\infty}^{+\infty} \delta(x - x_0) f(x) dx, \tag{2.2}$$

to replace the delta function in ω with one in E. Thus

$$\delta(\omega - \omega_{fi}) = \hbar\delta(E - E_{fi}), \tag{2.3}$$

which gives

$$\sigma_i(\omega) = \frac{\pi\omega}{\epsilon_0 c} \sum_f \delta(E - E_{fi}) |\langle\psi_f|\boldsymbol{\mu}_{fi} \cdot \mathbf{e}|\psi_i\rangle|^2. \tag{2.4}$$

If the zero of the energy scale is chosen to be E_i, the energy of the initial state, we obtain

$$\sigma_i(\omega) = \frac{\pi\omega}{\epsilon_0 c} P_i(E), \tag{2.5}$$

where

$$P_i(E) = \sum_f \langle\chi_i|\psi_f\rangle\delta(E - E_f)\langle\psi_f|\chi_i\rangle, \tag{2.6}$$

with

$$|\chi_i\rangle = \boldsymbol{\mu}_{fi} \cdot \mathbf{e}|\psi_i\rangle. \tag{2.7}$$

From equation (2.5) it is clear that the absorption cross section, $\sigma_i(\omega)$, is proportional to ω multiplied by an absorption spectrum, $P_i(E)$, and from this point on we shall concentrate on the absorption spectrum so as to avoid carrying the constant of proportionality.

It now remains to convert the expression for $P_i(E)$ in equation (2.6) into a form which does not require a discrete sum over final states. This can be done simply by

identifying the quantity

$$\sum_f |\psi_f\rangle\delta(E-E_f)\langle\psi_f| \tag{2.8}$$

as the spectral representation of the delta function $\delta(E-H)$, where H is the Hamiltonian for nuclear motion on the final Born-Oppenheimer potential energy surface V_f^e. However, this identification involves a mathematical subtlety associated with the fact that spectral representations are only properly defined for a certain class of functions (including in particular all functions $f(H)$ which have convergent power series expansions). Since the delta function $\delta(E-H)$ does not belong to this class, one must replace it with the limit of a pre-limit delta function, $\delta_\epsilon(E-H)$, which *does* have a convergent expansion [3]. Hence

$$\sum_f |\psi_f\rangle\delta(E-E_f)\langle\psi_f| = \lim_{\epsilon\to 0}\delta_\epsilon(E-H), \tag{2.9}$$

and thus

$$P_i(E) = \lim_{\epsilon\to 0}\langle\chi_i|\delta_\epsilon(E-H)|\chi_i\rangle. \tag{2.10}$$

Equation (2.10) achieves the goal set out at the beginning of this section; namely, to obtain an expression for the absorption spectrum which does not involve a discrete sum over final states, and which can therefore be used to treat bound-continuum (photodissociation) problems as well as bound-bound transitions.

2.1.3 The time-dependent wavepacket method

The choice of representation for $\delta_\epsilon(E-H)$ determines the method used to calculate the absorption spectrum $P_i(E)$, and it is possible to use either a time-independent or a time-dependent method [3]. Since the work presented in this thesis focuses exclusively on the time-dependent method, it is this formulation that we shall now discuss.

One of the best-known representations of the delta function is the Fourier representation,

$$\delta(E-H)=\frac{1}{2\pi\hbar}\int_{-\infty}^{+\infty}e^{+i(E-H)t/\hbar}dt, \tag{2.11}$$

for which the most physically-illuminating pre-limit version is,

$$\delta_\epsilon(E-H)=\frac{1}{\pi\hbar}\mathrm{Re}\int_{0}^{+\infty}e^{+i(E+i\epsilon-H)t/\hbar}dt. \tag{2.12}$$

Substituting this expression into equation (2.10) yields an expression for the absorption spectrum which shows it to be the half Fourier transform of an autocorrelation function [17, 73]:

$$P_i(E)=\lim_{\epsilon\to 0}\frac{1}{\pi\hbar}\mathrm{Re}\int_{0}^{\infty}e^{+iEt/\hbar}C_i(t)dt, \tag{2.13}$$

where

$$C_i(t)=\langle\chi_i(0)|\chi_i(t)\rangle, \tag{2.14}$$

and $|\chi_i(t)\rangle$ is the time-dependent wavepacket obtained by acting on $|\chi_i\rangle\equiv|\chi_i(0)\rangle$ with the propagator $e^{-i(H-i\epsilon)t/\hbar}$,

$$|\chi_i(t)\rangle=e^{-i(H-i\epsilon)t/\hbar}|\chi_i(0)\rangle. \tag{2.15}$$

Equation (2.13) shows that in order to calculate an absorption spectrum we need to know the appropriate initial wavefunction for the unexcited species. The Franck-Condon principle is then invoked to project this wavefunction vertically upwards onto the upper Born-Oppenheimer electronic potential energy surface. The main part of the calculation consists of the propagation of $|\chi_i(0)\rangle$ (the product of the electric dipole transition matrix element with the initial wavefunction) forwards in time. A schematic diagram to illustrate this process is given in figure 2.1. The autocorrelation function $C_i(t)$ is calculated during the propagation, and this can subsequently be Fourier transformed to give $P_i(E)$ as shown above. The integral

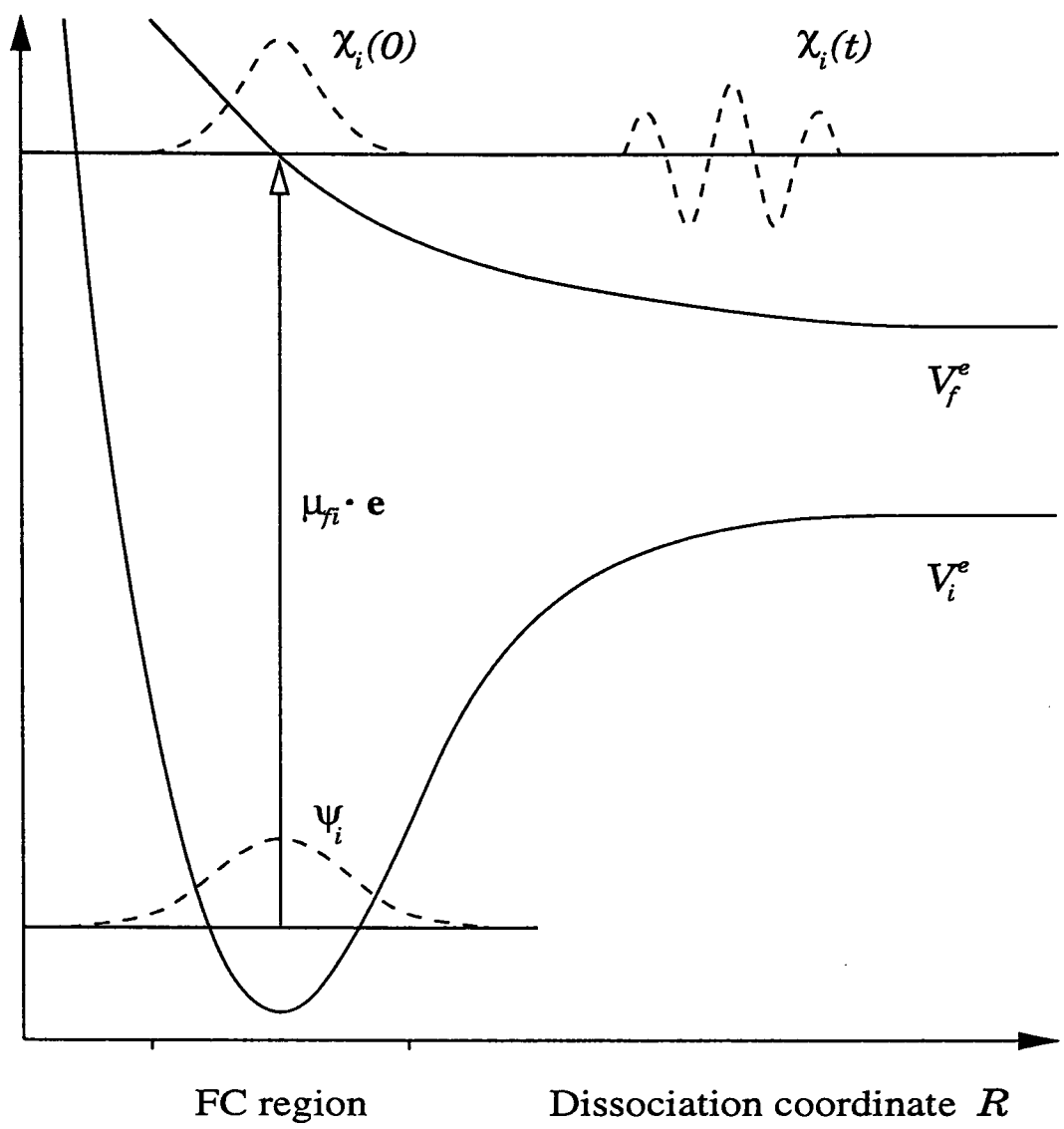


Figure 2.1 The time-dependent simulation of a photodissociation event.

in equation (2.13) is bound to converge due to the presence of the small but finite term involving ϵ which effectively multiplies the wavepacket by a damping factor at each time step of the propagation. Further details are given concerning this term in appendix A; suffice it to say here that in our calculations ϵ is interpreted as a coordinate-dependent operator commonly referred to as an "optical potential" or "absorbing potential".

2.1.4 Photodissociation dynamics: recurrences and resonances

Photodissociation dynamics can be discerned from a study of either $C_i(t)$ or $P_i(E)$. Let $|C_i(0)|$ be the modulus of the autocorrelation function at time $t = 0$. As the propagation begins, the wavepacket moves around the excited electronic potential

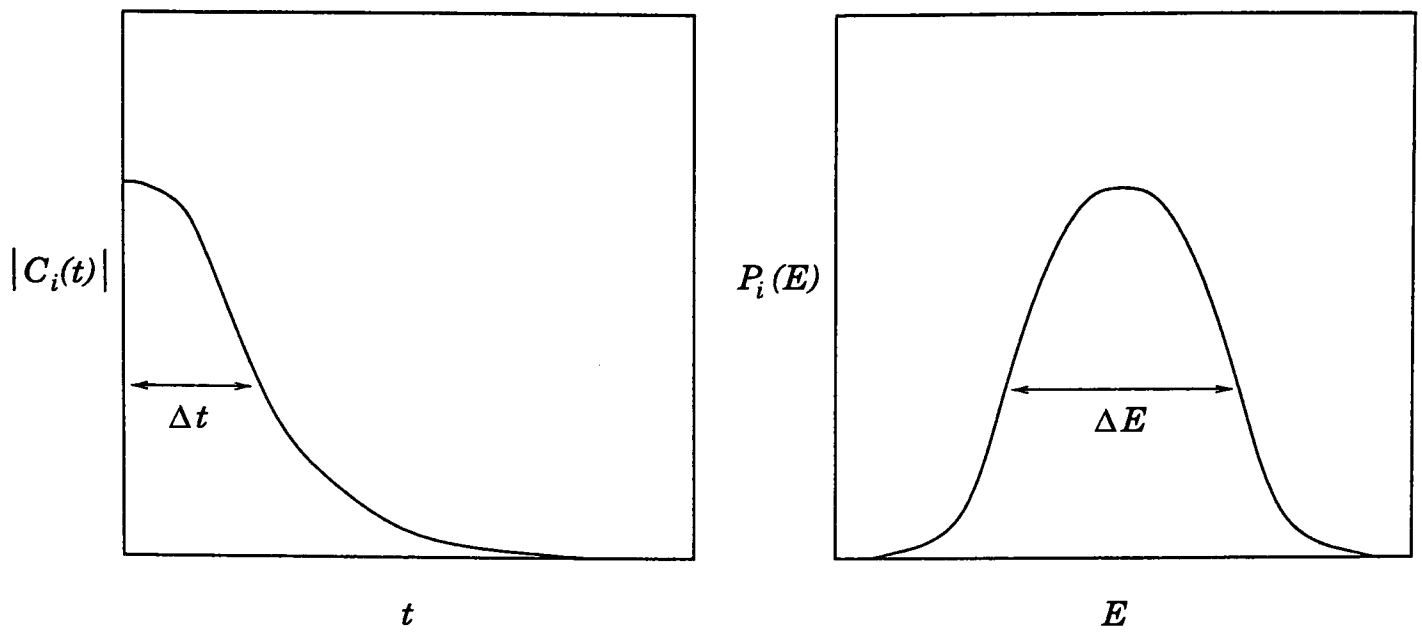


Figure 2.2 Behaviour of $|C_i(t)|$ and $P_i(E)$ for a system undergoing direct photodissociation.

energy surface and away from its initial position, hence $|C_i(t)|$ decreases. At all times $t > 0$ the value of $|C_i(t)|$ will be between zero and $|C_i(0)|$, but it may increase and decrease depending on the dynamics. The exact behaviour of $C_i(t)$ is thus indicative of the dynamics of the particular photodissociation event, and of course this is also manifested in the absorption spectrum $P_i(E)$. Some examples of different possible behaviours are discussed below.

The first example is the case of direct photodissociation. In this case the value of $|C_i(t)|$ decreases monotonically from $|C_i(0)|$ to zero and then remains at zero. In other words, the wavepacket leaves the Franck-Condon region and never returns. This is illustrated in figure 2.2 where one sees that the absorption spectrum of a direct photodissociation event is just one broad peak, the width of which is related to the speed with which the correlation function decreases from $|C_i(0)|$ to zero.

In contrast to direct photodissociation, consider next the case of a bound-bound electronic transition. The absorption spectrum corresponding to this is the well-known Franck-Condon spectrum of infinitely narrow lines at the energies of the

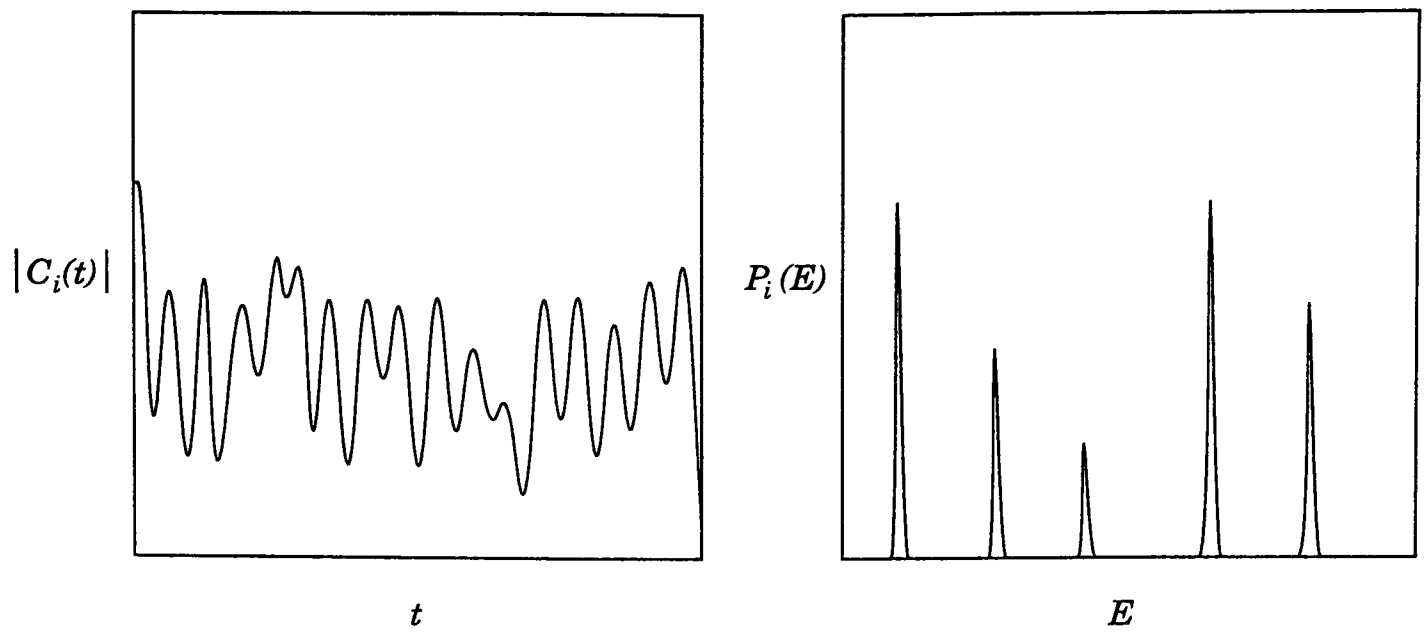


Figure 2.3 Behaviour of $|C_i(t)|$ and $P_i(E)$ for a system undergoing a bound-bound electronic transition.

bound states of the upper potential energy surface. The intensities of the lines reflect the Franck-Condon factors, and an illustration of such a spectrum is given in figure 2.3. In the case of a bound-bound transition, the value of $|C_i(t)|$ is again $|C_i(0)|$ at $t = 0$ and again decreases as the wavepacket leaves the Franck-Condon region. However, since the wavepacket is being propagated on a perfectly bound potential energy surface there is no way it can escape, thus it is reflected off the potential walls and parts of it come back periodically to the Franck-Condon region. This phenomenon is manifested in peaks known as "recurrences" in the modulus of the autocorrelation function, whose periodicity may reflect "periodic orbits" of the wavepacket as it moves on the upper potential energy surface. For a perfectly bound system, the oscillations in the correlation function continue to infinity, thus generating an absorption spectrum with infinitely narrow lines.

The final example to be considered is the case which is intermediate between those of direct photodissociation and bound-bound electronic spectroscopy, and is termed "indirect photodissociation". In this case the modulus of the autocorrelation function again decreases from $|C_i(0)|$ as the propagation begins. However, for indirect

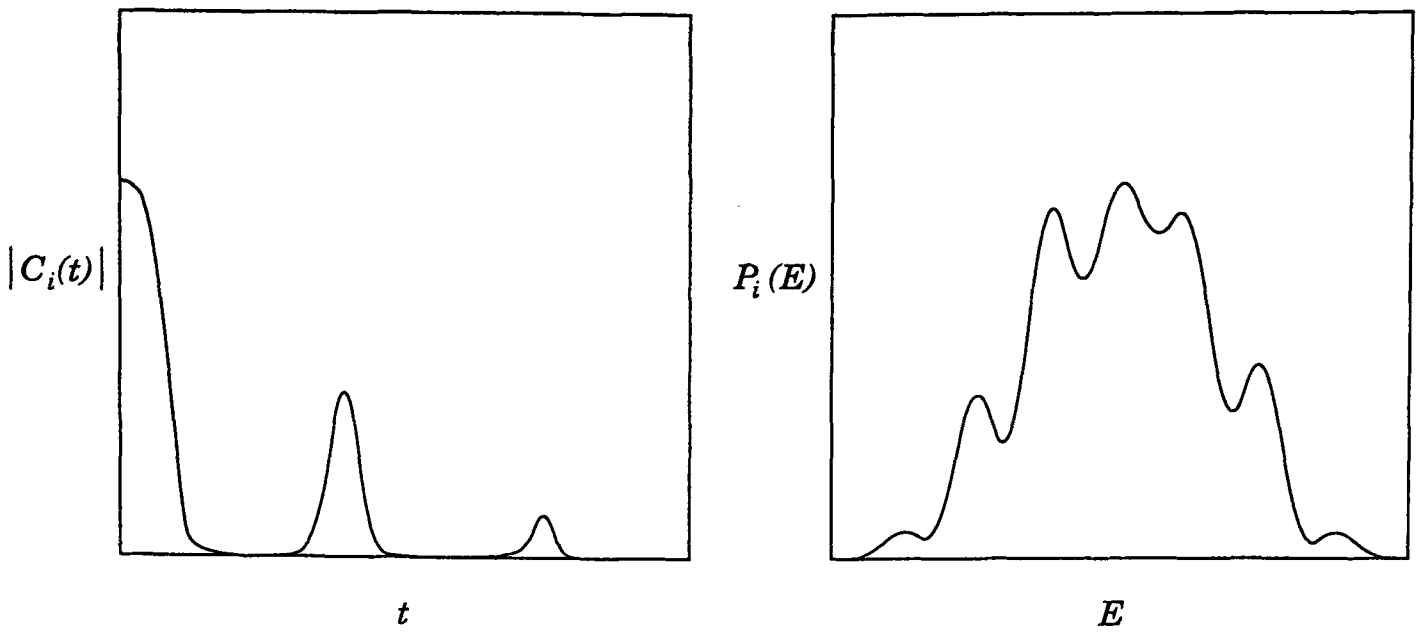


Figure 2.4 Behaviour of $|C_i(t)|$ and $P_i(E)$ for a system undergoing indirect photodissociation.

photodissociation, *some* of the wavepacket leaves the Franck-Condon region never to return (as in the case of direct photodissociation) but *some* of the wavepacket is trapped in quasi-bound "resonances" on the potential energy surface, and thus finds its way back to the Franck-Condon region. The periodicity with which this occurs is again associated with the presence of (possibly unstable) periodic orbits on the upper surface. The absorption spectrum corresponding to this process shows a broad overall structure due to the directly dissociating component but has narrower structure superimposed onto the broad structure which reflects the influence of the resonance states. Figure 2.4 gives a schematic illustration of $|C_i(t)|$ and $P_i(E)$ for this case. Quasi-bound resonance states play an extremely important rôle in the work presented in the subsequent chapters of this thesis, and will thus be discussed in greater detail later.

2.1.5 Summary

In summary, we have presented in this section a derivation of the time-dependent expression for the absorption spectrum of a system undergoing molecular photodis-

sociation from a specified initial quantum state $|\psi_i\rangle$ (equations (2.10) and (2.13)). It has been shown that the dynamics of the photodissociation can be understood either by studying the behaviour of the autocorrelation function, $C_i(t)$, or by studying the absorption spectrum, $P_i(E)$. The choice of which of these two to look at will depend on the system under study; for some systems it is more enlightening to think of the dynamics in terms of periodic orbits so that $C_i(t)$ is more useful, while for others it is more appropriate to consider the quasi-bound resonance states of the system and for such systems the absorption spectrum $P_i(E)$ is more informative.

The ideas presented in this section will be used extensively in chapter 3 which deals with the photodetachment spectrum of the FH_2^- anion. For now, however, we shall turn our attention to the theory of reactive scattering which is the other main area of interest in this thesis.

2.2 Quantum mechanical theory of chemical reactions

2.2.1 Introduction

The ultimate goal of the quantum mechanical theory of reactive scattering is the calculation of the "S-matrix" or "scattering matrix". The elements of this matrix, $S_{\mathbf{pr}}(E)$, are quantum mechanical probability amplitudes, and thus the square modulus of an element, $|S_{\mathbf{pr}}(E)|^2$, gives the probability of a transition at energy E (and also implicitly at the conserved angular momentum quantum number J) from an initial channel $\mathbf{r}$ of the reactants to a final channel $\mathbf{p}$ of the products. Once the S-matrix for a particular reaction is known for a large enough number of energies E (and also for sufficiently many values of J), all other quantities such as cross sections and rate constants can be calculated for the reaction using well-established

formulae [74, 75].

We shall begin this section by deriving an expression for the S-matrix element, $S_{\mathbf{pr}}(E)$, and showing how it can be calculated within a time-dependent formulation. Particular emphasis is placed on the importance of causality arguments in the derivation. We shall then proceed to define the initial state-selected reaction probability (ISSRP), and to show how the ISSRP can be expressed in terms of a "flux operator". The overall aim of this section is thus to develop the theory which will be used in the wavepacket calculations described in chapter 4.

2.2.2 A general expression for S-matrix elements

Although we ultimately want a time-dependent expression for the S-matrix, the simplest derivation is based on the time-independent scattering eigenstates $|\psi^+_{E\mathbf{r}}\rangle$ [76, 77]. These eigenstates satisfy the time-independent Schrödinger equation

$$H|\psi^+_{E\mathbf{r}}\rangle = E|\psi^+_{E\mathbf{r}}\rangle, \tag{2.16}$$

subject to the following asymptotic boundary condition in each open scattering channel $\mathbf{p}$:

$$\langle\phi_{\mathbf{p}}|\psi^+_{E\mathbf{r}}\rangle = \langle\phi_{\mathbf{p}}|\phi^-_{E\mathbf{p}}\rangle\delta_{\mathbf{pr}} - \langle\phi_{\mathbf{p}}|\phi^+_{E\mathbf{p}}\rangle S_{\mathbf{pr}}(E). \tag{2.17}$$

Here, $|\phi_{\mathbf{p}}\rangle$ is a localised (energy-independent) wavepacket in the asymptotic region of channel $\mathbf{p}$ and $S_{\mathbf{pr}}(E)$ is a scattering matrix element. The purely incoming and outgoing wavefunctions $|\phi^-_{E\mathbf{p}}\rangle$ and $|\phi^+_{E\mathbf{p}}\rangle$ in equation (2.17) can be chosen to have the form

$$\langle R_{\mathbf{p}}, \mathbf{x}_{\mathbf{p}}|\phi^\pm_{E\mathbf{p}}\rangle = h^\pm_{E\mathbf{p}}(R_{\mathbf{p}})\Phi_{\mathbf{p}}(\mathbf{x}_{\mathbf{p}}), \tag{2.18}$$

where

$$h^\pm_{E\mathbf{p}}(R_{\mathbf{p}} \to \infty) = v_{\mathbf{p}}^{-\frac{1}{2}} e^{\pm i(k_{\mathbf{p}}R_{\mathbf{p}} - l_{\mathbf{p}}\pi/2)}, \tag{2.19}$$

are velocity-normalised incoming and outgoing wavefunctions in the asymptotic region of channel $\mathbf{p}$, $k_{\mathbf{p}}$ is the asymptotic wave-vector, $v_{\mathbf{p}} = \hbar k_{\mathbf{p}}/\mu_{\mathbf{p}}$ is the asymptotic velocity, $l_{\mathbf{p}}$ is the orbital angular momentum quantum number, and $\Phi_{\mathbf{p}}(\mathbf{x_p})$ is the internal channel eigenstate (with $\mathbf{x_p}$ representing the coordinates for internal motion) in channel $\mathbf{p}$. Given this choice, it follows from the completeness of the scattering eigenstates $|\psi^+_{E\mathbf{c}}\rangle$ that the microcanonical density operator $\delta(E-H)$ can be written as [76, 77]

$$\delta(E-H) = \frac{1}{2\pi\hbar}\sum_{\mathbf{c}} |\psi^+_{E\mathbf{c}}\rangle\langle\psi^+_{E\mathbf{c}}|, \tag{2.20}$$

where the sum is over all channels $\mathbf{c}$ (including $\mathbf{r}$ and $\mathbf{p}$), and the density of states is equal to $2\pi\hbar$.

Now suppose that $|\phi_{\mathbf{p}}\rangle$ is a *purely outgoing* wavepacket without any incoming-wave component at any energy:

$$\langle\phi_{\mathbf{p}}|\phi^-_{E\mathbf{p}}\rangle = 0. \tag{2.21}$$

Substituting equation (2.21) into equation (2.17) leads to the following expression for the S-matrix element, $S_{\mathbf{pr}}(E)$:

$$S_{\mathbf{pr}}(E) = -\frac{\langle\phi_{\mathbf{p}}|\psi^+_{E\mathbf{r}}\rangle}{\langle\phi_{\mathbf{p}}|\phi^+_{E\mathbf{p}}\rangle}. \tag{2.22}$$

Therefore, in order to obtain a useful expression for $S_{\mathbf{pr}}(E)$, it is simply necessary to substitute an appropriate expression for the scattering eigenstate $|\psi^+_{E\mathbf{r}}\rangle$ into equation (2.22). This can be achieved by using equations (2.17), (2.20) and (2.21) to apply the microcanonical density operator to a *purely incoming* wavepacket $|\phi_{\mathbf{r}}\rangle$ (*i.e.*, a wavepacket that satisfies the condition $\langle\phi_{\mathbf{r}}|\phi^+_{E\mathbf{r}}\rangle = 0$). Hence,

$$\begin{aligned} 2\pi\hbar\delta(E-H)|\phi_{\mathbf{r}}\rangle &= \sum_{\mathbf{c}} |\psi^+_{E\mathbf{c}}\rangle\langle\psi^+_{E\mathbf{c}}|\phi_{\mathbf{r}}\rangle, \\ &= |\psi^+_{E\mathbf{r}}\rangle\langle\phi^-_{E\mathbf{r}}|\phi_{\mathbf{r}}\rangle, \end{aligned} \tag{2.23}$$

which implies that

$$|\psi^{+}_{E\mathbf{r}}\rangle = \frac{2\pi\hbar\delta(E-H)|\phi_{\mathbf{r}}\rangle}{\langle\phi^{-}_{E\mathbf{r}}|\phi_{\mathbf{r}}\rangle}, \tag{2.24}$$

and thus, from equation (2.22),

$$S_{\mathbf{pr}}(E) = -2\pi\hbar\frac{\langle\phi_{\mathbf{p}}|\delta(E-H)|\phi_{\mathbf{r}}\rangle}{\langle\phi_{\mathbf{p}}|\phi^{+}_{E\mathbf{p}}\rangle\langle\phi^{-}_{E\mathbf{r}}|\phi_{\mathbf{r}}\rangle}. \tag{2.25}$$

Equation (2.25) is a general expression for the S-matrix element for a transition from the initial channel $\mathbf{r}$ to the final channel $\mathbf{p}$ at energy E. In the next section we shall go on to develop a time-dependent formulation for this quantity.

2.2.3 A time-dependent wavepacket formulation for the S-matrix

Since the work in the subsequent chapters of this thesis uses the time-dependent wavepacket method, we choose here to use the Fourier representation of the delta function (given in equation (2.11)) to obtain the following time-dependent expression for the S-matrix element, $S_{\mathbf{pr}}(E)$:

$$S_{\mathbf{pr}}(E) = \frac{-1}{\langle\phi_{\mathbf{p}}|\phi^{+}_{E\mathbf{p}}\rangle\langle\phi^{-}_{E\mathbf{r}}|\phi_{\mathbf{r}}\rangle}\int_{-\infty}^{+\infty} e^{+iEt/\hbar}\langle\phi_{\mathbf{p}}|e^{-iHt/\hbar}|\phi_{\mathbf{r}}\rangle\, dt. \tag{2.26}$$

Notice in particular that $|\phi_{\mathbf{p}}\rangle$ must be purely outgoing for equation (2.22) to be true, and that $|\phi_{\mathbf{r}}\rangle$ must be purely incoming for equation (2.23) to be true. These two conditions are therefore necessary in order for equation (2.26) to give the correct result for a general (elastic, inelastic or reactive) transition. It is possible to relax the requirement that $|\phi_{\mathbf{p}}\rangle$ be purely outgoing by replacing equation (2.22) with

$$S_{\mathbf{pr}}(E) = \frac{\langle\phi_{\mathbf{p}}|\phi^{-}_{E\mathbf{p}}\rangle\delta_{\mathbf{pr}} - \langle\phi_{\mathbf{p}}|\psi^{+}_{E\mathbf{r}}\rangle}{\langle\phi_{\mathbf{p}}|\phi^{+}_{E\mathbf{p}}\rangle}, \tag{2.27}$$

and by making appropriate modifications to equations (2.25) and (2.26). However, the requirement that $|\phi_{\mathbf{r}}\rangle$ be purely incoming is *essential* in order for equation (2.24)

to give the correct result for $|\psi^+_{E\mathbf{r}}\rangle$. This condition places inconvenient restrictions on the form of the initial wavepacket and it is thus desirable to remove it. To do this it is convenient to restrict the type of transitions under study to inelastic and reactive transitions (for which $\mathbf{p} \neq \mathbf{r}$) and to consider the causality argument set out in the following.

2.2.4 Causality argument applied to the S-matrix

In the above discussion, $|\phi_\mathbf{r}\rangle$ is assumed to be purely incoming and localised in the asymptotic region of channel $\mathbf{r}$. It is therefore clear that its entire history $|\phi_\mathbf{r}(t)\rangle = e^{-iHt/\hbar}|\phi_\mathbf{r}\rangle$ with $t \leq 0$ will also be confined to the asymptotic region of this same channel and thus will have zero overlap with $|\phi_\mathbf{p}\rangle$ (assuming that $\mathbf{p} \neq \mathbf{r}$). Negative times do not therefore contribute to the integral in equation (2.26), and so the lower limit of the integral can be replaced with zero:

$$S_{\mathbf{pr}}(E) = \frac{-1}{\langle\phi_\mathbf{p}|\phi^+_{E\mathbf{p}}\rangle\langle\phi^-_{E\mathbf{r}}|\phi_\mathbf{r}\rangle} \int_0^{+\infty} e^{+iEt/\hbar}\langle\phi_\mathbf{p}|e^{-iHt/\hbar}|\phi_\mathbf{r}\rangle\, dt \quad (\mathbf{p} \neq \mathbf{r}). \quad (2.28)$$

The remaining task is to demonstrate that equation (2.28) is true for *general* initial and final wavepackets, *i.e.*, those which are not purely incoming and outgoing respectively.

In order to do this, consider first a general initial wavepacket, $|\phi'_\mathbf{r}\rangle$,

$$|\phi'_\mathbf{r}\rangle = |\phi_\mathbf{r}\rangle + |\delta\phi^+_\mathbf{r}\rangle, \quad (2.29)$$

where $|\phi_\mathbf{r}\rangle$ is the usual purely incoming wavepacket and $|\delta\phi^+_\mathbf{r}\rangle$ is an arbitrary outgoing component. Since $|\delta\phi^+_\mathbf{r}\rangle$ is purely outgoing we have $\langle\phi^-_{E\mathbf{r}}|\delta\phi^+_\mathbf{r}\rangle = 0$, and therefore we see that adding an arbitrary outgoing component to $|\phi_\mathbf{r}\rangle$ will not affect the denominator of equation (2.28). Furthermore, propagating $|\delta\phi^+_\mathbf{r}\rangle$ forwards in

time (*i.e.*, $t \geq 0$) will simply send it further into the asymptotic region of channel $\mathbf{r}$. Clearly then, the outgoing component of $|\phi'_{\mathbf{r}}\rangle$ will never overlap with $|\phi_{\mathbf{p}}\rangle$ (providing $\mathbf{p} \neq \mathbf{r}$), and this component therefore makes no contribution to the integral in equation (2.28). With this argument we have shown that it is not necessary for the reactant wavepacket to be purely incoming; the correct result for $S_{\mathbf{pr}}(E)$ will be obtained from equation (2.28) if the purely incoming $|\phi_{\mathbf{r}}\rangle$ is replaced by $|\phi'_{\mathbf{r}}\rangle$ which contains an arbitrary outgoing component.

Now, consider the effect on equation (2.28) of replacing the final-state wavepacket $|\phi_{\mathbf{p}}\rangle$ by a wavepacket containing an arbitrary incoming component, $|\delta\phi^-_{\mathbf{p}}\rangle$, localised in the asymptotic region of channel $\mathbf{p}$:

$$|\phi'_{\mathbf{p}}\rangle = |\phi_{\mathbf{p}}\rangle + |\delta\phi^-_{\mathbf{p}}\rangle. \tag{2.30}$$

It is clear that $\langle\delta\phi^-_{\mathbf{p}}|\phi^+_{E\mathbf{p}}\rangle = 0$ from a similar argument to that used above for $\langle\phi^-_{E\mathbf{r}}|\delta\phi^+_{\mathbf{r}}\rangle$. Also, since $|\delta\phi^-_{\mathbf{p}}\rangle$ is purely incoming and is localised in the asymptotic region of channel $\mathbf{p}$, we see that the quantity $\langle\delta\phi^-_{\mathbf{p}}|e^{-iHt/\hbar} \equiv \langle e^{+iHt/\hbar}\delta\phi^-_{\mathbf{p}}| \equiv \langle\delta\phi^-_{\mathbf{p}}(-t)|$ with $t \geq 0$ will also be confined to the asymptotic region of the product channel and will therefore have zero overlap with $|\phi_{\mathbf{r}}\rangle$. Hence, using $|\phi'_{\mathbf{p}}\rangle$ instead of $|\phi_{\mathbf{p}}\rangle$ in equation (2.28) makes no difference to the result for $S_{\mathbf{pr}}(E)$. We have thus shown that equation (2.28) is true for *general* initial and final wavepackets which do not have to be purely incoming and outgoing respectively.

There have been a number of derivations of the time-dependent expression for the S-matrix in the literature in recent years, ranging from the straightforward derivation of Dai and Zhang [43] to the more formal derivation of Tannor and Weeks [78]. However, nearly all of these derivations obtain equation (2.26) rather than equation (2.28) as their final result. In other words, most of these derivations do not

exploit the causality argument described above. As has been shown, this places inconvenient restrictions on the form of the initial wavepacket since in this case it is essential that the initial wavepacket be purely incoming. Derivations in the literature which *do* obtain equation (2.28) (or its time-independent analogue) are given in references [45, 79, 80, 81].

Equation (2.28) is the central result of this section. The next task is to define the initial state-selected reaction probability (ISSRP) in terms of the S-matrix, and then finally to present the "flux operator" formalism for the ISSRP which will be shown to be equivalent to the S-matrix definition.

2.2.5 The initial state-selected reaction probability (ISSRP)

It was noted in section 2.2.1 that the elements $S_{\mathbf{pr}}(E)$ of the scattering matrix are probability amplitudes. The probability of a transition occurring at energy E from initial channel $\mathbf{r}$ to final channel $\mathbf{p}$, $P_{\mathbf{pr}}(E)$, is therefore given by

$$P_{\mathbf{pr}}(E) = |S_{\mathbf{pr}}(E)|^2. \tag{2.31}$$

In order to discuss the initial state-selected reaction probability (ISSRP) it is necessary to be more specific about the nature of the subscripts $\mathbf{r}$ and $\mathbf{p}$. We need to substitute *two* new subscripts for each of these single subscripts, the first denoting the arrangement channel involved, and the second indicating the asymptotic quantum numbers of the state in that channel. So, for example, in this more detailed notation, a particular element of the scattering matrix might be given as $S_{\beta\mathbf{j},\alpha\mathbf{i}}(E)$, where $\alpha\mathbf{i}$ indicates that the initial state is located in arrangement channel α and is described by the asymptotic quantum numbers $\mathbf{i}$, and $\beta\mathbf{j}$ indicates that the product state is located in arrangement channel β and is described by the asymptotic

quantum numbers **j**.

Using this new notation in conjunction with equation (2.31), the ISSRP for forming products in arrangement channel β, starting from a particular initial state of a reactive system, $\alpha\mathbf{i}$, can be obtained by summing over all relevant scattering matrix elements in the following way:

$$P^{\beta}_{\alpha\mathbf{i}}(E) = \sum_{\mathbf{j}} |S_{\beta\mathbf{j},\alpha\mathbf{i}}(E)|^2, \qquad \alpha \neq \beta. \tag{2.32}$$

Equation (2.32) is the most straightforward definition of the ISSRP. However, it turns out that it is more efficient from a computational point of view to implement an alternative, equivalent expression for the ISSRP, and it is this expression which is introduced and discussed in the next section.

2.2.6 The flux formulation for the ISSRP

It is clear that we could use equations (2.28) and (2.32) to obtain the ISSRP simply by summing over the relevant state-to-state information. However, calculating the ISSRP in this way is a waste of computational effort: in evaluating the sum in equation (2.32) one is wastefully discarding a level of detail which is not needed for the ISSRP because it is a more averaged quantity than a state-to-state scattering matrix element. Therefore, the purpose of this section is to prove the validity of a more efficient way of calculating the ISSRP known as the "flux formulation". This formulation allows one to calculate the ISSRP simply by evaluating the total wavepacket flux which passes through a surface chosen to divide the product part of coordinate space from the reactant part.

Our aim is to prove that the following expression [42] for the ISSRP is equivalent

to equation (2.32):

$$P^{\beta}_{\alpha \mathbf{i}}(E) = \langle \psi^{+}_{E,\alpha \mathbf{i}} | \hat{F}^{\beta} | \psi^{+}_{E,\alpha \mathbf{i}} \rangle, \tag{2.33}$$

where $\hat{F}^{\beta}$ is the flux operator [82, 83, 84] which calculates the flux into arrangement channel β and is defined as

$$\hat{F}^{\beta} = \frac{i}{\hbar}[H, h(f_{\beta})]. \tag{2.34}$$

In this expression, $h(f_{\beta})$ is a Heaviside function such that

$$\begin{aligned} h(f_{\beta}) &= 1 \quad f_{\beta} \geq 0, \\ h(f_{\beta}) &= 0 \quad f_{\beta} < 0, \end{aligned} \tag{2.35}$$

where

$$f_{\beta} = R_{\beta} - \overline{R}_{\beta}. \tag{2.36}$$

Here, R_{β} is the translational mass-scaled Jacobi coordinate of the β arrangement channel (see appendix B for a description of Jacobi coordinates), *i.e.*, $\overline{R}_{\beta}$ defines a dividing surface between the reactants and the products in arrangement channel β, with $f_{\beta} > 0$ on the product side.

It is straightforward to show that equation (2.34) gives the following expression for the flux operator,

$$\hat{F}^{\beta} = -\frac{i\hbar}{2\mu}\left[\frac{\partial}{\partial R_{\beta}}\delta(R_{\beta} - \overline{R}_{\beta}) + \delta(R_{\beta} - \overline{R}_{\beta})\frac{\partial}{\partial R_{\beta}}\right], \tag{2.37}$$

since the only part of the Hamiltonian H that the Heaviside function does not commute with is the radial kinetic energy operator for motion in the R_{β} direction. We now substitute equation (2.37) into equation (2.33), and consider the situation in which $\overline{R}_{\beta}$ is large enough such that we can justifiably use the asymptotic expression for $|\psi^{+}_{E,\alpha \mathbf{i}}\rangle$ implied by equation (2.17):

$$|\psi^{+}_{E,\alpha \mathbf{i}}\rangle \overset{R_{\beta} \to \infty}{\longrightarrow} -\sum_{\mathbf{j}} h^{+}_{E\mathbf{j}}(R_{\beta}) \Phi_{\beta \mathbf{j}}(\mathbf{x}_{\beta}) S_{\beta \mathbf{j}, \alpha \mathbf{i}}(E), \tag{2.38}$$

where the sum over j denotes a sum over all the open channels in arrangement channel β at energy E. Evaluating equation (2.33) in this way, and in particular exploiting the orthonormality of the internal channel eigenstates in arrangement β, $\Phi_{\beta \mathbf{j}}(\mathbf{x}_\beta)$, yields the expression for $P^{\beta}_{\alpha \mathbf{i}}(E)$ given previously in equation (2.32) as the definition of the ISSRP,

$$P^{\beta}_{\alpha \mathbf{i}}(E) = \sum_{\mathbf{j}} |S_{\beta \mathbf{j},\alpha \mathbf{i}}(E)|^2, \qquad \alpha \neq \beta,$$

and thus we have shown that the flux formulation of equation (2.33) is a valid method for calculating quantum mechanical initial state-selected reaction probabilities.

The implementation of equation (2.33) requires the calculation of $|\psi^{+}_{E,\alpha \mathbf{i}}\rangle$. As implied by equations (2.11) and (2.24), this can be accomplished by Fourier transforming a time-dependent wavepacket $|\psi_{\alpha \mathbf{i}}(t)\rangle$. Thus,

$$|\psi^{+}_{E,\alpha \mathbf{i}}\rangle = \frac{1}{\langle \phi^{-}_{E,\alpha \mathbf{i}} | \phi_{\alpha \mathbf{i}} \rangle} \int_{-\infty}^{+\infty} e^{+iEt/\hbar} |\psi_{\alpha \mathbf{i}}(t)\rangle dt, \tag{2.39}$$

where

$$|\psi_{\alpha \mathbf{i}}(t)\rangle = e^{-i(H - i\epsilon)t/\hbar} |\phi_{\alpha \mathbf{i}}\rangle, \tag{2.40}$$

and $|\phi_{\alpha \mathbf{i}}\rangle$ is an initial state-selected (purely incoming) wavepacket in channel $\alpha \mathbf{i}$.

2.2.7 Causality argument applied to the ISSRP

Applying the same causality argument to equation (2.39) (in the context of its use in equation (2.33)) as that which was used to obtain equation (2.28) from equation (2.26), shows that for a purely incoming initial wavepacket the lower limit of the time integral in equation (2.39) can be changed to zero:

$$|\psi^{+}_{E,\alpha \mathbf{i}}\rangle = \frac{1}{\langle \phi^{-}_{E,\alpha \mathbf{i}} | \phi_{\alpha \mathbf{i}} \rangle} \int_{0}^{+\infty} e^{+iEt/\hbar} |\psi_{\alpha \mathbf{i}}(t)\rangle dt. \tag{2.41}$$

Once this has been done, adding an arbitrary outgoing component to $|\phi_{\alpha \mathbf{i}}\rangle$ will make no difference to either the numerator or the denominator of equation (2.33), and therefore we can use a *general* initial wavepacket $|\phi_{\alpha \mathbf{i}}\rangle$ in equation (2.41) which does not have to be purely incoming.

In conclusion, therefore, the ISSRP for a reaction can be calculated from equation (2.33) in conjunction with equation (2.41).

2.2.8 Summary

In summary, in this section we have derived a time-dependent expression for the scattering matrix element, $S_{\mathbf{pr}}(E)$, starting from some basic premises of quantum mechanical scattering theory. Also, we have introduced the initial state-selected reaction probability (ISSRP), and given the flux formulation for the calculation of this quantity. We have shown this formulation to be equivalent to summing over the square moduli of appropriate S-matrix elements.

2.3 Approximate methods for higher total angular momenta

2.3.1 The initial state-selected reaction cross section

The reaction cross section, $\sigma(E)$, for a particular pair of atoms or molecules is an effective area which describes their propensity to react at a given energy [1], such that the larger the cross section, the more likely it is that reaction will take place between the two species. The initial state-selected reaction cross section, $\sigma_{\alpha \mathbf{i}}(E)$, therefore describes the likelihood for reaction to take place given that the reactants are in a particular initial state $\mathbf{i}$ of arrangement channel α. For the atom plus diatom

reaction

$$\mathrm{A} + \mathrm{BC} \longrightarrow \mathrm{AB} + \mathrm{C}, \tag{2.42}$$

the initial state-selected cross section (degeneracy-averaged over the K quantum number) is given by [53]

$$\sigma_{\alpha \mathbf{i}}(E_T) = \frac{1}{2j+1} \times \frac{\pi\hbar^2}{2\mu E_T} \times \sum_J \sum_K (2J+1) P_{\alpha \mathbf{i}}^{JK}(E_T). \tag{2.43}$$

In this expression, j is the rotational quantum number of the reactant diatomic, $\mathbf{i}$ specifies the ro-vibrational quantum numbers (v, j) of the reactants, J is the total angular momentum quantum number, K is the quantum number for the projection of the total angular momentum onto a body-fixed axis, E_T is the initial relative translational energy of the reactants, and the reduced mass μ is given by

$$\mu = \frac{m_A m_{BC}}{m_A + m_{BC}}. \tag{2.44}$$

The ISSRP in equation (2.43) is the same as that given in equation (2.33), but from this point on we shall no longer explicitly label the ISSRP by the product arrangement channel β. However, we do now need to have explicit labels to show the dependence of the ISSRP on the total angular momentum, J, and its projection onto a body-fixed axis, K.

2.3.2 Translational energy dependence of the cross section

The dependence of the (initial state-selected) cross section on translational energy in the low-energy region is very strongly influenced by the thermochemistry of the reaction [1]. For a reaction which is exothermic and for which there is no barrier along the reaction coordinate there is no "threshold energy", *i.e.*, the cross section can be non-zero for any translational energy $E_T > 0$. At low energies the cross section is

extremely large, and it decreases as the energy increases as shown in figure 2.5(a). This energy-dependence can be understood in terms of equation (2.43) by realising that a reaction which is exothermic and has no barrier has a finite (*i.e.*, non-zero) reaction probability $P_{\alpha i}^{JK}(E_T)$ for a sufficiently low J at any translational energy $E_T > 0$. Given, therefore, that at low energies the $1/E_T$ factor in equation (2.43) is extremely large, the cross section is correspondingly very large in the low-energy region.

As an example of this behaviour, consider an exothermic reaction between an ion and a non-polar molecule which proceeds without a barrier [85]. In the simple classical treatment known as Langevin theory [86], the rate of the reaction is considered to be entirely determined by the long-range forces between the reactants. (In other words, the cross section for reaction is equated to a simple capture cross section for complex formation.) To obtain an analytical expression for the cross section, we assume that reaction will take place provided the reactants have sufficient energy to surmount the barrier in the reactant valley which is calculated by adding a spherically-averaged ion-induced-dipole interaction to the repulsive centrifugal term. The resulting expression for the cross section is [85]

$$\sigma(E_T) = \pi \left[\frac{q^2 \alpha}{(4\pi\epsilon_0)^2 E_T} \right]^{\frac{1}{2}}, \tag{2.45}$$

where q is the charge on an electron, and α is the spherically-averaged polarisability of the neutral molecule. We shall return to this expression later in the thesis.

In contrast with the behaviour of an exothermic reaction which proceeds without a barrier, a reaction which is endothermic and/or proceeds *via* a barrier shows very different behaviour in the low-energy region (see figure 2.5(b)). The cross section is zero for all energies less than a threshold energy (where the threshold energy

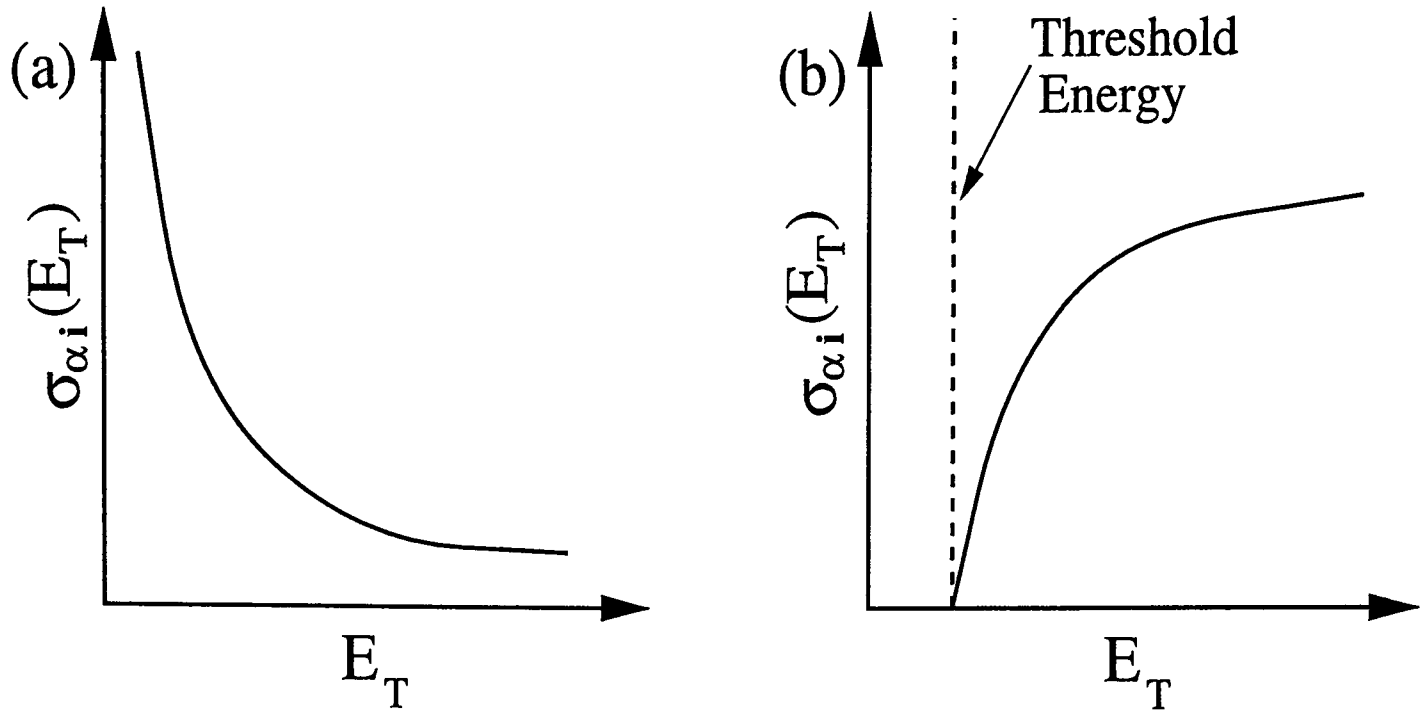


Figure 2.5 The low-energy behaviour of the initial state-selected reaction cross section as a function of translational energy (a) for a reaction which is exothermic and for which there is no barrier along the reaction coordinate, and (b) for a reaction which is endothermic and/or proceeds *via* a barrier.

corresponds either to the endothermicity of the reaction, or to the effective barrier height), and thereafter increases as a function of energy, usually levelling off to an asymptotic value. This can be understood from equation (2.43) by noting that for such a reaction, the reaction probability $P_{\alpha i}^{JK}(E_T)$ is zero until there is sufficient energy to overcome the endothermicity and/or the reaction barrier. As a result of this, there is no contribution to the cross section at energies corresponding to very large values of the $1/E_T$ factor. The cross section thus increases as a function of translational energy (in the threshold region) since at higher translational energies, more total angular momenta can contribute to the reaction (there is more energy available to overcome the centrifugal barrier).

Up to this point we have introduced the initial state-selected reaction cross section $\sigma_{\alpha i}(E_T)$ and described its behaviour as a function of translational energy in the threshold region for two contrasting classes of reaction. Once the initial state-selected reaction cross section is known for a range of energies it can be used to

calculated the initial state-selected reaction rate constant as discussed in the following section.

2.3.3 The initial state-selected rate constant

The initial state-selected rate constant, $k_{\alpha \mathbf{i}}(T)$, is obtained by thermally averaging the initial state-selected cross section with a Maxwell-Boltzmann distribution [1, 53]:

$$k_{\alpha \mathbf{i}}(T) = \left(\frac{8k_BT}{\pi\mu}\right)^{\frac{1}{2}} \times \left(\frac{1}{k_BT}\right)^2 \times \int_0^\infty E_T \exp\left(\frac{-E_T}{k_BT}\right) \sigma_{\alpha \mathbf{i}}(E_T)\, dE_T. \qquad (2.46)$$

Note that this is not the same as the usual thermal rate constant, $k(T)$, since $k_{\alpha \mathbf{i}}(T)$ corresponds to reaction from a single initial state. To obtain the full thermal rate constant we need to average over all possible initial states, assuming that the reactants are in a state of thermal equilibrium [1]. For example, for the atom plus diatom reaction in equation (2.42), where the diatomic is in the initial state (v, j), the full thermal rate constant is given by

$$k(T) = \frac{1}{q_{BC}} \sum_v \sum_j g_j \exp\left(\frac{-E_{vj}}{k_BT}\right) k_{vj}(T), \qquad (2.47)$$

where $g_j \equiv (2j+1)$ is the degeneracy of the rotational state j of the diatomic, E_{vj} is the internal energy of the BC molecule in the ro-vibrational state described by the quantum numbers (v, j), and q_{BC} is the partition function for the internal (ro-vibrational) motion of BC:

$$q_{BC} = \sum_v \sum_j g_j \exp\left(\frac{-E_{vj}}{k_BT}\right). \qquad (2.48)$$

Having introduced the initial state-selected reaction cross section and rate constant we go on in the next section to describe some approximations which are required in order to compute these quantities for systems of interest.

2.3.4 Introduction to higher total angular momenta

It is clear from equation (2.43) that in order to calculate the initial state-selected cross section (and thus the initial state-selected rate constant) it is necessary to know the ISSRP for all contributing values of J. To calculate exact quantum mechanical results for $J > 0$ becomes increasingly computationally intensive as J increases because the number of angular basis functions in a wavepacket calculation scales as $(2J+1)$, reflecting the number of possible projections of the total angular momentum onto a body-fixed axis. As a result of this, most calculations on chemical systems use approximate methods for $J > 0$. There are many such methods [87, 88, 89, 90, 91], and in the following sections we first briefly describe some of the more important ones, and then go on to discuss in more detail the method used in the calculations in chapter 4: the rotationally adiabatic approximation [92, 93, 94, 95, 96].

2.3.5 The centrifugal sudden (CS) approximation

To discuss the centrifugal sudden approximation it is necessary to refer to a particular coordinate system: the Jacobi coordinates. We use the mass-scaled Jacobi coordinates, (R, r, γ), of the A + BC arrangement [97] (see appendix B for a description of these coordinates); the unscaled Jacobi coordinates corresponding to these, $(\tilde{R}, \tilde{r}, \gamma)$, are illustrated in figure 2.6.

The centrifugal sudden (CS) approximation is the standard decoupling approximation for treating higher angular momenta. It assumes that Coriolis coupling between projections of the total angular momentum $\boldsymbol{J}$ along the $\boldsymbol{R}$ vector can be ignored, and the result of this is that K becomes a good quantum number, where K is the projection of $\boldsymbol{J}$ onto the $\boldsymbol{R}$ vector.

To derive the CS approximation for an atom plus diatom system we begin with the exact Hamiltonian for a three-atom system. Within the Born-Oppenheimer approximation this is

$$H = T + U + V, \tag{2.49}$$

where T is the radial kinetic operator given by

$$T = -\frac{\hbar^2}{2\mu}\left(\frac{\partial^2}{\partial R^2} + \frac{\partial^2}{\partial r^2}\right), \tag{2.50}$$

U is the rotation part of the Hamiltonian given by

$$U = \frac{\hat{j}^2}{2\mu r^2} + \frac{\hat{\ell}^2}{2\mu R^2}, \tag{2.51}$$

and V is the potential energy surface for the system[†].

[†]Note that the expression in equation (2.49) is a reduced Hamiltonian. The full Hamiltonian $\mathcal{H}$ is given by [89],

$$\mathcal{H} = -\frac{\hbar^2}{2\mu}\left(\frac{1}{R}\frac{\partial^2}{\partial R^2}R + \frac{1}{r}\frac{\partial^2}{\partial r^2}r\right) + \frac{\hat{j}^2}{2\mu r^2} + \frac{\hat{\ell}^2}{2\mu R^2} + V(R, r, \gamma), \tag{2.52}$$

and the corresponding Schrödinger equation is

$$\mathcal{H}\Psi(R, r, \gamma) = E\Psi(R, r, \gamma), \tag{2.53}$$

where E is the total energy excluding that associated with the motion of the centre-of-mass, and $\Psi(R, r, \gamma)$ is the full wavefunction. However, in order to simplify the form of the kinetic energy part of the operator, it is better to use a *reduced* Hamiltonian, H, together with a reduced wavefunction $\psi(R, r, \gamma)$ given by,

$$\psi(R, r, \gamma) = Rr\Psi(R, r, \gamma). \tag{2.54}$$

Thus

$$\mathcal{H}\Psi(R, r, \gamma) = \frac{1}{Rr}H\psi(R, r, \gamma), \tag{2.55}$$

where

$$H = Rr\mathcal{H}\frac{1}{Rr}, \tag{2.56}$$

which gives the expression for the reduced Hamiltonian presented in equation (2.49).

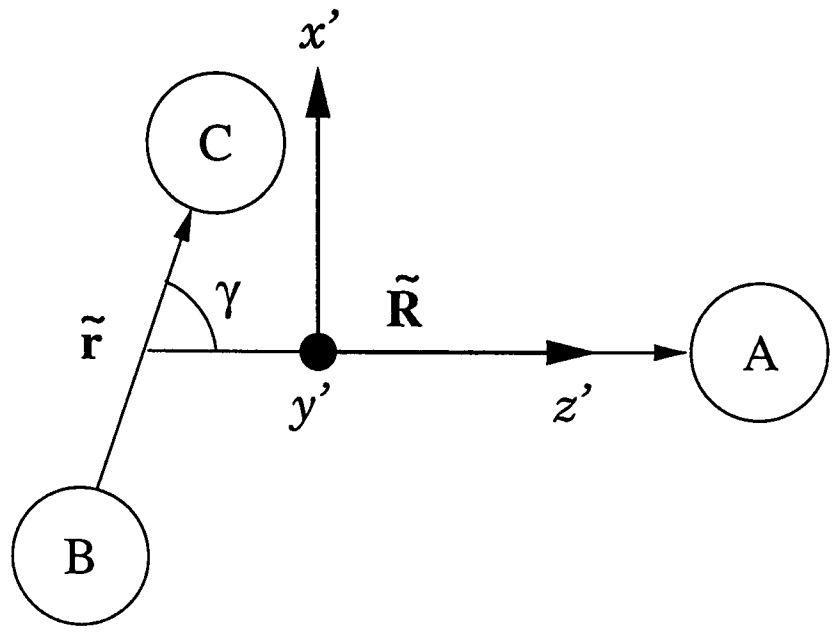


Figure 2.6 The Jacobi coordinates $(\tilde{R}, \tilde{r}, \gamma)$ for the A + BC arrangement, shown with the body-fixed axes (x', y', z').

We proceed by considering the matrix elements of U. To do this it is necessary to introduce a convenient set of basis functions with which to represent the angular coordinates $\hat{\boldsymbol{R}}$ and $\hat{r}$. The functions we use are the body-fixed axes (BF) functions [3, 88, 97]

$$\mathcal{Y}_{jK}^{JM}(\hat{\boldsymbol{R}}, \hat{r}) = \mathcal{Y}_{jK}^{JM}(\gamma, \Omega) = \left(\frac{2J+1}{4\pi}\right)^{\frac{1}{2}} Y_{jK}(\gamma, 0)\, D_{KM}^{J}(\Omega), \qquad (2.57)$$

where $\Omega = (\Psi, \Theta, \Phi)$ are the Euler angles [11, 98] which take the space-fixed axes (x, y, z) onto the body-fixed axes (x', y', z') shown in figure 2.6 (Θ and Φ are the spherical polar angles of $\boldsymbol{R}$ in the original space-fixed axis system and Ψ is a right-hand axis twist about $\boldsymbol{R}$ which brings r into the $x'z'$ plane), and D_{KM}^{J} is a Wigner D function in the passive convention used by Pack [88, 97].

These functions are simultaneous orthonormal eigenfunctions of the angular momentum operators $\hat{J}^2 = (\hat{j} + \hat{\ell})^2$, $\hat{j}^2$, $\hat{J}_z$, $\hat{J}_{z'}$ and $\hat{j}_{z'}$, where $\hat{J}_{z'}$ and $\hat{j}_{z'}$ are the operators for the projection of $\boldsymbol{J}$ and $\boldsymbol{j}$ on the body-fixed z' axis along $\boldsymbol{R}$. The properties of the functions can be summarised as follows:

$$\hat{J}^2\, \mathcal{Y}_{jK}^{JM} \;=\; \hbar^2\, J(J+1)\, \mathcal{Y}_{jK}^{JM}, \qquad (2.58)$$

$$\hat{j}^2\,\mathcal{Y}^{JM}_{jK} = \hbar^2\, j\,(j+1)\,\mathcal{Y}^{JM}_{jK}, \tag{2.59}$$

$$\hat{J}_z\,\mathcal{Y}^{JM}_{jK} = \hbar\, M\,\mathcal{Y}^{JM}_{jK}, \tag{2.60}$$

$$\hat{J}_{z'}\,\mathcal{Y}^{JM}_{jK} = \hbar\, K\,\mathcal{Y}^{JM}_{jK}, \tag{2.61}$$

$$\hat{j}_{z'}\,\mathcal{Y}^{JM}_{jK} = \hbar\, K\,\mathcal{Y}^{JM}_{jK}, \tag{2.62}$$

$$\int\int \mathcal{Y}^{J'M'}_{j'K'}(\gamma,\Omega)^{*}\mathcal{Y}^{JM}_{jK}(\gamma,\Omega)\,\sin\gamma\,d\gamma\,d\Omega = \delta_{J'J}\delta_{M'M}\delta_{j'j}\delta_{K'K}. \tag{2.63}$$

We begin by considering the case where $J = 0$. In this case, the form of U is simply

$$U^{J=0} = \frac{1}{2\mu}\left(\frac{1}{R^2}+\frac{1}{r^2}\right)\hat{j}^2, \tag{2.64}$$

and equation (2.59) shows that the matrix elements of U are trivial to evaluate:

$$\langle JMj'K'|U^{J=0}|JMjK\rangle = \frac{1}{2\mu}\left(\frac{1}{R^2}+\frac{1}{r^2}\right)\langle 0\;0\;j'K'|\hat{j}^2|0\;0\;jK\rangle \tag{2.65}$$

$$= \frac{\hbar^2}{2\mu}\left(\frac{1}{R^2}+\frac{1}{r^2}\right)j(j+1)\delta_{j'j}\delta_{K'K}. \tag{2.66}$$

For the case where $J \neq 0$ we use equation (2.51) for the rotational part U of the Hamiltonian, and again consider the matrix elements of the operator in the basis given in equation (2.57):

$$\langle JMj'K'|U|JMjK\rangle = \frac{1}{2\mu r^2}\langle JMj'K'|\hat{j}^2|JMjK\rangle + \frac{1}{2\mu R^2}\langle JMj'K'|\hat{\ell}^2|JMjK\rangle. \tag{2.67}$$

Clearly, the first term is evaluated using equation (2.59) in the same way as in the $J = 0$ case. However, we now also have to consider the representation of $\hat{\ell}^2$. It is a standard result [3] to show that by using the ladder operators,

$$\hat{J}_{\pm} = \hat{J}_{x'} \mp i\hat{J}_{y'}, \tag{2.68}$$

and

$$\hat{j}_{\pm} = \hat{j}_{x'} \pm i\hat{j}_{y'}, \tag{2.69}$$

we obtain

$$\left(\hat{\ell}^2\right)^J_{j'K',jK} = \langle JMj'K' \,|\, (\hat{J}-\hat{j})^2 \,|\, JMjK\rangle \tag{2.70}$$

$$= \langle JMj'K' \,|\, \hat{J}^2+\hat{j}^2-2\hat{J}\cdot\hat{j} \,|\, JMjK\rangle \tag{2.71}$$

$$= \langle JMj'K' \,|\, \hat{J}^2+\hat{j}^2-2\hat{J}_{z'}\hat{j}_{z'}-\hat{J}_+\hat{j}_+-\hat{J}_-\hat{j}_- \,|\, JMjK\rangle \tag{2.72}$$

$$= \hbar^2\delta_{j'j}[\, D_{JjK}\delta_{K'K} - C^+_{JK}C^+_{jK}\delta_{K'K+1} - C^-_{JK}C^-_{jK}\delta_{K'K-1}\,] \tag{2.73}$$

where

$$D_{JjK} = J(J+1)+j(j+1)-2K^2, \tag{2.74}$$

and

$$C^{\pm}_{ab} = [a(a+1)-b(b\pm 1)]^{\frac{1}{2}}\,. \tag{2.75}$$

Equations (2.73), (2.74) and (2.75) constitute the final expression necessary to evaluate the exact representation of U in the basis given by the functions $\mathcal{Y}^{JM}_{jK}(\hat{\boldsymbol{R}},\hat{\boldsymbol{r}})$.

It is clear that in the exact representation K is not a good quantum number, since equation (2.73) contains terms which couple different K states together. However, in the CS approximation these Coriolis terms are ignored so that the representation is diagonal in K. This is equivalent to saying that the projection of the total angular momentum onto the $\boldsymbol{R}$ vector is conserved. The CS expression for the matrix elements of U in the case where $J>0$ is therefore

$$\begin{aligned}\langle JMj'K'|U|JMjK\rangle \;\approx\; & \frac{\hbar^2}{2\mu}\left(\frac{1}{R^2}+\frac{1}{r^2}\right) j(j+1)\delta_{j'j}\delta_{K'K} \\ + \; & \frac{\hbar^2}{2\mu}\frac{1}{R^2}\left[J(J+1)-2K^2\right]\delta_{j'j}\delta_{K'K}.\end{aligned} \tag{2.76}$$

Comparing equations (2.65) and (2.76) shows that we can regard the CS approximation for a $J>0$ calculation as the addition of an effective potential, $U^{\mathrm{CS}}_{J|K|}(R)$,

to the Hamiltonian for $J = 0$, where

$$U^{\mathrm{CS}}_{J|K|}(R) = \frac{\hbar^2}{2\mu}\frac{1}{R^2}\left[J(J+1) - 2K^2\right]. \tag{2.77}$$

Inspection of equations (2.67) and (2.73) shows that Coriolis coupling decreases as $1/R^2$, and therefore that in the asymptotic A + BC region (where the geometrical configuration tends towards that of a prolate top), Coriolis coupling can safely be ignored. However, the assumption that the projection of the total angular momentum onto the $\boldsymbol{R}$ vector is conserved more generally is difficult to justify in some cases. An example of a system where the approximation is clearly invalid would be a reaction whose dynamics was dominated by a deep well, the geometry of which was such that the principal axis associated with the smallest moment of inertia was perpendicular to the $\boldsymbol{R}$ vector. (Note that by analogy with the behaviour of rigid asymmetric rotors the projection of $\boldsymbol{J}$ onto the axis of the smallest principal moment of inertia is the body-fixed projection which should be most nearly conserved [90].) A diagram to illustrate a configuration of this sort is given in figure 2.7, and further comments will be made about this later.

Equation (2.76) shows that to carry out a CS calculation for total angular momentum $J \neq 0$ it is necessary to carry out a separate calculation for each contributing value of $|K|$ (since $+K$ and $-K$ are equivalent in this approximation), and that the computational effort for each of these calculations will be the same as for a $J = 0$ calculation. Note that the range of K is as follows:

$$K = -\min(J,j),\ldots,\min(J,j), \tag{2.78}$$

so that in general the computational effort will depend on the choice of the initial state (*i.e.*, it will depend on the choice of the rotational quantum number j for the diatomic).

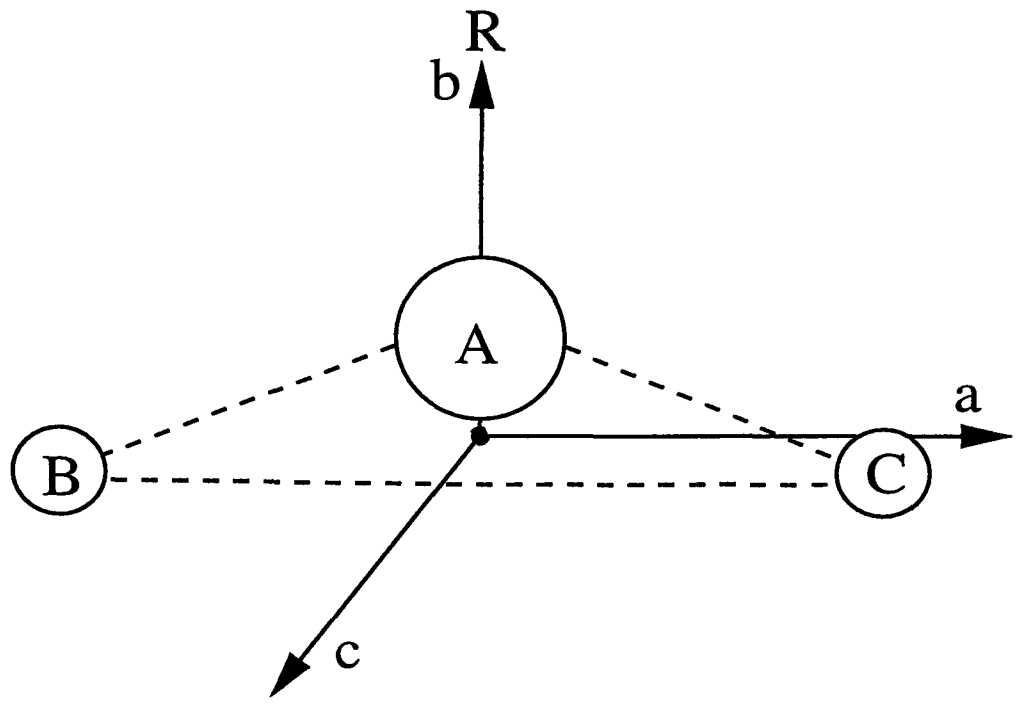


Figure 2.7 Illustration of a geometrical configuration for the reaction A + BC in which the principal axis of least inertia (the $\boldsymbol{a}$ axis) is perpendicular to the $\boldsymbol{R}$ vector thus rendering the CS approximation inappropriate at this geometry.

We have now derived the CS approximation and its main features have been discussed. In the next section we describe McCurdy and Miller's modification to the CS approximation: the optimum centrifugal sudden approximation (OSA).

2.3.6 The optimum centrifugal sudden (OCS) approximation

The CS approximation, in which the projection of $\boldsymbol{J}$ along the A + BC vector $\boldsymbol{R}$ is conserved, is specifically designed for single-arrangement processes such as inelastic scattering. For a two-arrangement process such as reactive scattering, one can imagine that in order to minimise the Coriolis coupling which is to be neglected, it would be preferable to conserve the projection of $\boldsymbol{J}$ along $\boldsymbol{R}$ in the reactant valley, but to conserve the projection of $\boldsymbol{J}$ along $\boldsymbol{R}'$ in the product valley, where $\boldsymbol{R}'$ is the translational mass-scaled Jacobi coordinate appropriate for the product arrangement channel (see appendix B). Clearly, however, the point at which one would switch from the conservation of the reactant helicity, K, to the conservation of the product helicity, K', is somewhat difficult to define.

In order to address this difficulty, McCurdy and Miller designed an optimum CS approximation (OCS) [90] which uses an instantaneous principal axis frame. In this new helicity representation, the body-fixed quantisation axis that is used for a given point on the potential energy surface depends on the geometry of that point. In other words, the quantisation axis is neither $\boldsymbol{R}$ nor $\boldsymbol{R}'$, but is rather the principal axis of the ABC triangle of atoms which corresponds to the smallest principal moment of inertia (the $\boldsymbol{a}$ axis in the standard convention). In the asymptotic region of the reactant valley this axis becomes the reactant translational coordinate $\boldsymbol{R}$, while in the asymptotic region of the product valley it becomes the product translational coordinate $\boldsymbol{R}'$. In the intermediate region it varies smoothly between the two.

It is clear from this description that the OCS approximation is equivalent to the CS approximation in the asymptotic region of the reactant valley. It is also evident that both the CS and the OCS approximations implicitly utilise an adiabatic separation of vibration and rotation since they both neglect Coriolis coupling in some way.

The practical implementation of the OCS approximation is similar to that of the CS approximation in that it requires the addition of an effective rotational surface, $\dot{U}^{\mathrm{OCS}}_{J|K|}$, to the $J = 0$ Hamiltonian. However, in the OCS case, the surface which is added is a function of all three mass-scaled Jacobi coordinates, (R, r, γ), and is the prolate top approximation to the appropriate rigid-rotor energy level of the triangle of atoms ABC:

$$U^{\mathrm{OCS}}_{J|K|}(R, r, \gamma) = E^{J|K_a|}(R, r, \gamma) = \frac{1}{2}(\tilde{B} + \tilde{C})[J(J+1) - K_a^2] + \tilde{A}K_a^2, \qquad (2.79)$$

where $\tilde{A}$, $\tilde{B}$, and $\tilde{C}$ are the rigid-rotor rotational constants for the geometry given by (R, r, γ), and K_a is the quantum number for the projection of $\boldsymbol{J}$ onto the $\boldsymbol{a}$ axis (the principal axis associated with the smallest moment of inertia for a particular

geometry). Note that an adiabatic approximation is implicitly made, in that K_a remains constant while the $\boldsymbol{a}$ axis changes smoothly during the reaction. Clearly, K_a tends to K in the limit of the asymptotic region of the reactant valley, and to K' in the asymptotic region of the product valley.

There are three final points to note concerning the OCS. First, Pack and Parker [97] have pointed out that in addition to neglecting Coriolis coupling as described above, McCurdy and Miller's OCS method makes the additional approximation that the rotational energy surface is given by an instantaneous *rigid-rotor* energy level, whereas in fact for a more rigorous description it would be necessary to describe it by an instantaneous *fluid rotor* energy level (which would only change the $\tilde{B}$ rotational constant). Secondly, the computational effort required for a $J > 0$ calculation within this approximation is the same as that for a CS calculation, except that the set-up of the effective rotational surface may take a little longer in the OCS case. Finally, while this approximation does not work very well for the H + H_2 reaction [90], it has been shown to work satisfactorily (giving cross sections within about 10% of the exact values) in several initial state-selected reactive scattering calculations involving the collision of heavier atoms (such as F and Cl) with H_2 [99].

2.3.7 The rotationally adiabatic approximation (RAA)

The calculations presented in chapter 4 use an approximation which is very slightly different from the OCS approximation described above, and which has been advocated by Bowman and co-workers [92, 93, 94, 95, 96]. The basis of this approximation is that if, as in the OCS approximation, there is an adiabatic separation of rotation and vibration, then it is in fact unnecessary to ignore the off-diagonal terms in

the rigid-rotor Hamiltonian. Instead, for each geometry we can simply diagonalise the full tridiagonal Hamiltonian matrix for each contributing angular momentum quantum number, J, to obtain the appropriate asymmetric top energy levels. This Hamiltonian matrix has elements given by:

$$H_{kk}^{\mathrm{rot}} = \frac{1}{2}(\tilde{B} + \tilde{C})[J(J+1) - k^2] + \tilde{A}k^2, \tag{2.80}$$

and

$$H_{kk\pm 2}^{\mathrm{rot}} = \frac{1}{4}(\tilde{B} - \tilde{C})C_{Jk}^{\pm}C_{Jk\pm 1}^{\pm}, \tag{2.81}$$

and the result of the diagonalisation is simply a different effective rotational energy surface from that used in the OCS, which we shall denote here as $\mathcal{U}_{JK_aK_c}^{\mathrm{RAA}}(R, r, \gamma)$. In this way we include the Coriolis coupling in equation (2.81), albeit in an approximate (adiabatic) way. In other words, instead of using (as in the OCS case) a prolate top approximation to the asymmetric top rigid-rotor energy level as the effective rotational energy surface which is added to the $J = 0$ Hamiltonian, we use the asymmetric top energy level itself. Appendix C discusses the energy levels of a rigid asymmetric rotor in more detail.

As an example of the use of this method, consider a calculation of the ISSRP for the reaction in equation (2.42), where the initial state of the diatomic BC is ($v = 0, j = 1$) and the total angular momentum is $J = 2$. From equation (2.78) we see that the projection of the total angular momentum onto the asymptotic reactant $\boldsymbol{R}$ vector can take the values,

$$K = -\min(J, j), \ldots, \min(J, j) = -1, 0, +1. \tag{2.82}$$

Each of these asymptotic K values correlates adiabatically with a different effective rotational energy surface, and we must therefore carry out separate wavepacket

calculations on each of these surfaces (*i.e.*, the surfaces associated with the 2_{02}, 2_{12} and 2_{11} levels of the ABC asymmetric top). Calculations performed in this way are described in this thesis as using the rotationally adiabatic approximation (RAA). As in the case of the OCS approximation described in the previous section, the RAA has been found to give highly satisfactory results for calculations on reactions involving the collision of heavier atoms (such as F or Cl) with H_2 [99].

2.3.8 Summary

In this section we have introduced the initial state-selected reaction cross section and reaction rate constant and in doing so have shown that we need initial state-selected reaction probabilities for every value of (J, K) contributing to the reaction under study. We have explained the necessity for approximate methods for calculating ISSRPs for total angular momentum quantum numbers $J > 0$, and finally we have described three such approximate methods: the centrifugal sudden approximation, the optimum centrifugal sudden approximation, and the rotationally adiabatic approximation, the latter of which will be used later in this thesis.

2.4 Conclusions

To conclude, in the first part of this chapter we have presented the quantum mechanical theory behind two processes of fundamental chemical importance: molecular photodissociation, and reactive scattering. For molecular photodissociation, we have derived an expression for the absorption spectrum of a dissociative system, which will be used in chapter 3 to model the photodetachment spectrum of FH_2^-. In the area of reactive scattering, we have derived an expression for the initial

state-selected reaction probability (ISSRP) in terms of a matrix element of a flux operator. In the final part of the chapter we have introduced the initial state-selected cross section and rate constant for a reaction, and then described some approximate methods for carrying out calculations for total angular momentum quantum numbers $J > 0$. These reactive scattering expressions will be implemented in chapter 4 which deals with the reaction $N^+ + H_2 \longrightarrow NH^+ + H$.

Chapter 3 Photodetachment Spectroscopy of FH_2^-

In the first part of chapter 2 we derived an expression for the Franck-Condon absorption spectrum of a species in such a way as to be applicable to bound-continuum transitions. In the present chapter we shall describe an application of this theory to the case of the photodetachment spectrum of an anion: FH_2^-. The chapter begins with a brief discussion of the photoelectron spectroscopy of anions in section 3.1, in which we indicate the reasons for carrying out experiments and calculations in this area. Section 3.2 provides an overview of the literature for the F + H_2 reaction and gives the motivation behind the work presented in this chapter. In section 3.3, we describe the assumptions necessary to apply the theory of Franck-Condon absorption spectra to the photodetachment spectra of anions, and then go on to outline the method we used for carrying out the calculations. We present the spectra which we have calculated in section 3.4, and then describe the method used to analyse them in section 3.5, along with the interpretation of the results. In section 3.6, we describe some recent work on the F + H_2 reaction carried out after the publication of the calculations presented in this chapter [100], and finally, in section 3.7, we give a brief summary and offer suggestions for possible future work.

3.1 Anion photoelectron spectroscopy: "transition state spectroscopy"

One of the fundamental goals of chemical physics is to understand the nature of the potential energy surfaces which describe the interactions between atoms, ions and

molecules, and to determine the effect of different features of these surfaces on the chemical reactions they describe. Much of the interest in reaction dynamics focuses on the transition state region, *i.e.*, that region of the surface in which chemical bonds are broken and formed. The forces at work in this region of the potential energy surface will clearly have a very strong influence on the asymptotic properties of the reaction (for example, the product internal state distribution, the product angular distribution, and the reaction cross section). Dynamicists aim to deduce the relationship between the asymptotic properties of a reaction and the features of its transition state region (*e.g.*, the barrier height and width, or the bending potential near the saddle point), and thus a detailed and accurate knowledge of the transition state is required.

State-to-state scattering experiments probe the asymptotic properties of a reaction and from these it is necessary to work backwards to deduce the nature of the transition state. However, recent years have seen the development of a conceptually different type of experiment: "transition state spectroscopy" [101]. These experiments probe the reaction transition state directly using spectroscopic techniques [102], and anion photodetachment spectroscopy, the subject of the work in this chapter, falls into this category.

The anion photodetachment experiment was pioneered by Neumark and co-workers in the early 1990s [103, 104, 105]. The idea of the experiment is to access the transition state region of a neutral reaction *via* the photodetachment of a stable precursor anion. A schematic diagram which illustrates this is given in figure 3.1. The scattering process under study is a "half-collision event", as discussed in chapter 1, and for the system of interest in this chapter it can be written as:

$$FH_2^- \xrightarrow{h\nu} FH_2^{\ddagger} + e^- \begin{cases} \nearrow F + H_2 + e^- \\ \searrow HF + H + e^-. \end{cases}$$

The main advantage in studying half-collision events such as this is that averaging over initial conditions is greatly reduced compared with a full-collision study. A major problem in scattering-based (full-collision) experiments is that the extensive averaging over initial conditions (*i.e.*, averaging over reactant orbital angular momentum and reactant orientation) tends to wash out any sharp structure which might be present in individual partial waves, thus valuable information is lost. In half-collision studies, the angular momentum available to the reactants is extremely restricted because the stable precursor is typically formed in a rotationally cold state. In a photoexcitation process involving simple photon absorption or ejection of a light particle (an electron or H atom) this cold angular momentum distribution is approximately mapped onto the transition region species.

A feature of half-collision studies which must be borne in mind is that in contrast to scattering experiments which are sensitive to all reactant orientations that lead to reaction, half-collision experiments typically provide information on the potential energy surface for only a limited range of geometries – the Franck-Condon region for the electronic transition in question. Although this feature can be advantageous it is clearly essential for the stable precursor to have a good geometric overlap with the transition state region of the upper potential energy surface in order for this region to be probed by the experiment.

In summary, anion photodetachment spectroscopy is one of a range of experiments known as "transition state spectroscopy" experiments. It uses the photodetachment

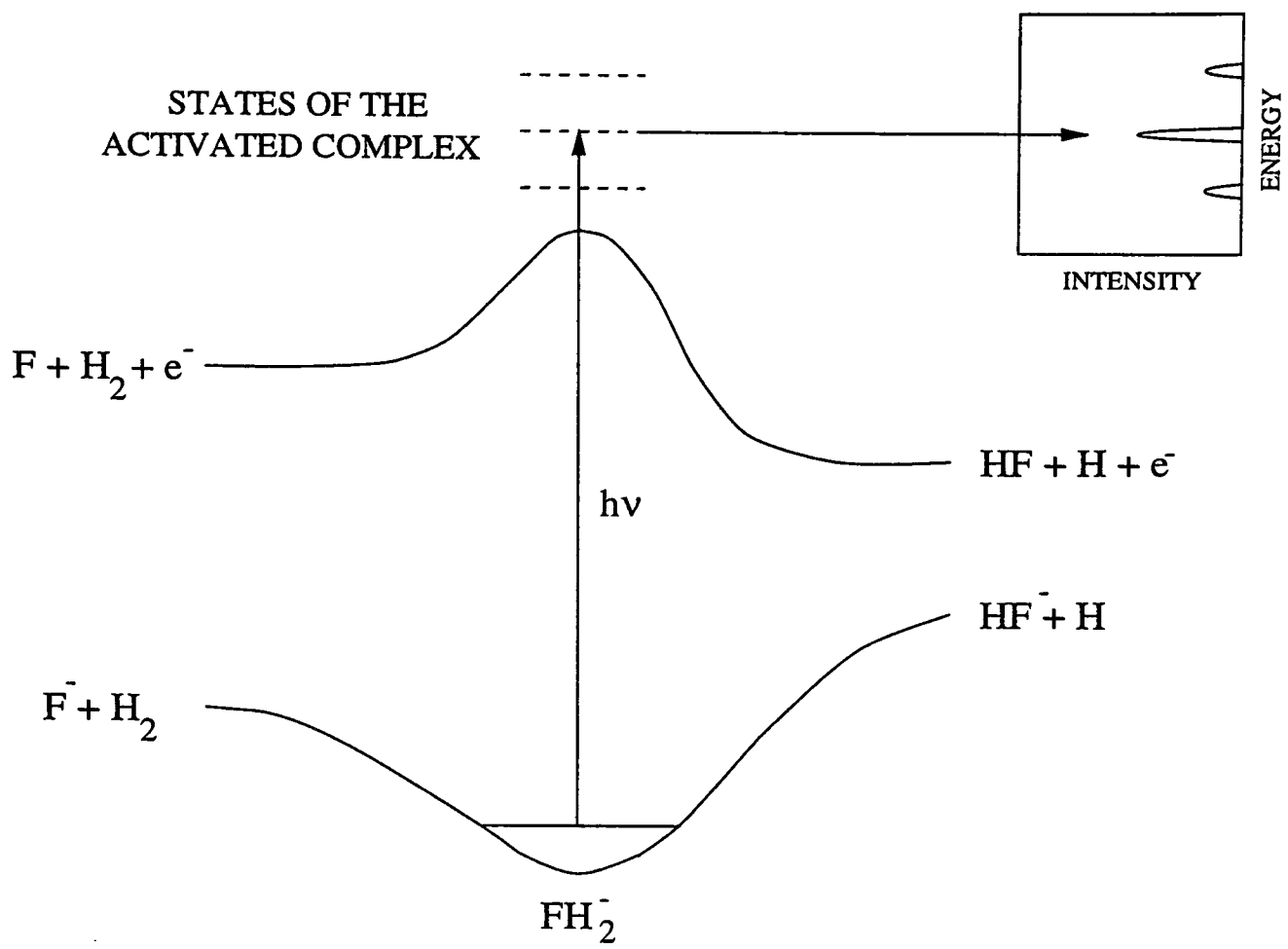


Figure 3.1 Schematic diagram of the photodetachment of a stable ion to produce an unstable neutral close to a reactive transition state.

of a stable anion such as FH_2^- to probe the transition state of a neutral reaction; $F + H_2 \longrightarrow HF + H$ in this case.

3.2 The $F + H_2 \longrightarrow HF + H$ reaction

The prototypical exothermic exchange reaction

$$F + H_2 \longrightarrow HF + H, \tag{3.1}$$

is one of the most thoroughly studied chemical reactions, and it has played a central rôle in the development of chemical reaction dynamics from its earliest stages [1]. A recent review by Manolopoulos [106] summarises the progress which has been made in understanding this reaction over the last few years, and thus only a brief overview

will be given here, sufficient to explain the motivation behind the calculations presented later in this chapter.

Recent interest in reaction (3.1) has centred around advances made both in experiment and in theory. On the experimental side, the FH_2^- anion photoelectron spectroscopy experiments of Neumark and co-workers (as described in section 3.1) have shed new light on the dynamics of the reaction in the transition state region [103, 107, 108], and the molecular beam experiments of Toennies and co-workers on the isotopically substituted F + D_2 reaction have achieved unprecedented product vibrational state resolution [109, 110]. On the theoretical side, a highly-correlated *ab initio* potential energy surface for the F + H_2 reaction has been calculated by Stark and Werner (SW) [111]. In contrast to dynamics calculations on earlier semi-empirical potential energy surfaces [107, 112], quantum mechanical calculations using the SW surface have been found to reproduce both the positions and the relative intensities of the peaks in the FH_2^- photoelectron spectrum [108]. Quasi-classical trajectory [113, 114, 115, 116] and quantum mechanical [117, 118] calculations on the SW surface have since also been found to give a satisfactory description of various other experimental properties of the F + H_2, F + D_2 and F + HD reactions, including product vibrational branching ratios, product angular distributions, and thermal rate constants.

The purpose of the work presented in this chapter is to try to answer an important question concerning the dynamics of the F + H_2 reaction: to what extent are quantum mechanical reactive scattering resonances implicated in experimentally-observable quantities? This question has been the subject of considerable discussion in the literature concerning the reaction [119]. For example, as a result of early dy-

namics calculations on various semi-empirical potential energy surfaces, resonances were thought to be implicated in both the 1985 molecular beam experiment of Lee and co-workers [120], and the 1991 anion photoelectron spectroscopy experiment of Weaver and Neumark [103]. However, this was subsequently shown not to be the case. The selective forward scattering of the HF($v' = 3$) product in the molecular beam experiment was eventually attributed to quantum mechanical tunnelling at high initial orbital angular momenta [118], while the dominant peaks in the FH_2^- anion photoelectron spectrum were assigned to direct scattering F + H_2 hindered-rotor states [107, 108, 118] based on calculations on the SW surface. Despite these findings, quantum mechanical resonances definitely do play a rôle in the dynamics of the reaction – they can be seen, for example, as peaks in plots of the cumulative $J = 0$ reaction probability as a function of energy [118] – and the key question is therefore whether or not these resonances can be detected experimentally.

Although quantum mechanical resonances are relatively easy to calculate theoretically they are extremely difficult to detect experimentally, largely due to the averaging over angular momenta mentioned in section 3.1 which tends to "wash out" resonance structure from full-collision experiments. This point is illustrated very clearly by the discussion in the literature concerning the possibility of observing resonances in the H + H_2 reaction [121, 122, 123, 124], the conclusion of which was that it would be necessary to obtain vibrationally and rotationally state-resolved differential cross sections as a function of collision energy in order to detect the resonances experimentally [124]. A molecular beam experiment of this type is currently impossible for the F + H_2 reaction and thus a different experimental strategy is required. In particular, we need an experiment which involves less averaging over angular momentum – anion photoelectron spectroscopy is the obvious choice.

The original suggestion that anion photoelectron spectroscopy could be used to observe reactive scattering resonances was in a paper by Clary and Connor on the IHI^- and $BrHBr^-$ systems [125]. Since then, Neumark and co-workers have applied the technique to a wide variety of systems including the IHI^- anion, and in the case of this system they have observed the symmetric stretch resonances which were predicted in reactive scattering calculations [126, 127, 128]. This success, added to the indication from *ab initio* calculations on the FH_2^- anion [129] that there is a fortuitously good overlap between the ground-state anion wavefunction and the transition state of the neutral reaction, meant that the photoelectron spectroscopy of FH_2^- was a natural way to try to observe quantum mechanical resonances in the $F + H_2$ reaction, and this was the intention of Weaver and Neumark when they carried out the FH_2^- experiment [103]. However, as described above, the photoelectron spectra of *para*- and *normal*-FH_2^- which have been measured so far have served simply to highlight the rôle of direct scattering $F + H_2$ hindered rotor states in the transition state region without giving any indication of the influence of resonances [108].

The motivation behind the calculations presented in this chapter was to discover whether the absence of any evidence for resonances in the available FH_2^- spectra could simply be a consequence of the low energy resolution (19 meV full width at half maximum) of the experiments performed to date. A *threshold* photodetachment experiment, such as that which has already been performed by Neumark and co-workers for IHI^- [128], would have an energy resolution of around 1 meV full width at half maximum. We therefore decided to carry out calculations of the photodetachment spectra of FH_2^- on the SW surface at this higher resolution to see whether resonances would be implicated by a threshold experiment.

3.3 Method and computational details

3.3.1 Introduction

Recall from chapter 2 that equations (2.13), (2.14) and (2.15) gave the Franck-Condon absorption spectrum from a single initial state $|\psi_i(0)\rangle$ as

$$P_i(E) = \lim_{\epsilon \to 0} \frac{1}{\pi\hbar} \mathrm{Re} \int_0^\infty e^{+iEt/\hbar} C_i(t) dt, \tag{3.2}$$

where $C_i(t)$ is defined as

$$C_i(t) = \langle \chi_i(0) | e^{-i(H - i\epsilon)t/\hbar} | \chi_i(0) \rangle. \tag{3.3}$$

In the application discussed in this chapter, H is the vibrational Hamiltonian ($J = 0$) for the upper F + H_2 potential energy surface, ϵ is a convergence factor discussed both in chapter 2 and later in this chapter, $|\chi_i(0)\rangle$ is the product of the electric dipole transition matrix element with the initial vibrational bound state of the FH_2^- anion $|\psi_i(0)\rangle$,

$$|\chi_i(0)\rangle = \boldsymbol{\mu}_{\tilde{f}\tilde{i}} \cdot \mathbf{e} |\psi_i(0)\rangle, \tag{3.4}$$

and E is the final reactive scattering energy relative to the bottom of the asymptotic F + H_2 valley.

In order to implement these equations, we shall make use of the usual assumptions that are used to simulate anion photoelectron spectra, which are discussed (and justified) in more detail in an article by Schatz [130]. In brief these are:

1. that the anion is sufficiently rotationally cold to be modelled by total angular momentum $J = 0$, and
2. that the electric dipole transition matrix element for the electronic transition is a constant function of both the nuclear coordinates in the Franck-Condon

region and the energy of the ejected photoelectron.

The first of these assumptions allows us to use the *vibrational* Hamiltonian in equation (3.3) above, while the second allows us to add the simplification that,

$$|\chi_i(0)\rangle = |\psi_i(0)\rangle, \tag{3.5}$$

since the electric dipole transition matrix element is held to be a constant which can be chosen for convenience to be unity. The expression for the photoelectron spectrum is thus as given in equation (3.2), but it is now used in conjunction with the following simplified expression for the correlation function,

$$C_i(t) = \langle\psi_i(0)|e^{-i(H-i\epsilon)t/\hbar}|\psi_i(0)\rangle. \tag{3.6}$$

3.3.2 Methodology

This section describes the method used to implement equations (3.2) and (3.6). We shall begin by describing the coordinates used in the calculations and then give the form of the Hamiltonian in these coordinates. Next we discuss the representation of the Hamiltonian, the initial wavefunction $|\psi_i(0)\rangle$, the propagation method, and the absorbing potential. Finally, we describe the convolution of the correlation function with a Gaussian in order to attain the energy resolution we require for the photoelectron spectra.

The calculations were carried out using mass-scaled Jacobi (MSJ) coordinates, (R, r, γ), of the F + H_2 reactant arrangement. The Jacobi coordinates, $(\tilde{R}, \tilde{r}, \gamma)$, of this arrangement are illustrated in figure 3.2, and the mass-scaled coordinates are related to the unscaled coordinates by multiplying the radial coordinates by mass-dependent parameters [97]. (This is discussed in detail in appendix B.) Ex-

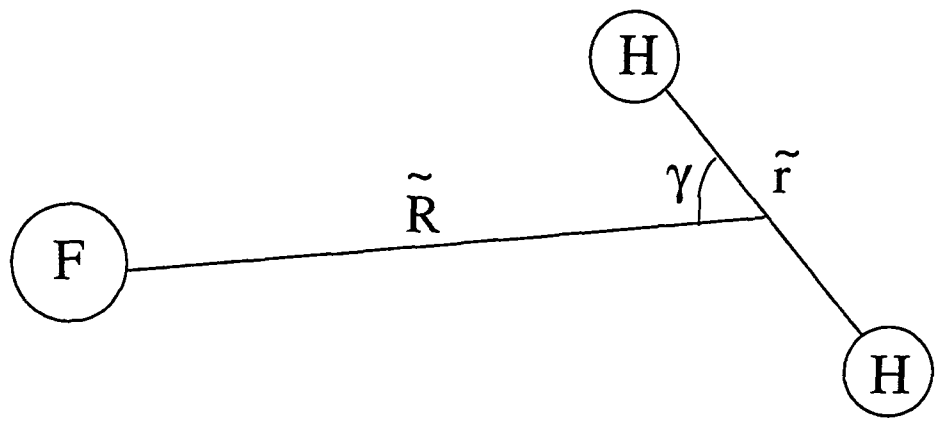


Figure 3.2 Jacobi coordinates of the F + H_2 reactant arrangement.

pressed in MSJ coordinates, the form of the Hamiltonian appropriate for the nuclear motion (within the Born-Oppenheimer approximation) is that which was given in equation (2.49), namely

$$H = -\frac{\hbar^2}{2\mu}\left(\frac{\partial^2}{\partial R^2} + \frac{\partial^2}{\partial r^2}\right) + \frac{\hat{j}^2}{2\mu r^2} + \frac{\hat{\ell}^2}{2\mu R^2} + V(R, r, \gamma), \tag{3.7}$$

where $\hat{j}$ is the rotational angular momentum operator associated with rotation of the vector $\boldsymbol{r}$, and $\hat{\ell}$ is the orbital angular momentum operator associated with rotation of the vector $\boldsymbol{R}$. The advantage of using mass-scaled coordinates is apparent in the fact that only one reduced mass, μ, appears in equation (3.7), where

$$\mu = \left(\frac{m_F m_H m_H}{m_F + m_H + m_H}\right)^{\frac{1}{2}}. \tag{3.8}$$

Since the photodetachment spectra to be modelled are for rotationally cold anions, the calculations are carried out for zero total angular momentum. In this case, the Hamiltonian can be written as

$$H = T + U, \tag{3.9}$$

where

$$T = -\frac{\hbar^2}{2\mu}\left(\frac{\partial^2}{\partial R^2} + \frac{\partial^2}{\partial r^2}\right), \tag{3.10}$$

and

$$U = +\frac{1}{2\mu}\left(\frac{1}{R^2} + \frac{1}{r^2}\right)\hat{j}^2 + V(R, r, \gamma). \tag{3.11}$$

Having obtained this expression for the Hamiltonian, the next step is to choose an appropriate representation for the problem. For the radial coordinates, R and r, we used particle-in-a-box discrete variable representations (DVRs) [131], while for the angular coordinate, γ, we used Legendre polynomial basis functions as a finite basis representation (FBR). In this mixed representation the Hamiltonian matrix is given by,

$$\begin{aligned} H_{p'q'j',pqj} &= (T_R)_{p'p}\delta_{q'q}\delta_{j'j} + (T_r)_{q'q}\delta_{p'p}\delta_{j'j} \\ &+ \frac{\hbar^2}{2\mu}\frac{j(j+1)}{R_p^2}\delta_{p'p}\delta_{q'q}\delta_{j'j} + \frac{\hbar^2}{2\mu}\frac{j(j+1)}{r_q^2}\delta_{q'q}\delta_{p'p}\delta_{j'j} \\ &+ V(R_p, r_q)_{j'j}\delta_{p'p}\delta_{q'q}, \end{aligned} \tag{3.12}$$

where R_p and r_q are the DVR grid points for the R and r dimensions respectively, $(T_R)_{p'p}$ and $(T_r)_{q'q}$ are matrix elements of the radial kinetic energy operators for which closed-form expressions in the DVR basis are given by Colbert and Miller [131], and j is the rotational angular momentum quantum number of the basis functions $\hat{P}_j(\cos\gamma) = \sqrt{j+\frac{1}{2}}P_j(\cos\gamma)$. The above representation is computationally attractive due to its sparsity which makes the repeated application of the Hamiltonian throughout the propagation of the wavepacket as efficient as possible.

We now move on to discuss the form of the initial wavepacket, denoted $|\psi_i(0)\rangle$ in equation (3.6). This wavepacket, the ground-state wavefunction of the collinear FH_2^- anion, was modelled in the harmonic normal mode approximation [112] such that the wavefunction was described as a simple harmonic oscillator in each degree of freedom,

$$|\psi_i(0)\rangle = \phi_R(R)\phi_r(r)\phi_\gamma(\gamma), \tag{3.13}$$

where

$$\phi_R(R) = \left(\frac{\alpha_R}{\pi}\right)^{\frac{1}{4}} \exp\left[-\frac{\alpha_R}{2}(R-R_0)^2\right], \tag{3.14}$$

$$\phi_r(r) = \left(\frac{\alpha_r}{\pi}\right)^{\frac{1}{4}} \exp\left[-\frac{\alpha_r}{2}(r-r_0)^2\right], \tag{3.15}$$

$$\phi_\gamma(\gamma) = (\alpha_\gamma)^{\frac{1}{2}} \left\{\exp\left[-\frac{\alpha_\gamma}{2}\gamma^2\right] + \exp\left[-\frac{\alpha_\gamma}{2}(\pi-\gamma)^2\right]\right\}. \tag{3.16}$$

The equilibrium geometry (R_0, r_0, collinear) and normal mode frequencies ($\omega_i = \hbar\alpha_i/\mu_i$, where μ_i is the reduced mass for mode i) were taken from the *ab initio* calculations of Simons and co-workers [129]. The same harmonic normal mode approximation was used in some earlier calculations of the FH_2^- spectrum at 19 meV energy resolution [108], and was found to reproduce the intensities of the peaks in both the *para* and *normal* experimental spectra. It therefore seems to be an acceptable approximation to the ground vibrational wavefunction of the anion [100].

The next aspect of the method to be discussed is the time-evolution implied by equation (3.2). This was performed using the symmetric split operator method [42, 132] with a partitioning of the Hamiltonian into radial kinetic energy (T) and potential and centrifugal energy (U) operators as indicated in equation (3.9),

$$\begin{aligned}\psi_i(t+\Delta t) &= e^{-iH\Delta t/\hbar}\psi_i(t) \\ &= e^{-iU\Delta t/2\hbar}e^{-iT\Delta t/\hbar}e^{-iU\Delta t/2\hbar}\psi_i(t) + O(\Delta t^3).\end{aligned} \tag{3.17}$$

Propagating a wavepacket through time on a finite grid (such as the DVR grid described above) will inevitably lead to the wavepacket eventually reaching the edge of the grid during the propagation. If this is not dealt with there will be unphysical reflections from the edge of the grid which will invalidate the results

of the calculation. To prevent this from occurring, the factor $e^{-\epsilon t/\hbar}$ is included in equation (3.6). Recall from chapter 2 that this factor guarantees the convergence of the integral over t in equation (3.2). The question is how best to represent this factor on the finite grid in R and r generated by the radial DVR, and the usual solution to this problem is to regard

$$V_{\text{abs}}(R, r) = -i\epsilon(R, r) \tag{3.18}$$

as a coordinate-dependent absorbing potential (also referred to as an "optical potential") which absorbs the wavepacket as it approaches the boundary of the grid. Appendix A deals with this issue in more detail so here we shall simply state that we used a numerically-optimised absorbing potential over the last 25% of the radial grid in R and r.

The final subject to be covered in this section is the convolution of the correlation function with a Gaussian in order to obtain a specified energy resolution in the photoelectron spectrum. As described in section 3.2, the chief motivation behind carrying out these wavepacket calculations lay in discovering whether quantum mechanical resonances would be implicated by photoelectron spectra recorded at higher resolution than the 19 meV full width at half maximum (FWHM) resolution achieved in experiments to date. The aim of this work was therefore first to reproduce the 19 meV spectra in order to confirm the validity of the method, and secondly to calculate photoelectron spectra of FH_2^- at the 1 meV (FWHM) resolution attainable in a threshold photodetachment experiment.

To achieve a particular energy resolution, the spectrum calculated is not simply given by the expression in equations (3.2) and (3.6) but is instead the convoluted

version,

$$\tilde{P}_i(E) = \lim_{\epsilon \to 0} \frac{1}{\pi\hbar} \mathrm{Re} \int_0^\infty e^{+iEt/\hbar} \tilde{C}_i(t) dt, \tag{3.19}$$

where

$$\tilde{C}_i(t) = e^{-t^2/2\tau^2} \langle \psi_i(0) | e^{-i(H - i\epsilon)t/\hbar} | \psi_i(0) \rangle. \tag{3.20}$$

By the convolution theorem [133], which states that the Fourier transform of a product of two functions is simply the convolution of the Fourier transforms of the individual functions, it can be seen that

$$\tilde{P}_i(E) = \lim_{\epsilon \to 0} \int_{-\infty}^{+\infty} g(E - E') P_i(E') dE', \tag{3.21}$$

where

$$\begin{aligned} g(E) &= \frac{1}{2\pi\hbar} \int_{-\infty}^{\infty} e^{+iEt/\hbar} e^{-t^2/2\tau^2} dt, \\ &= \frac{1}{\sqrt{2\pi\Delta E^2}} e^{-E^2/2\Delta E^2}, \end{aligned} \tag{3.22}$$

with

$$\Delta E = \frac{\hbar}{\tau}. \tag{3.23}$$

It can therefore be shown that equation (3.19) will produce a photoelectron spectrum with the correct energy resolution, for example FWHM = 1 meV or 19 meV, providing τ is specified as

$$\tau = \frac{\sqrt{\ln 256}\, \hbar}{\mathrm{FWHM}}. \tag{3.24}$$

The next section gives some numerical details of the calculations carried out, in particular the various parameters required for convergence.

3.3.3 Numerical details

Photoelectron spectra were calculated for *para*- and *ortho*-FH_2^- at 19 meV and 1 meV energy resolution (FWHM). A summary of the converged parameters for the

FWHM/eV	R_{max}/a_0	r_{max}/a_0	Δt/fs	Total time/ps
0.019	10	5	0.66	0.24
0.001	12	10	0.20	3.0

Table 3.1 Parameters for calculation of FH_2^- photodetachment spectra.

calculations is given in table 3.1. In this table, R_{max} is the size of the DVR grid in R (where R ranges from 0 to R_{max}), r_{max} is the size of the DVR grid in r (where r ranges from 0 to r_{max}), Δt is the time-step used in the split-operator propagation, and the final column gives the total propagation time needed to obtain a converged spectrum. It was found that converged results were obtained by using up to 73 DVR points in R (fewer than this were required for the lower resolution spectra), up to 61 DVR points in r, and up to 73 Legendre polynomials in $\cos\gamma$ (accounting for the permutation symmetry of the two hydrogen atoms, which restricts the angular basis to even polynomials for *para*-FH_2^- and odd polynomials for *ortho*-FH_2^-).

3.4 Results: calculated photoelectron spectra

The calculated photoelectron spectra of *para*-FH_2^- at 19 meV and 1 meV (FWHM) energy resolution are shown in figures 3.3 and 3.4 respectively, while those for *ortho*-FH_2^- at the same resolutions are shown in figures 3.5 and 3.6. Recall that 19 meV resolution corresponds to the experimental resolution in the region of the dominant peaks in the best available FH_2^- spectra obtained using a conventional photodetachment experiment [108]. This is the resolution which was used in earlier simulations of the FH_2^- system using a time-independent reactive scattering method [108], and the present simulations agree with these earlier simulations to graphical accuracy.

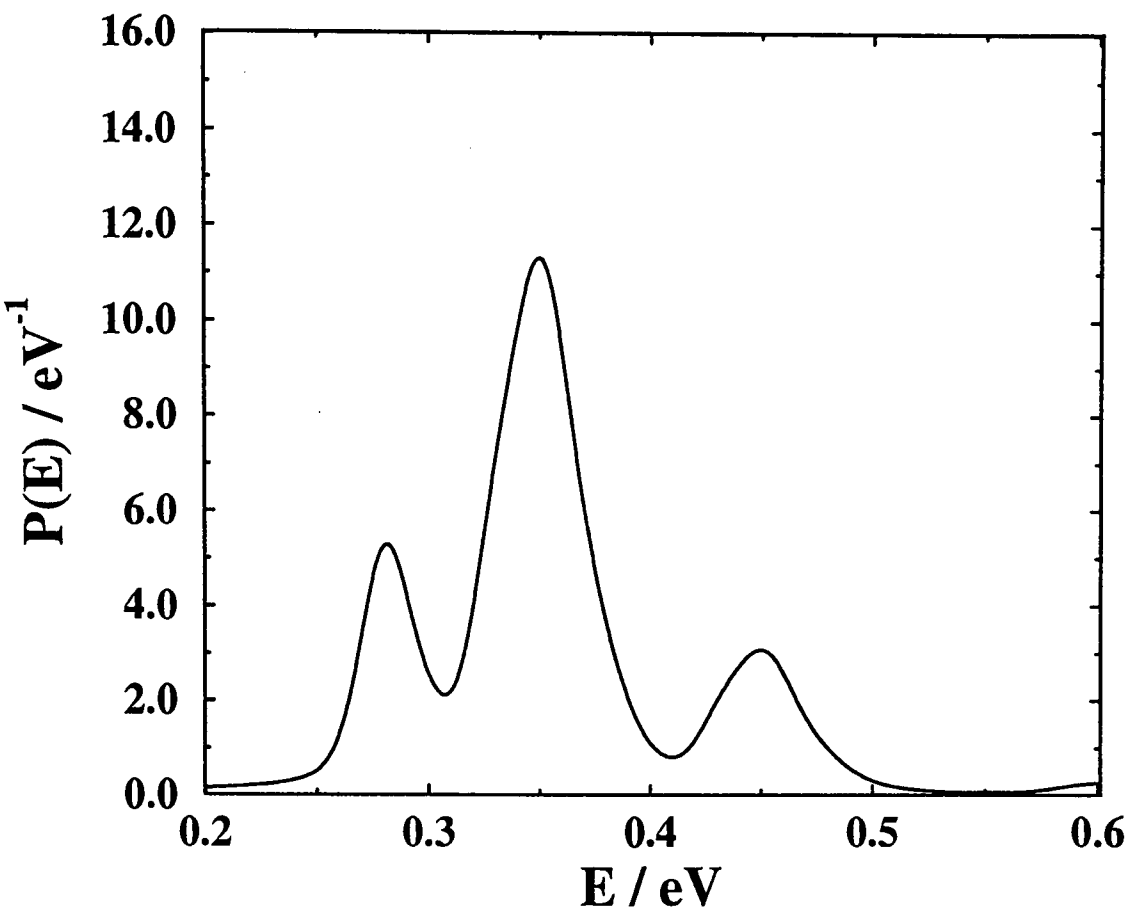


Figure 3.3 Photoelectron spectrum of *para*-FH_2^- at 19 meV (FWHM) resolution.

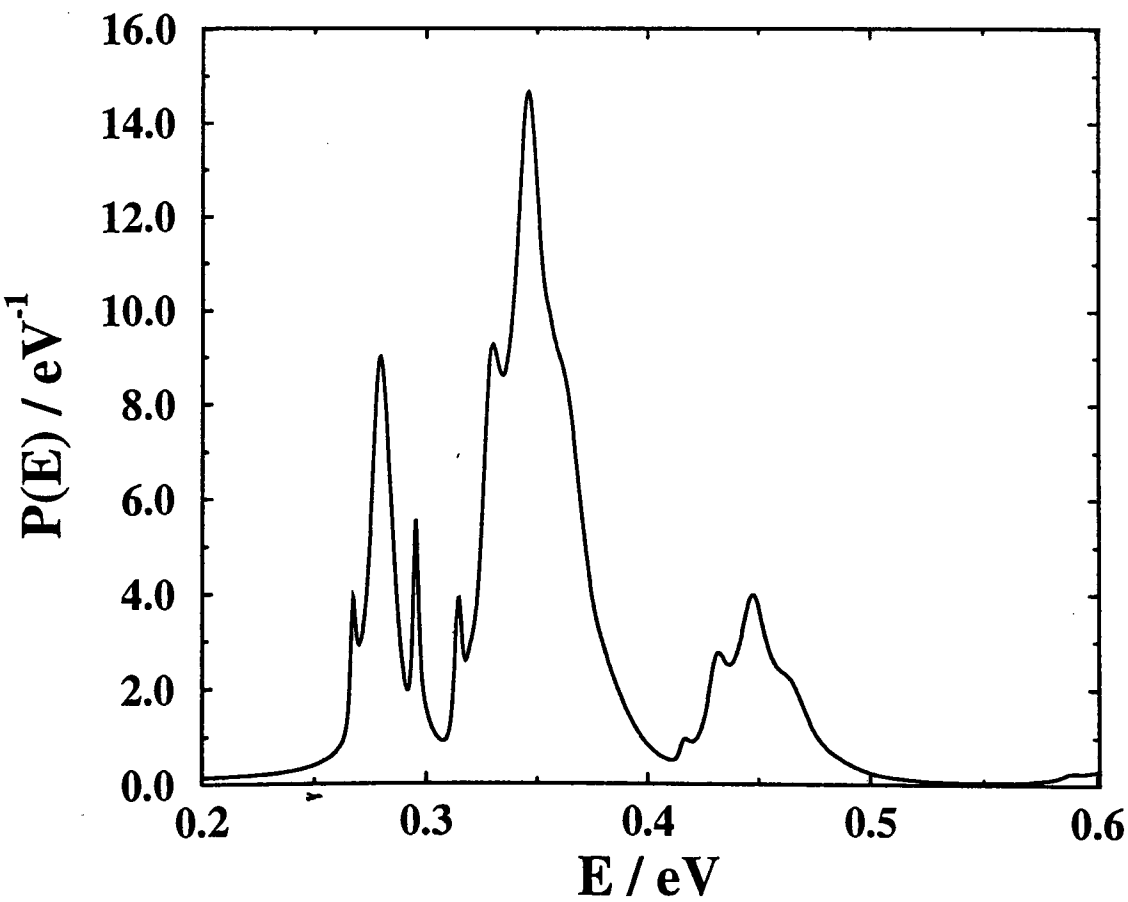


Figure 3.4 Photoelectron spectrum of *para*-FH_2^- at 1 meV (FWHM) resolution.

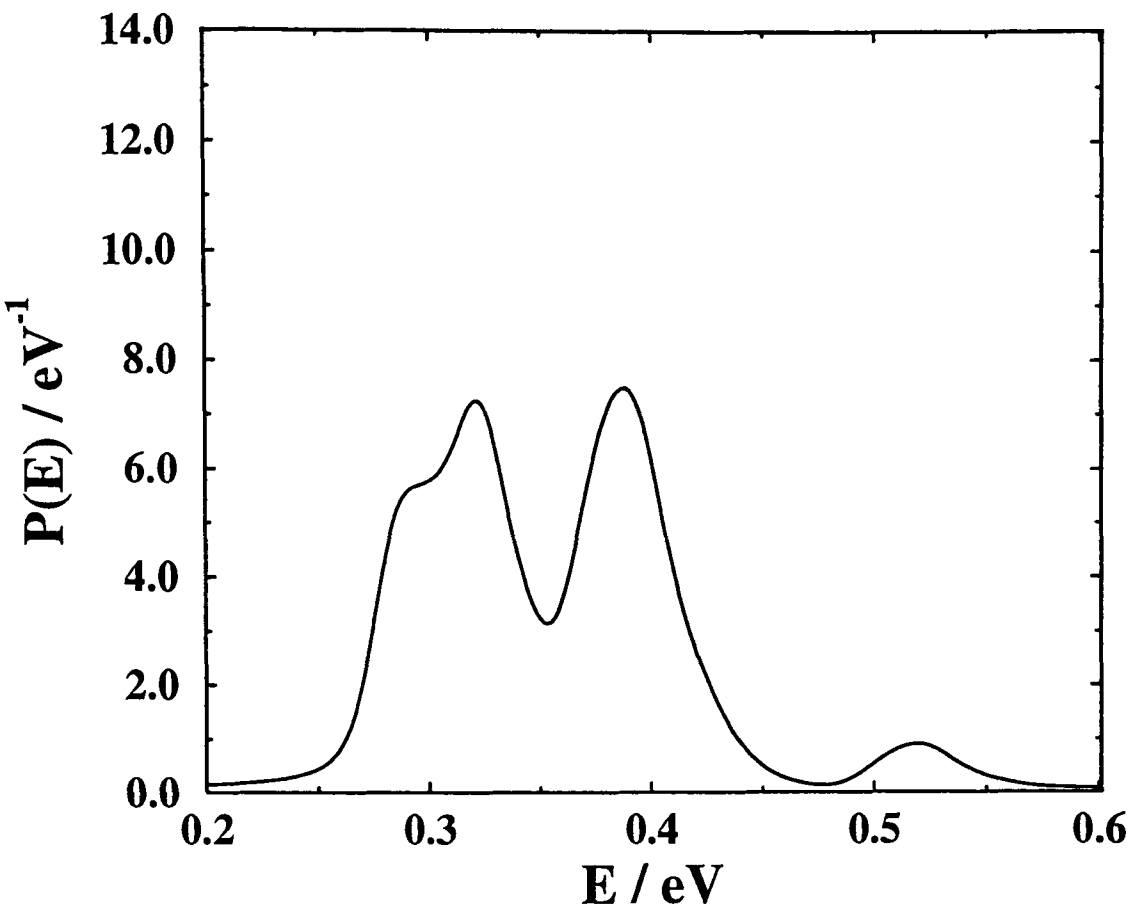


Figure 3.5 Photoelectron spectrum of *ortho*-FH_2^- at 19 meV (FWHM) resolution.

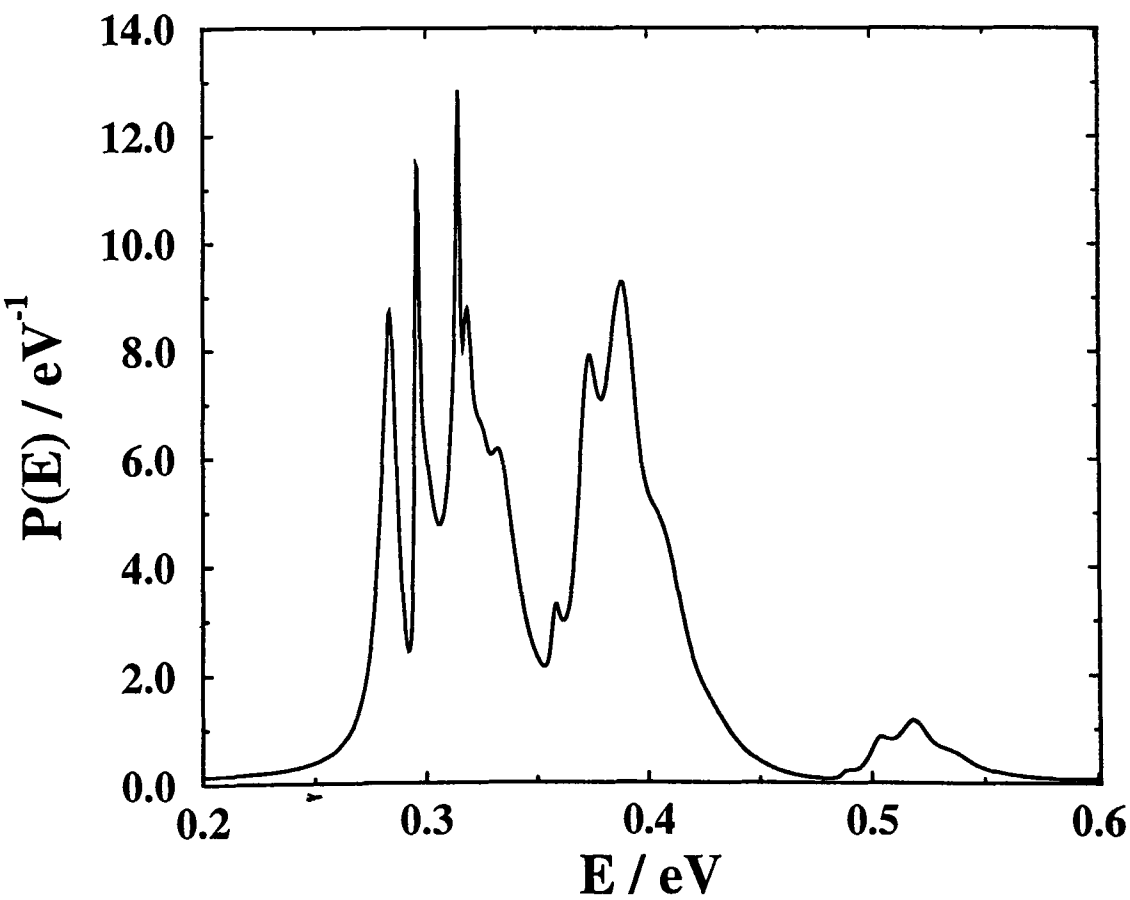


Figure 3.6 Photoelectron spectrum of *ortho*-FH_2^- at 1 meV (FWHM) resolution.

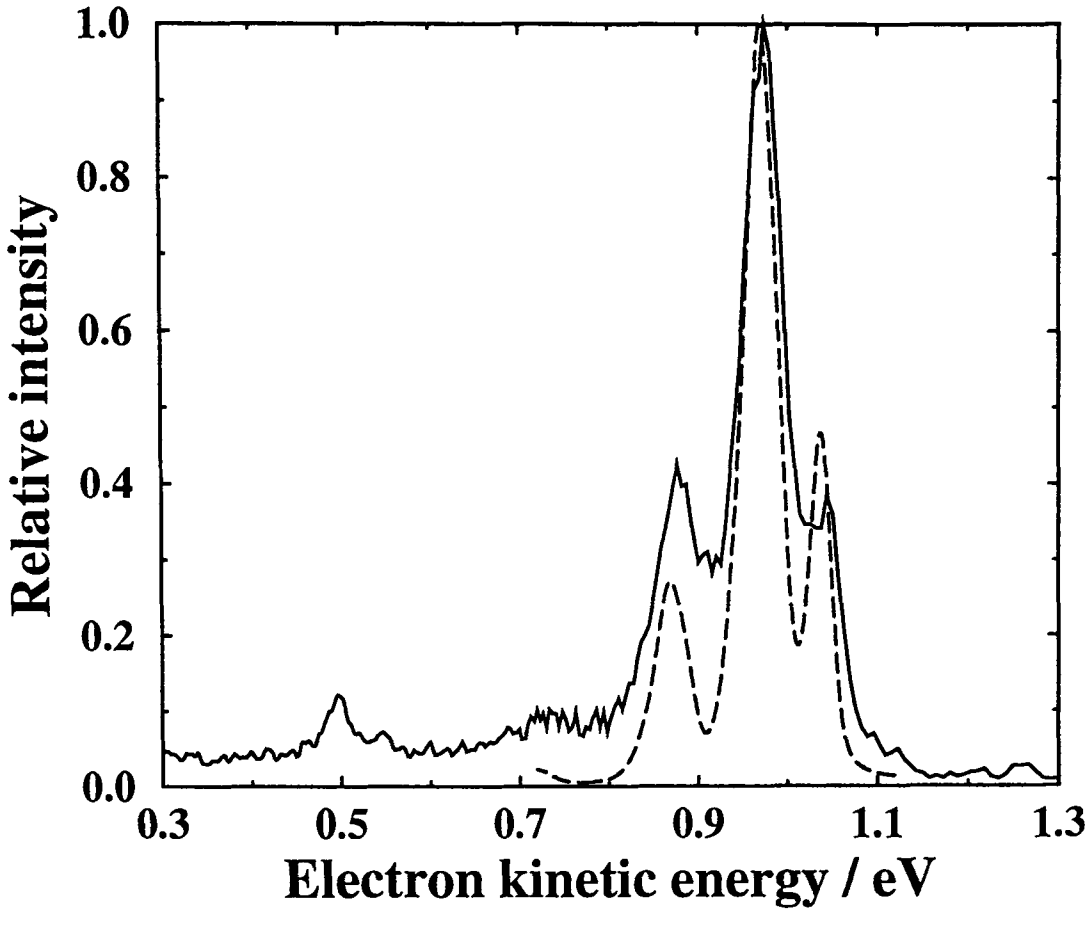


Figure 3.7 Comparison between experimental (solid) and theoretical (dashed) photoelectron spectra for *para*-FH_2^-. The theoretical spectrum has 19 meV resolution (FWHM), and the two spectra have been scaled such that their strongest peaks have unit intensity.

The 19 meV resolution spectrum of *para*-FH_2^- is compared in figure 3.7 with the best available experimental results [108]. In order to make this comparison we have used the following relationship between the electron kinetic energy eKE and the scattering energy E [108]:

$$e\mathrm{KE} = h\nu - D_0(\mathrm{FH}_2^-) - \mathrm{EA(F)} + \mathrm{ZPE(H_2)} - E, \tag{3.25}$$

where $D_0(\mathrm{FH}_2^-)$ is the dissociation energy of the anion, EA(F) is the electron affinity of the fluorine atom, and $\mathrm{ZPE(H_2)}$ is the zero-point energy of the H_2 molecule. Since $D_0(\mathrm{FH}_2^-)$ is not well characterised by the *ab initio* calculations of Simons and coworkers [129], we have used this parameter as a variable with which to shift the theoretical spectrum along the energy axis in order to obtain the best possible fit

to the experimental spectrum.

The calculated 1 meV resolution spectra in figures 3.4 and 3.6 constitute the new results of this work [100]. These spectra reveal the sort of structure one would expect to see in a *threshold* photodetachment experiment of the kind already performed by Neumark and co-workers on IHI^- [128]. Clearly, the higher resolution spectra in figures 3.4 and 3.6 contain significantly more structure than the low resolution spectra in figures 3.3 and 3.5, and this new structure is sufficiently intense and well resolved to be detected experimentally.

3.5 Analysis: energy-dependent wavefunctions

3.5.1 Method of analysis

The simplest and most illuminating way to assign the structure in figures 3.4 and 3.6 is based on the analysis of the $HOCl^-$ photoelectron spectrum by Davis and co-workers [134]. In the present (time-dependent) context, the central idea of this analysis is the observation that equations (3.2) and (3.6) can be re-written as

$$P_i(E) = \langle \psi_i(0) | \psi_i(E) \rangle \,, \tag{3.26}$$

where

$$|\psi_i(E)\rangle = \frac{1}{\pi\hbar} \mathrm{Re} \int_0^\infty \exp[+i(E + i\epsilon - H)t/\hbar] \, |\psi_i(0)\rangle \, dt, \tag{3.27}$$

is an energy-dependent scattering wavefunction that can be computed from the evolving wavepacket. It follows that the peaks in the photoelectron spectrum occur at energies for which there is a particularly good overlap between $|\psi_i(0)\rangle$ and $|\psi_i(E)\rangle$, and that the peaks can therefore be assigned by examining the nodal structure of the wavefunctions $|\psi_i(E)\rangle$ at each peak energy E.

In practice, we have found that it is more useful not to look at $|\psi_i(E)\rangle$ directly, but instead to look at its second energy derivative, *i.e.*,

$$P_i''(E) = \langle \psi_i(0) | \psi_i''(E) \rangle \,, \tag{3.28}$$

where

$$|\psi_i''(E)\rangle = -\frac{1}{\pi\hbar^3} \mathrm{Re} \int_0^\infty t^2 \exp[+i(E + i\epsilon - H)t/\hbar] \, |\psi_i(0)\rangle \, dt. \tag{3.29}$$

The reason for this is that several of the narrow peaks in figures 3.4 and 3.6 occur on the shoulders of broader peaks. If one looks directly at $|\psi_i(E)\rangle$ at the central energy E of such a narrow peak, the resulting assignment is often ambiguous because of a large background contribution from the underlying broad peak. However, the background contribution is significantly reduced when one looks at the second derivative $|\psi_i''(E)\rangle$, because the component of the wavefunction $|\psi_i(E)\rangle$ associated with the broad peak is a comparatively slowly varying function of energy. Another way of looking at this which leads to the same conclusion is to note that the t^2 in the integrand of equation (3.29) preferentially weights the long time dynamics responsible for narrow features in the spectrum $P_i(E)$.

This section has outlined the method used to analyse the structure in the high resolution photodetachment spectra of *ortho-* and *para*-FH_2^-. In the following section some examples will be given of wavefunctions $|\psi_i''(E)\rangle$ obtained using this analysis, and of their physical interpretation.

3.5.2 Results and interpretation

In order to illustrate the results of the analysis carried out as described in the previous section, figure 3.8 shows collinear contour plots of the wavefunctions $|\psi_i''(E)\rangle$ at

the energies of the first three peaks in the high resolution *para*-FH_2^- photoelectron spectrum in figure 3.4. These three peaks were chosen because they are representative of the dynamics of the F + H_2 reaction accessed by FH_2^- photodetachment. The wavefunction contour plots shown should be viewed in conjunction with figures 3.9 and 3.10, which show collinear contour plots of the initial anion wavefunction $|\psi_i(0)\rangle$ and of the SW potential energy surface.

The important features to concentrate on in these figures are the fact that the initial anion wavefunction is fortuitously localised in the neutral transition state region at the end of the F + H_2 reactant valley, and the fact that there are van der Waals wells in both the F + H_2 reactant and H + HF product valleys on the neutral surface. The van der Waals well in the reactant valley has a T-shaped equilibrium geometry at $R = 6.59$ bohr, $r = 1.02$ bohr and $\gamma = 90°$, and a well depth of 16 meV. However, it is also apparent at collinear geometries as shown in figure 3.10(b). The van der Waals well in the product valley has a collinear equilibrium geometry at $R = 5.28$ bohr and $r = 3.03$ bohr and a well depth of 11 meV as shown in figure 3.10(c).

A resonance in the reactant valley

Figure 3.8(a) shows the wavefunction $|\psi_i''(E)\rangle$ at the energy $E = 0.268$ eV of the first sharp peak in the high resolution *para*-FH_2^- photoelectron spectrum in figure 3.4. This peak is clearly due to a quasi-bound resonance state that is localised in the van der Waals well region in the reactant valley. Since the wavefunction is nodeless, the quantum numbers of the state are $v = 0$ in the H–H stretch coordinate r and $t = 0$ in the F–H_2 van der Waals stretch coordinate R. Furthermore, the fact that this state occurs at such low energy suggests that its remaining hindered H_2 rotational quantum number can only be $j = 0$, and this assignment is confirmed by examining

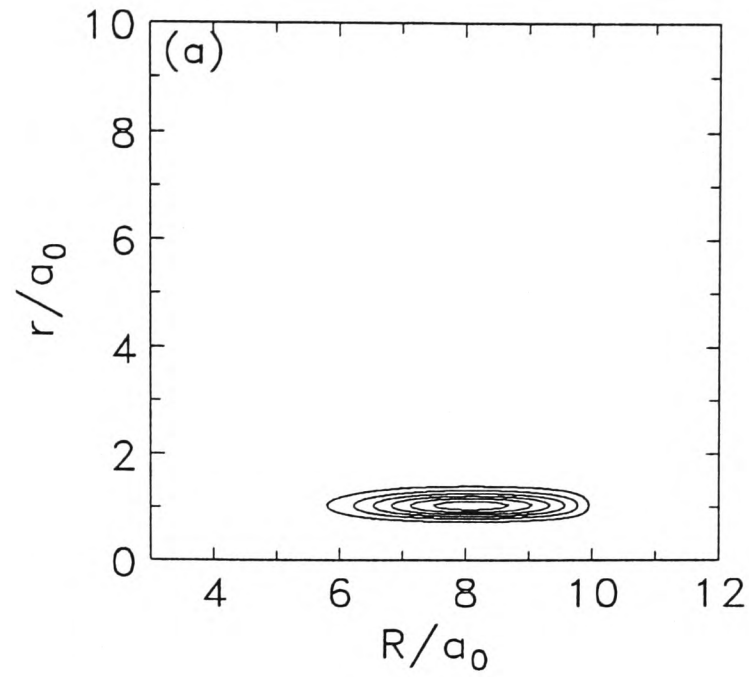


Figure 3.8 Wavefunctions $|\psi_i''(E)\rangle$ corresponding to the first three peaks in the high resolution *para*-FH_2^- photoelectron spectrum in figure 3.4. (a) A reactant resonance at $E = 0.268$ eV, (b) a direct scattering state at $E = 0.280$ eV, and (c) a product resonance at $E = 0.294$ eV.

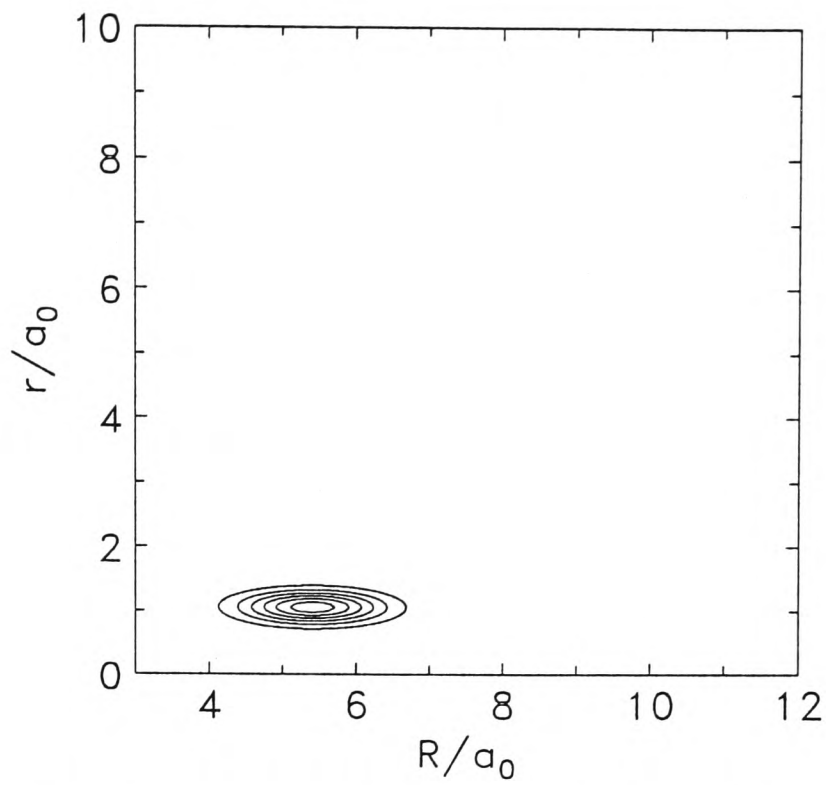
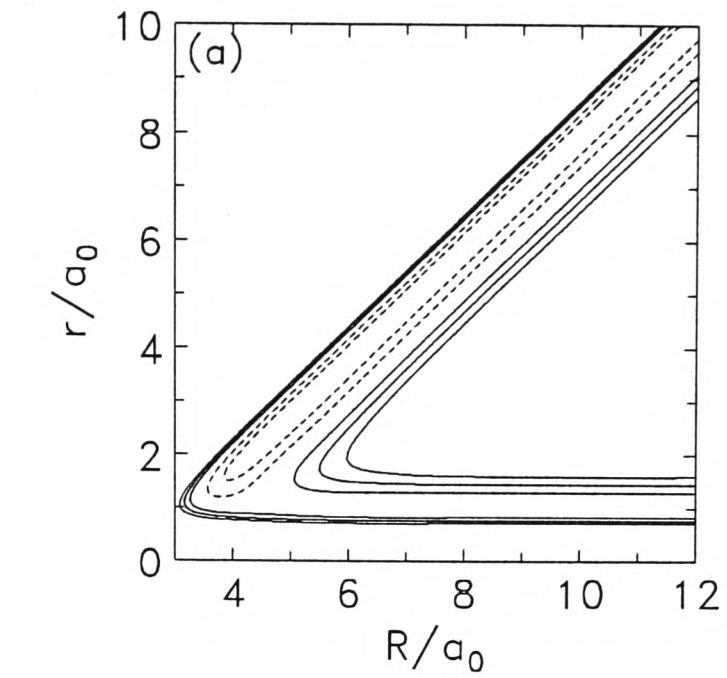
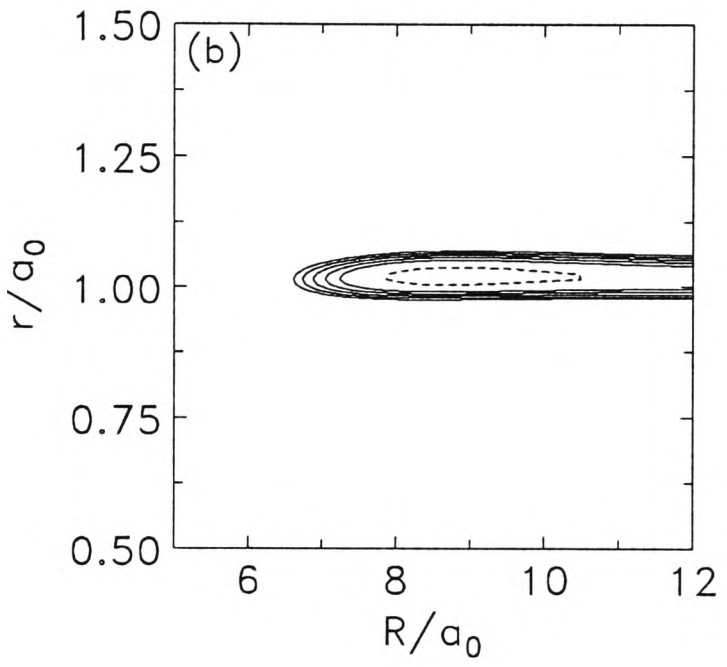


Figure 3.9 Collinear contour plot of the initial anion wavefunction $|\psi_i(0)\rangle$ as a function of the mass-scaled Jacobi coordinates R and r of the reactant arrangement.

the nodal structure of $|\psi_i''(E)\rangle$ as a function of γ. The overall assignment of the state in terms of F + H_2 reactant quantum numbers is thus $(v, j, t) = (0, 0, 0)$.

Strictly speaking, this particular state is not a reactive scattering resonance because the corresponding peak in figure 3.4 occurs below the threshold for the F + H_2 ($v = j = 0$) reaction. The only way in which the state can decay is therefore by tunnelling through the reaction barrier to the (exothermic) H + HF product arrangement, and one might not immediately expect it to have any impact on quantum reactive scattering calculations on the SW surface. However, since the state occurs very close to the reaction threshold and it is a resonance with a finite energy width, it does in fact have a small component that lies above the threshold energy. This may therefore explain why there is a small cumulative reaction probability peak just above the F + p-H_2 reaction threshold in calculations on the SW surface which it is difficult to account for in any other way [118]. In any event, the state shown in





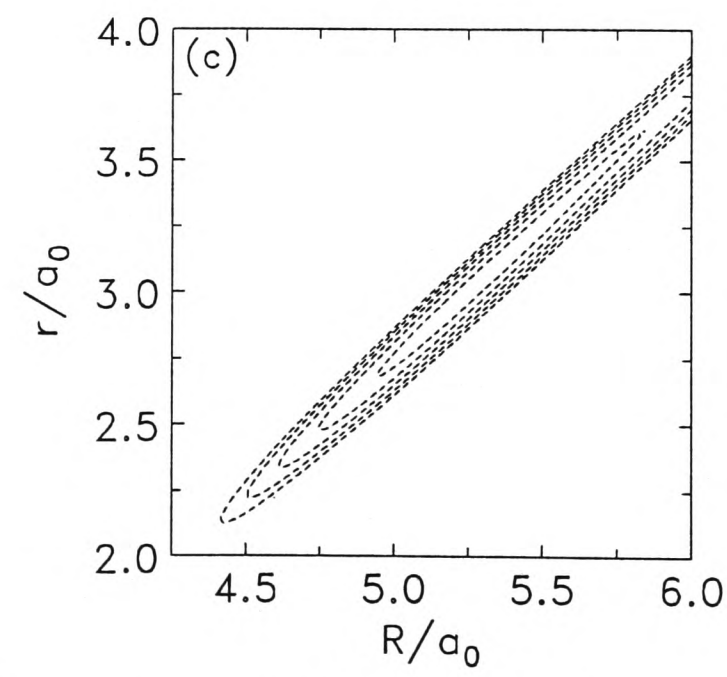


Figure 3.10 Collinear contour plot of the SW potential energy surface (a), with expansions of the reactant and product van der Waals well regions in panels (b) and (c). Solid contours correspond to positive energies and dashed contours to negative energies relative to the bottom of the asymptotic F + H_2 reactant valley.

figure 3.8(a) is clearly accessed in the 1 meV FH_2^- photodetachment spectrum in figure 3.4, and one might also expect it to appear as a sharp resonance feature in H + HF inelastic scattering calculations.

A delocalised direct scattering state

The next peak in figure 3.4 is the rather broader peak at E=0.280 eV. Figure 3.8(b) shows the corresponding wavefunction $|\psi_i''(E)\rangle$, which has a significant amplitude throughout the reaction coordinate and therefore a manifestly different origin from the localised resonance state in figure 3.8(a). This is simply the F + $H_2(v=0, j=0)$ direct scattering state that has been assigned previously to the first peak in the low resolution *para*-FH_2^- photoelectron spectrum [118]. It is clear from figure 3.8(b) that the state is nodeless in the H–H stretch coordinate r in the transition state region, and therefore has the quantum number $v = 0$. A similar plot of $|\psi_i''(E)\rangle$ as a function of R and γ in the transition state region confirms that the hindered H_2 rotational quantum number is $j = 0$. This completes the assignment, because the state is a direct scattering state and is not quantised along the reaction coordinate.

The reason why the wavefunction in figure 3.8(b) gives rise to a peak in the photoelectron spectrum is that it has both a significant amplitude and a long local de Broglie wavelength along the reaction coordinate in the transition state region, and therefore it has a good Franck-Condon overlap with the initial anion wavefunction. According to this argument, one would expect to see a similar direct scattering peak in the photoelectron spectrum each time an adiabatic reaction channel becomes energetically accessible in the transition state region [135]. The wavefunction in figure 3.8(b) is the first of these direct scattering states with transition state quantum numbers $(v, j) = (0, 0)$; the next two broad peaks at E=0.346 and 0.448 eV in the

para-FH_2^- photoelectron spectrum in figure 3.4 are due to similar direct scattering states with quantum numbers $(v, j) = (0, 2)$ and $(0, 4)$. These broad peaks clearly dominate the low resolution spectrum in figure 3.3, which can therefore be assigned simply to a direct scattering hindered-rotational progression as has been argued previously [107, 108, 118].

A resonance in the product valley

The third and final panel of figure 3.8 shows yet another aspect of the calculated F + H_2 reaction dynamics that should be accessible to a threshold photodetachment experiment. The wavefunction $|\psi_i''(E)\rangle$ shown in this figure corresponds to the third peak in the *para*-FH_2^- photoelectron spectrum in figure 3.4, which is centred at E=0.294 eV. Clearly, this peak is again due to a quasi-bound resonance state, but one that is localised this time in the van der Waals well region of the H + HF product valley. The nodal structure in figure 3.8(c) shows that the H–F stretch and H–HF van der Waals stretch quantum numbers of the state are $v' = 3$ and $t' = 0$, respectively, and an examination of the nodal structure of $|\psi_i''(E)\rangle$ as a function of the product H–HF Jacobi angle γ' reveals that the remaining (bending or HF hindered rotational) product quantum number is $j' = 0$. The overall assignment of the state in terms of H + HF product quantum numbers is thus $(v', j', t') = (3, 0, 0)$.

This assignment is the same as the earlier assignment of a peak at E=0.293 eV in the F + H_2 cumulative reaction probability [118], which was attributed in reference [118] to a Feshbach resonance (for total angular momentum $J = 0$) associated with the opening of the HF($v' = 3$) product manifold. It is therefore particularly compelling to note that there is a small component of the wavefunction $|\psi_i''(E)\rangle$ at large H–HF distances in figure 3.8(c) which has only two nodes in the H–F product vibrational

coordinate r'. The explanation for this is simply that the energy of the state lies below the threshold for the production of H + HF($v' = 3$), and the state therefore decays predominantly into H + HF($v' = 2$) by vibrational predissociation as one would expect for a Feshbach resonance [11].

Summary of the wavefunctions $|\psi_i''(E)\rangle$

These three examples give a clear overall picture of the F + H_2 reaction dynamics that is accessed in the high resolution FH_2^- photoelectron spectra given in figures 3.4 and 3.6. Although the assignments are not always so unambiguous, all of the other peaks in these spectra can be assigned in a similar way to resonance states that are localised in the reactant valley (with approximate reactant quantum numbers v, j and t), direct scattering states (with approximate transition state quantum numbers v and j), or resonance states that are localised in the product valley (with approximate product quantum numbers v', j' and t'). These assignments are summarised for both *para*- and *ortho*-FH_2^- in table 3.2.

The only observation from this table that needs any further comment is the fact that the product resonances occur at the same energies in both spectra, whereas the direct scattering peaks and the reactant resonances occur at different energies for *ortho*- and *para*-FH_2^- on account of their different hydrogen atom permutation symmetries. The product resonances appear to be unaffected by the permutation symmetry because they are localised sufficiently far out in the degenerate product valleys for the tunnelling splitting that would differentiate between the *ortho* and *para* cases to be too small to be resolved in figures 3.4 and 3.6.

One caveat that should be made about these calculations is that the positions and

Peak position/eV		Assignment	Quantum numbers
para-FH_2^-	*ortho*-FH_2^-		
0.268		reactant resonance	$(v,j,t)=(0,0,0)$
0.280		direct scattering	$(v,j)=(0,0)$
	0.283	direct scattering	$(v,j)=(0,1)$
0.294	0.294	product resonance	$(v',j',t')=(3,0,0)$
0.315	0.315	product resonance	$(v',j',t')=(3,2,0)$
	0.318	product resonance	$(v',j',t')=(3,2,1)$
0.331	0.331	product resonance	$(v',j',t')=(3,3,0)$
0.346		direct scattering	$(v,j)=(0,2)$
	0.359	reactant resonance	$(v,j,t)=(0,3,0/1)^\dagger$
	0.374	reactant resonance	$(v,j,t)=(0,3,1/2)^\dagger$
	0.389	direct scattering	$(v,j)=(0,3)$
0.417		reactant resonance	$(v,j,t)=(0,4,0/1)^\dagger$
0.432		reactant resonance	$(v,j,t)=(0,4,1/2)^\dagger$
0.448		direct scattering	$(v,j)=(0,4)$
	0.489	reactant resonance	$(v,j,t)=(0,5,0/1)^\dagger$
	0.504	reactant resonance	$(v,j,t)=(0,5,1/2)^\dagger$
	0.519	direct scattering	$(v,j)=(0,5)$

Table 3.2 Assignment of the high resolution FH_2^- photodetachment spectra in figures 3.4 and 3.6. (A dagger (†) indicates that the assignment of the F–H_2 van der Waals stretch quantum number t is ambiguous in this case because of a large background contribution to $|\psi_i''(E)\rangle$ from the underlying direct scattering peak.)

widths of the predicted resonances will be a highly sensitive function of the neutral $F + H_2$ potential energy surface. However, this caveat is mitigated to some extent by the fact that the present low resolution FH_2^- photoelectron spectra agree very well with the corresponding experimental spectra [108] (see also figure 3.7), and these low resolution spectra contain unresolved resonance contributions. Indeed the expected sensitivity of the resonance positions and widths to the reactant and product van der Waals well regions of the $F + H_2$ potential energy surface is all the more reason to detect them experimentally.

3.6 Discussion: recent work on $F + H_2$

Since the publication of the work presented in this chapter [100], there have been several new papers in the literature concerning the $F + H_2$ reaction, including a couple which are of particular relevance to the calculations presented above. In this section a short general review of these recent publications will preceed a more detailed discussion of the two papers most closely related to the work in this chapter.

Recent papers include a review of the available $F + H_2$ kinetics data [136] as well as new work on both the experimental and theoretical sides. The experimental papers include work on product state-selected angular distributions [137, 138], nascent rovibrational HF distributions [139], and absolute cross sections for the deuterium-substituted reaction $F + D_2 \rightarrow DF + D$ [140]. On the theoretical side, quasiclassical trajectories (QCT) have been used to study product rotational polarisation effects [141], while in another paper comparisons have been made between QCT and quantum mechanical simulations of molecular beam experiments [142]. Skodje and co-workers [143] have applied spectral quantization to the FH_2^- photodetach-

ment process and examined the origin of peaks in the photodetachment spectra for the collinear system. They have also applied spectral control theory to optimise the information content of the collinear photodetachment spectrum by varying the initial anion wavefunction, and they have shown how to calculate the infra-red pulse which would be required to create such a non-stationary initial state. Finally, a recent *ab initio* study of F + H_2 [144] has found extremely good quantitative agreement with the calculations of Stark and Werner [111] which underlie the surface used in the work presented in this chapter.

The first paper to be discussed in more detail is that of Founargiotakis *et al.* [145] who calculated bifurcation diagrams of periodic orbits for the collinear FH_2 system using the 5SEC potential energy surface [146]. They found that the principal families of periodic orbits originate in the van der Waals minima of the reactant and product channels and at the saddle point between the two minima. The authors suggest a correspondence between the reactant and product resonance wavefunctions generated by our calculations (figures 3.8(a) and 3.8(c)) and the periodic orbits localised in the reactant and product van der Waals minima respectively. They also suggest a relationship between their "saddle node" periodic orbits and our direct scattering states such as that shown in figure 3.8(b), although of course a direct comparison between the two calculations is difficult due to the different dimensionalities and potential energy surfaces used.

We now turn to the paper of Hartke and Werner [147] in which they have performed time-dependent quantum mechanical simulations of the FH_2^- photodetachment spectra using a method almost identical to that used in our calculations. The motivation for this work was to improve the correspondence between the theoretical and exper-

imental spectra, and in particular to improve the relative intensities and positions of the theoretical peaks. There are two main differences between these calculations and ours. First, while we used a harmonic normal mode approximation for the initial anion wavefunction, Hartke and Werner calculated an "exact" vibrational wavefunction on a new *ab initio* surface for the anion [148]. This not only allowed them to take into account the anharmonicity of the anion wavefunction, but it also meant that it was no longer necessary to fit the peak positions of the spectra to the experimental results; the absolute energies were fully determined by the new calculations without the need to use $D_0(FH_2^-)$ as a fitting parameter. The second difference between the two sets of calculations is that we used the original Stark and Werner surface for the neutral species (SW), whereas Hartke and Werner used a new surface (HSW) [148] which incorporates an approximate (adiabatic) spin-orbit correction to account for the open-shell nature of $F(^2P)$ in the reactant channel. The consequences of these two differences will now be discussed.

On comparing the theoretical results with the low resolution experimental spectra (19 meV FWHM), the new calculations show a small improvement in the relative peak intensities, which Hartke and Werner attribute to their inclusion of the anharmonicity of the anion wavefunction [147]. The main effect of the use of the spin-orbit correction in the new neutral surface (HSW) appears to be that it brings the relative energies of the peaks into better agreement with experiment, although this effect is small. A comparison of the high resolution spectra (1 meV FWHM) of Hartke and Werner with those presented in this chapter shows that the intensities of the sharp peaks corresponding to resonances localised in the van der Waals well regions of the reactant and product valleys are lower in the new calculations than in our calculations. This is attributed by Hartke and Werner to the increased barrier

height of the HSW neutral surface compared with the SW surface. They propose that an increased barrier height has the effect of imparting more kinetic energy to the initial wavepacket and that trapping of parts of the wavepacket in quasi-bound states is thus less pronounced.

To summarise the calculations of Hartke and Werner, they show small improvements over the calculations presented in this chapter in the relative peak intensities when comparing the results with the low resolution experimental spectra. They also determine absolute peak energies without recourse to using $D_0(\mathrm{FH_2^-})$ as a fitting parameter, and they achieve good agreement with experiment for the peak positions.

In conclusion, this section has reviewed the recent work on the F + H_2 reaction which has been published since the calculations in this chapter were carried out. Particular emphasis has been placed on discussing the calculations of Hartke and Werner which are very similar to those carried out by us but use a different anion wavefunction and a new potential energy surface for the neutral system. The results of these calculations have been compared to our results and the differences discussed.

3.7 · Conclusions

In this chapter, we have calculated and analysed the photoelectron spectra of *para*- and *ortho*-$\mathrm{FH_2^-}$, both at the 19 meV (FWHM) resolution which has already been achieved in a conventional photodetachment experiment [108], and at the 1 meV (FWHM) resolution which should be attainable in a threshold photodetachment experiment of the type already performed on the $\mathrm{IHI^-}$ anion [128]. In addition to the direct scattering F + H_2 hindered-rotor states that are seen in the lower resolution spectra, the high resolution spectra show a further distinct set of narrow peaks due

to reactive scattering resonances, and these new peaks have been assigned using an appropriate method of analysis. This is of interest because these resonances have not been seen previously in any other F + H_2 reactive scattering experiment. The results of the calculations presented in this chapter suggest that a future theshold photodetachment experiment on the FH_2^- anion may resolve the resonances clearly and unambiguously.

With regard to future theoretical work in this area, a very important step would be to attempt a calculation in which the propagation of the wavepacket was not confined to a single Born-Oppenheimer potential energy surface. The presence of a conical intersection between the two lowest spin-orbit states in the region between the barrier and the van der Waals well in the reactant valley [147] means that multi-surface effects may play a significant rôle in the FH_2 system, and calculations to investigate this question would be of great interest to dynamicists.

Stop Press!

M.H.Alexander, H.-J.Werner and D.E.Manolopoulos have very recently performed a time-independent multi-surface calculation. The results of this will be published shortly [149].

Chapter 4 Reactive Scattering Calculations on the $N^+ + H_2$ Reaction

In chapter 2 we derived the quantum mechanical theory of reactive scattering, and in particular we obtained an expression for the initial state-selected reaction probability (ISSRP) (given in equations (2.33) and (2.41)). We then went on to discuss the need for approximate methods for calculating ISSRPs for total angular momenta $J > 0$, and gave expressions for the initial state-selected reaction cross section (equation (2.43)), and the initial state-selected reaction rate constant (equation (2.46)).

In the present chapter we apply these ideas to the following reaction [150]:

$$N^+(^3P) + H_2(^1\Sigma_g^+) \longrightarrow NH^+(X^2\Pi) + H(^2S). \tag{4.1}$$

The structure of the chapter is as follows. In section 4.1, we present the motivation behind studying this reaction and give an overview of the previous work, both experimental and theoretical, which has been carried out on this system. Section 4.2 gives a description of the method used for the calculations presented in this chapter, and in section 4.3 we present the results of these calculations and compare them with the results of other work. Finally, in section 4.4, we give a brief summary of the key results presented in this chapter, and also offer some suggestions for future work on the reaction.

4.1 The $N^+ + H_2 \longrightarrow NH^+ + H$ reaction

4.1.1 Introduction

The ion-molecule reaction

$$N^+(^3P) + H_2(^1\Sigma_g^+) \longrightarrow NH^+(X^2\Pi) + H(^2S),$$

has been the subject of a considerable volume of work, both experimental and theoretical. Interest in this reaction can be justified, according to the rationale of Levine and Bernstein [1], both from a pragmatic and from a purist standpoint: not only is the reaction important in the field of astrophysics, but it also has several features which make the dynamics interesting for its own sake. In this section we aim to provide a background to the calculations presented later in the chapter. We shall achieve this by first explaining the importance of the reaction in the field of astrophysics, and then going on to discuss in detail the work which has been carried out on understanding the dynamics of the reaction to date.

4.1.2 Astrophysical significance

Dense interstellar clouds

Regions of space known as "dense interstellar clouds" have been the subject of intense scrutiny in the astrophysics community for over two decades, and their rôle as "stellar nurseries" (*i.e.*, areas in which stars are born) is now beyond question [151]. Such clouds typically possess gas densities n in the range 10^3 cm$^{-3} \leq n \leq 10^6$ cm^{-3} [152], and have temperatures under 40 K†. The chemical complexity of

†Note, however, that recent observations of the molecular hydrogen quadrupole emission spectrum gives evidence for energy-rich regions where vibrationally-excited H_2 may be present [153].

dense interstellar clouds makes it theoretically possible to place constraints on the energetic processes and timescales associated with stellar birth, and thus to gain an improved understanding of the whole process of star formation. This goal would be achieved by using, among other things, the relative abundances of certain species to characterise different regions of space, but of course to do this it is necessary to find molecules which constitute sufficiently distinct "chemical signposts". It is hoped that ammonia could be one such signpost since it has a large number of allowed transitions, but in order for it to be used it is essential to understand the chemistry which governs both its formation and its depletion in interstellar clouds. A detailed understanding of the dynamics of the reactions involved in the formation of ammonia under interstellar conditions, coupled with an understanding of the interplay of this chemistry with large-scale dynamical phenomena in the interstellar region (such as the influence of magnetic fields, the importance of grains and their interaction with the gaseous medium, and the ablation of solid matter by the winds associated with newly formed stars), may lead to the use of ammonia as a sensitive discriminator between different stages of star formation [154, 155].

Interstellar ammonia synthesis

An historic paper by Herbst and Klemperer [156] on gas-phase ion-molecule synthesis was the first to propose a synthetic scheme for the formation of ammonia in dense interstellar clouds:

$$N^+ + H_2 \longrightarrow NH^+ + H, \tag{4.2}$$

$$NH^+ + H_2 \longrightarrow NH_2^+ + H, \tag{4.3}$$

$$NH_2^+ + H_2 \longrightarrow NH_3^+ + H, \tag{4.4}$$

$$NH_3^+ + H_2 \longrightarrow NH_4^+ + H, \tag{4.5}$$

$$NH_4^+ + e^- \longrightarrow NH_3 + H. \tag{4.6}$$

Most of the work concerning the interstellar formation of ammonia has focused on examining this synthetic scheme [151] – [207], and good reviews of this can be found in references [157] and [158]. Here we provide a brief summary of the work in this area.

It is generally accepted that the only reactions which are significant at the low temperatures typical of interstellar conditions are those which are exothermic and which proceed without an activation barrier. Reaction (4.1) is slightly endothermic (by a few tens of meV), and as a result there has been a good deal of discussion as to whether it would be sufficiently fast at the low temperatures of dense interstellar clouds (< 40 K) to account for the observed abundance of ammonia in some regions [158, 159, 160, 161].

One factor which would improve the feasibility of the Herbst-Klemperer scheme for the interstellar synthesis of ammonia is the possibility of a non-thermal translational energy distribution for the reagent $N^+(^3P)$ ions under cloud conditions [159, 162]. It has been argued that the exothermic reaction which is important for the production of $N^+(^3P)$ ions in the interstellar medium [163, 164]

$$He^+ + N_2 \longrightarrow N^+ + N + He, \tag{4.7}$$

produces kinetically excited N^+ ions, and that their translational energy may help to overcome the endothermicity of reaction (4.1), thus increasing the rate of the reaction. The effect of rotational excitation of the reactant H_2 molecules on the rate of reaction (4.1) is also debated in the literature, as is the effect of spin-orbit energy

in the $N^+(^3P)$ ions. These factors will be discussed further later.

The exact value of the endothermicity of reaction (4.1) remains undetermined, due to difficulties both in experimental measurements of the quantity and in theoretical calculations. As a result of this, there is still a great deal of uncertainty concerning the low-temperature rate constant of reaction (4.1), and it is this uncertainty, coupled with some new experimental results [157, 165] which seem to support an alternative synthetic scheme for ammonia, which has led to ongoing discussion about the feasibility of the Herbst-Klemperer mechanism for the production of ammonia.

In 1975, Dalgarno proposed an alternative synthesis for ammonia initiated by the reaction between H_3^+ ions and N atoms [166],

$$H_3^+ + N \longrightarrow NH_2^+ + H, \tag{4.8}$$

which bypasses the first two reactions in the Herbst-Klemperer scheme. Reaction (4.8) was subsequently discredited in the literature as it was thought to possess a large activation barrier and therefore to be impractical in the low-temperature conditions of interstellar clouds [159, 167]. However, some new experimental measurements have re-opened the discussion of Dalgarno's proposal. First, H_3^+ has been observed in the interstellar medium at such densities as could make reaction (4.8) significant [168], and secondly, the rate constant for reaction (4.8) has been measured [165] and suggests that the reaction is fast, although this result remains somewhat controversial in the light of the theoretical work on the system.

The current state of the discussion is summarised in the recent paper by Scott *et al.* [157] in which the authors emphasise the importance of obtaining a clear understanding of the low-temperature behaviour of reaction (4.1). Only when this

has been achieved will it be possible to determine whether the Herbst-Klemperer scheme or the Dalgarno scheme is the more important in the interstellar synthesis of ammonia.

This overview of the astrophysical interest in reaction (4.1) explains the pragmatic justification [1] for interest in the reaction. The next section will describe the work which has been carried out to date towards understanding the chemical dynamics of the reaction, which is interesting both for its own sake and for the bearing it has on the potential astrophysical importance of the reaction.

4.1.3 Chemistry literature

As stated in section 4.1.1, reaction (4.1) is important both for its significance in the field of astrophysics and for certain features of the reaction which make it interesting in its own right. Some of these features are:

- The reaction is nearly thermoneutral (it is endothermic by only a few tens of meV) and its exact thermochemistry has proven difficult to determine.
- Angle-dependent, long-range electrostatic forces are important in the reaction, particularly between the reactants where both ion-induced-dipole and ion-quadrupole forces are present.
- The dynamics of the reaction may be strongly influenced by excited rotational or fine-structure states of the reactants.
- The adiabatic ground-state potential energy surface (PES) for the reaction contains two connected C_{2v} geometry wells – a deep (6.15 eV) inner well and a shallow (2.7 eV) outer well.

In the following sections we shall summarise earlier studies of the dynamics of the reaction, including both experimental and theoretical work.

Experimental work

Experimental work has been carried out both on reaction (4.1) and on its deuterium-substituted analogue:

$$N^+(^3P) + D_2(^1\Sigma_g^+) \longrightarrow ND^+(X^2\Pi) + D(^2S). \tag{4.9}$$

Work has concentrated on the following two areas, although as we shall see below there is still a substantial degree of uncertainty remaining in each of these:

- Accurate determination of the energy thresholds for reactions (4.1) and (4.9),
- Determination of the effect of excitation of the reagents (*i.e.*, excited rotational and spin-orbit states) upon the rate of the reaction.

The early experimental work on reaction (4.1) focused largely on measuring thermal rate constants and on trying to determine the exact thermicity of the reaction [169, 170, 171, 172, 173]. It was, and still is, necessary to do this because the dissociation energy of $NH^+(X^2\Pi)$ has not yet been accurately determined, and the species continues to present a challenge both to experimentalists and to theoreticians [174, 175, 176]. The difficulty in the experimental determination of the exact endothermicity of the reaction is reflected by a large variation in the reported values: between 11 meV and 33 meV in more recent experiments.

In addition to this work on determining the threshold for reaction (4.1), some other early dynamics experiments were carried out. These included the use of the ion-beam method to measure velocity distributions [177, 178, 179, 180, 181]. The distributions obtained indicated that at high relative energies the reaction takes place *via* a direct

mechanism whereas at lower relative energies (< 2 eV) a long-lived complex is involved.

The more recent experimental work on reaction (4.1) has been concerned not only with determining the threshold of the reaction, but also with the second of the two points above; namely, the attempt to understand the effect of reagent excitation on the reaction [158, 182, 183, 184, 185, 186]. The fact that the reaction is so nearly thermoneutral means that the endothermicity is comparable in magnitude both to the spacing of the rotational levels of the H_2 molecule, and to the splitting of the spin-orbit states of the $N^+(^3P)$ ion. An understanding of the effect of excitation of the reactants is therefore crucial in order to predict and understand the low-temperature behaviour of the reaction. There seems to be a general consensus that rotational excitation of the H_2 is effective in promoting the reaction [182, 183, 184, 185], but the effect of spin-orbit excitation in the $N^+(^3P)$ is more ambiguous [158, 182, 183, 186] and still remains to be determined experimentally.

It should be apparent from this overview of the experimental work which has been carried out to date on reaction (4.1) that a good deal still remains to be understood about this reaction. The next section provides a summary of the theoretical work which has been carried out with a view to understanding the dynamics of the system.

Theoretical work

Many ion-molecule reactions are strongly exothermic and have no barrier along their reaction coordinate. Such reactions can often be treated successfully using straightforward capture theories [85] to calculate reaction cross sections and reaction rate constants. The assumption implicit in this simple treatment is that the *capture*

cross section is equal to the *reaction* cross section. In other words, it is assumed that as soon as the reactants have overcome an effective potential barrier (obtained by adding the long-range electrostatic potential between the reactants to the centrifugal potential) they will definitely react to make products [85]. However, in a review of the rates of chemical reactions dominated by long-range intermolecular forces [187], Clary describes the conditions which must be met in order for this to be a good approximation, and in particular stresses the need for the reaction to be strongly exothermic. This condition is not met by reaction (4.1) which is nearly thermoneutral, and thus capture theories cannot be used straightforwardly in this case to calculate reaction cross sections and reaction rate constants.

The theoretical work which has been carried out on reaction (4.1) can be divided into three broad categories:

1. *ab initio* studies,
2. trajectory calculations,
3. statistical calculations.

Of the *ab initio* studies carried out [188, 189, 190, 191, 192, 193], most were concerned with determining the correlation between various surfaces. However, in one case [193] a global potential energy surface (PES) was calculated in order to facilitate studies of the dynamics of the reaction. It was constructed by Wilhelmsson, Siegbahn and Schinke using complete-active-space self-consistent-field and multireference contracted configuration interaction methods to generate 752 points belonging to the ground adiabatic $1^3A''$ surface which were subsequently fitted to an analytic form. This ground-state adiabatic PES is the surface used in the calculations presented in this chapter, and it will be discussed in greater detail later.

The earliest trajectory calculations carried out on the $N^+ + H_2$ reaction were performed by Gittins and Hirst in 1979 [194]. These authors used an analytic Sorbie-Murrell type fit [195] to their own *ab initio* points obtained by unrestricted Hartree-Fock calculations [188, 194] to obtain a surface for the system. The authors concluded that at low initial relative translational energies, symmetric product angular distributions are obtained indicating a complex reaction mechanism, whereas at higher energies, asymmetric distributions are observed which indicate a more direct mechanism.

More recently, two sets of quasi-classical trajectory (QCT) calculations have been carried out on the reaction. The first of these was carried out by Gonzalez *et al.* [196, 197, 198] on a London-Eyring-Polanyi-Sato PES, augmented by an ion-induced-dipole term [199] (thus ignoring the contribution from the ion-quadrupole term). The main conclusion reached by the authors from this work was that the $^3A_2$ minimum at C_{2v} geometry (the more shallow of the two minima in the ground-state adiabatic surface) played a more important rôle in the dynamics of the reaction than was previously expected.

The second set of QCT calculations was that of Wilhelmsson and Nyman [200, 201] who used the surface of Wilhelmsson, Siegbahn and Schinke [193]. In reference [200], the authors demonstrate the importance of explicit consideration of the asymptotic ion-induced-dipole and ion-quadrupole interactions in the entrance channel, and present reaction cross sections as a function of collision energy (approximately in the range 0.06-0.40 eV). Reference [201] contains reaction cross sections and rate constants calculated using the QCT method, and in particular compares the results obtained from two surfaces which are identical in every respect except for a difference

in their thermicities. Some of the results of these calculations will be discussed later on in this chapter, where they will be compared with the results of the new quantum mechanical calculations presented here.

The final calculations to be described in this overview of the theoretical literature for reaction (4.1) are the statistical calculations. There are strong indications both from experiment and from theory that at low collision energies the reaction proceeds *via* a long-lived complex. It was thought that this might make the reaction a good candidate for investigation using a statistical method, although the very low density of reactant states in the threshold region casts some doubt upon the validity of a statistical treatment in the low-energy regime.

Ervin and Armentrout used classical phase space theory (PST) [173] to analyse their experimental reaction cross sections in order to attempt to determine the energy threshold for reaction (4.1). Experimental problems with energy-broadening, however, made it difficult to specify the threshold with precision. Gerlich applied quantum mechanical PST [202] in the form of a "dynamically biased" statistical theory and claimed good agreement between his cross sections and rate constants and those of previous experimental and theoretical investigations. However, this method requires the use of two freely-varying parameters, the reaction endothermicity and an electronic degeneracy factor (to account for the nine different spin-orbit states of the $N^+(^3P)$ ion). Finally, Nyman applied an angular momentum conserving statistical method to reaction (4.1) [203]. Effective potential theory was used to generate a spherically-symmetric potential energy surface from the surface of Wilhelmsson and Nyman [200], and a QCT Monte Carlo simulation procedure was used to determine whether a trajectory on this surface would form a complex. The final step was to

use phase space theory to determine into which channel the complex decomposed. Nyman claimed good agreement with trajectory calculations carried out previously on the same surface [200], although as will be shown later in this chapter, such an agreement does not necessarily inspire confidence in the statistical results.

Aims for the present work

It is clear from this overview of the literature concerning reaction (4.1) that there have been no fully quantum mechanical calculations carried out to date on the dynamics of the reaction. In order to judge which of the trajectory or statistical methods are accurate for a reaction such as this, it is obviously necessary to have the exact quantum mechanical results to compare with. The aim of the calculations presented in this chapter is therefore to calculate quantum mechanical initial state-selected reaction probabilities, cross sections, and rate constants for reaction (4.1) on the *ab initio* surface of Wilhelmsson, Siegbahn and Schinke [193]. By doing this we hope both to come to a better understanding of the dynamics of the reaction, and also to test the validity of the more approximate theoretical methods which have been applied previously to the reaction.

4.2 Method and computational details

4.2.1 Introduction

In this section we describe the computational wavepacket method used in the calculations carried out on reaction (4.1). Before getting into a detailed discussion of various aspects of the wavepacket method, however, we shall begin with a review of the equations derived in chapter 2, and with a simple pictorial introduction in order

to give an overall idea of what is involved in calculations of this type.

In chapter 2 we derived the following formula for the initial state-selected reaction probability (ISSRP):

$$P^{\beta}_{\alpha \mathbf{i}}(E) = \langle \psi^{+}_{E,\alpha \mathbf{i}} | \hat{F}^{\beta} | \psi^{+}_{E,\alpha \mathbf{i}} \rangle. \tag{4.10}$$

Here, $\hat{F}^{\beta}$ is an operator which calculates the wavepacket flux into arrangement channel β, α and β denote the reactant and product arrangement channels respectively, $\mathbf{i}$ represents the quantum numbers of the initial state of the reactants, and $P^{\beta}_{\alpha \mathbf{i}}(E)$ is the probability at energy E for reaction to take place from the initial state $\alpha \mathbf{i}$ into the final arrangement channel β. Finally, the energy-dependent wavefunction, $|\psi^{+}_{E,\alpha \mathbf{i}}\rangle$, is given by

$$|\psi^{+}_{E,\alpha \mathbf{i}}\rangle = \frac{1}{\langle \phi^{-}_{E,\alpha \mathbf{i}} | \phi_{\alpha \mathbf{i}} \rangle} \int_0^{+\infty} e^{+iEt/\hbar} |\psi_{\alpha \mathbf{i}}(t)\rangle dt, \tag{4.11}$$

where $\phi^{-}_{E,\alpha \mathbf{i}}$ is defined in equations (2.18) and (2.19) of chapter 2, $|\phi_{\alpha \mathbf{i}}\rangle$ is a state-selected initial wavepacket in arrangement channel α, and the wavepacket at time t is given by

$$|\psi_{\alpha \mathbf{i}}(t)\rangle = e^{-iHt/\hbar} |\phi_{\alpha \mathbf{i}}\rangle. \tag{4.12}$$

It should be clear from these equations that a wavepacket calculation of the ISSRP will involve three main stages. These are illustrated (for a collinear three-atom reaction) in figure 4.1, and can be summarised as follows:

1. Set-up of the representation of the Hamiltonian, H, and the initial wavepacket, $|\phi_{\alpha \mathbf{i}}\rangle$,
2. Propagation of the wavepacket to obtain $|\psi_{\alpha \mathbf{i}}(t)\rangle$ (equation (4.12)),
3. Analysis of $|\psi_{\alpha \mathbf{i}}(t)\rangle$ using a flux dividing surface to give the ISSRP (equations (4.10) and (4.11)).

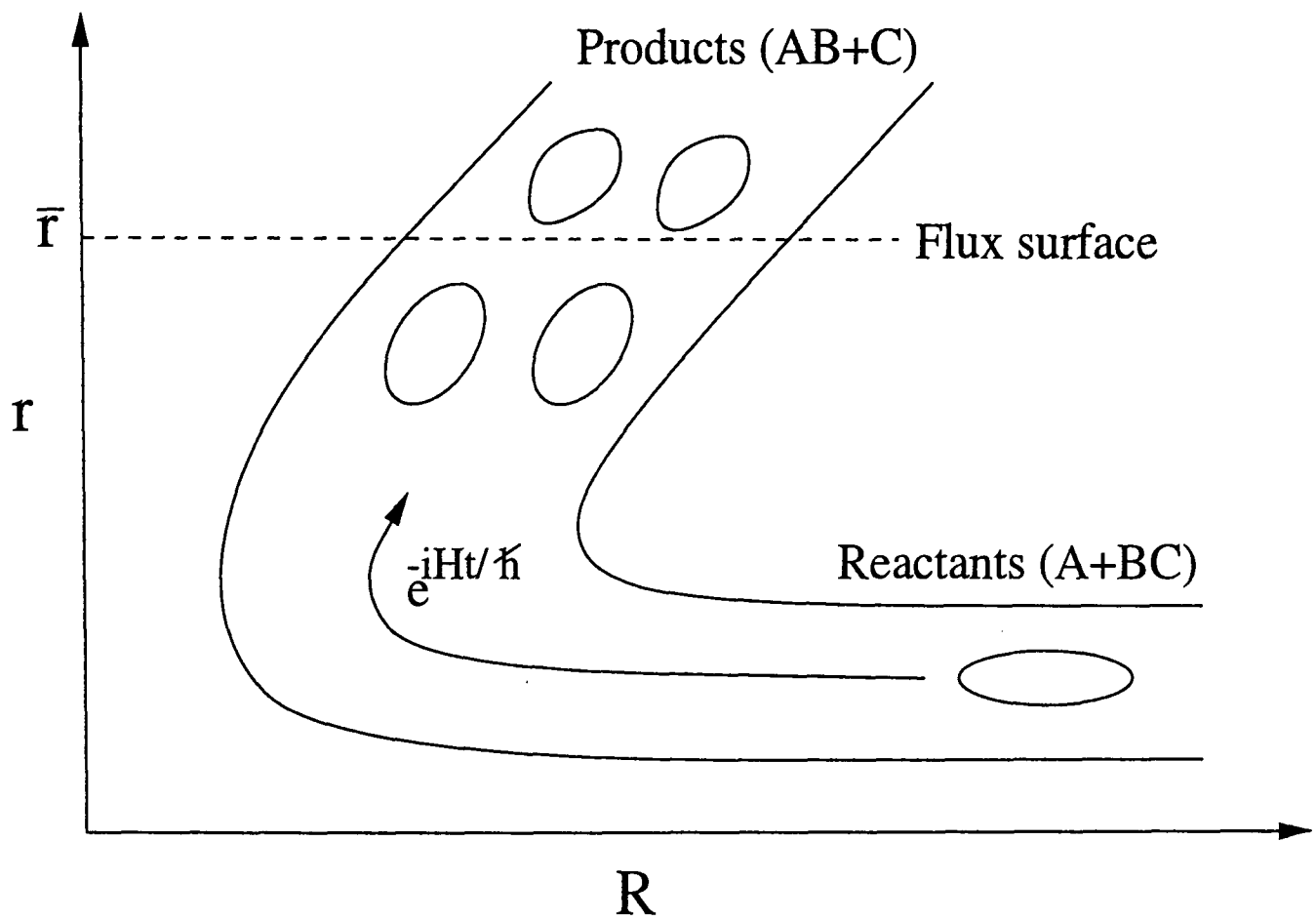


Figure 4.1 A schematic diagram to illustrate a wavepacket calculation of the initial state-selected reaction probability for a collinear reaction A + BC ⟶ AB + C. The coordinates R and r are the mass-scaled Jacobi coordinates for the A + BC arrangement channel.

In the next section we shall go on to discuss the methodology of the $N^+ + H_2$ calculations in more detail.

4.2.2 Methodology

Introduction

In this section we begin by describing the method which we used to implement equations (4.10), (4.11), and (4.12) for the calculation of initial state-selected reaction probabilities (ISSRPs) for total angular momentum $J = 0$. We first give the coordinates used in the calculations and the form of the Hamiltonian in these coordinates. Next we discuss the potential energy surface that we used, and the way in which the features of this surface influenced the choice of representation for the

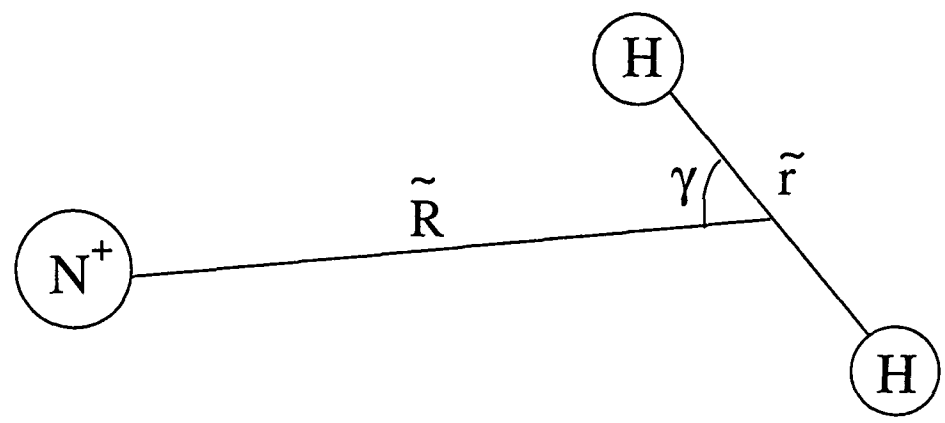


Figure 4.2 Jacobi coordinates of the $N^+ + H_2$ reactant arrangement.

Hamiltonian. After describing the representation of the Hamiltonian we continue by discussing the absorbing potential, the form of the initial wavefunction $|\phi_{\alpha i}\rangle$, the propagation method, and the way in which the flux was calculated. In the final part of the section we explain the calculation of initial state-selected cross sections and rate constants, in particular concentrating on the implementation of the rotationally adiabatic approximation for total angular momenta $J > 0$.

Coordinates and Hamiltonian for $J = 0$

The calculations were carried out using the same coordinates as we used for the FH_2^- calculations described in chapter 3: the mass-scaled Jacobi (MSJ) coordinates of the reactant arrangement (see section 3.3.2). These coordinates, (R, r, γ), are discussed in detail in appendix B, and their corresponding unscaled coordinates are illustrated in figure 4.2.

Expressed in MSJ coordinates, the form of the Hamiltonian for total angular momentum $J = 0$ (within the Born-Oppenheimer approximation) is the same as that in equations (3.9), (3.10), and (3.11):

$$H = T + U, \tag{4.13}$$

where

$$T = -\frac{\hbar^2}{2\mu}\left(\frac{\partial^2}{\partial R^2} + \frac{\partial^2}{\partial r^2}\right), \tag{4.14}$$

and

$$U = +\frac{1}{2\mu}\left(\frac{1}{R^2} + \frac{1}{r^2}\right)\hat{j}^2 + V(R, r, \gamma). \tag{4.15}$$

Here, $\hat{j}$ is the rotational angular momentum operator associated with rotation of the vector $\boldsymbol{r}$, the reduced mass μ is given by

$$\mu = \left(\frac{m_N m_H m_H}{m_N + m_H + m_H}\right)^{\frac{1}{2}}, \tag{4.16}$$

and $V(R, r, \gamma)$ is the potential energy as a function of the nuclear coordinates.

Potential energy surface

We used the *ab initio* ground-state adiabatic potential energy surface† of Wilhelms-son, Siegbahn and Schinke (WSS) [193], which approximates the $1^3A''$ surface for the $N^+(^3P) + H_2(^1\Sigma_g^+)$ reaction. A simplified correlation diagram for the system is shown in figure 4.3. The existence of an avoided intersection in C_s symmetry means that both the $^3B_1$ and $^3A_2$ (in C_{2v} geometry) wells are present and accessible on the ground-state adiabatic PES. These two wells (which occur at different geometries) were mentioned previously in section 4.1.3 and, as will be seen later, have an extremely important effect on the dynamics of the reaction. For future reference, the $^3A_2$ well will be referred to as the "shallow" or "outer" well, while the $^3B_1$ well will be referred to as the "deep" or "inner" well. The WSS PES also contains a $^3\Sigma_g^-$ well in $D_{\infty h}$ geometry which is evident in the correlation diagram in figure 4.3.

Figure 4.3 shows that there is an excited state of NH^+ ($a^4\Sigma^-$) lying fairly close in energy to the ground $^2\Pi$ state (the separation is approximately 60 meV), which is

†This is the PES denoted PES(IV) in reference [201].

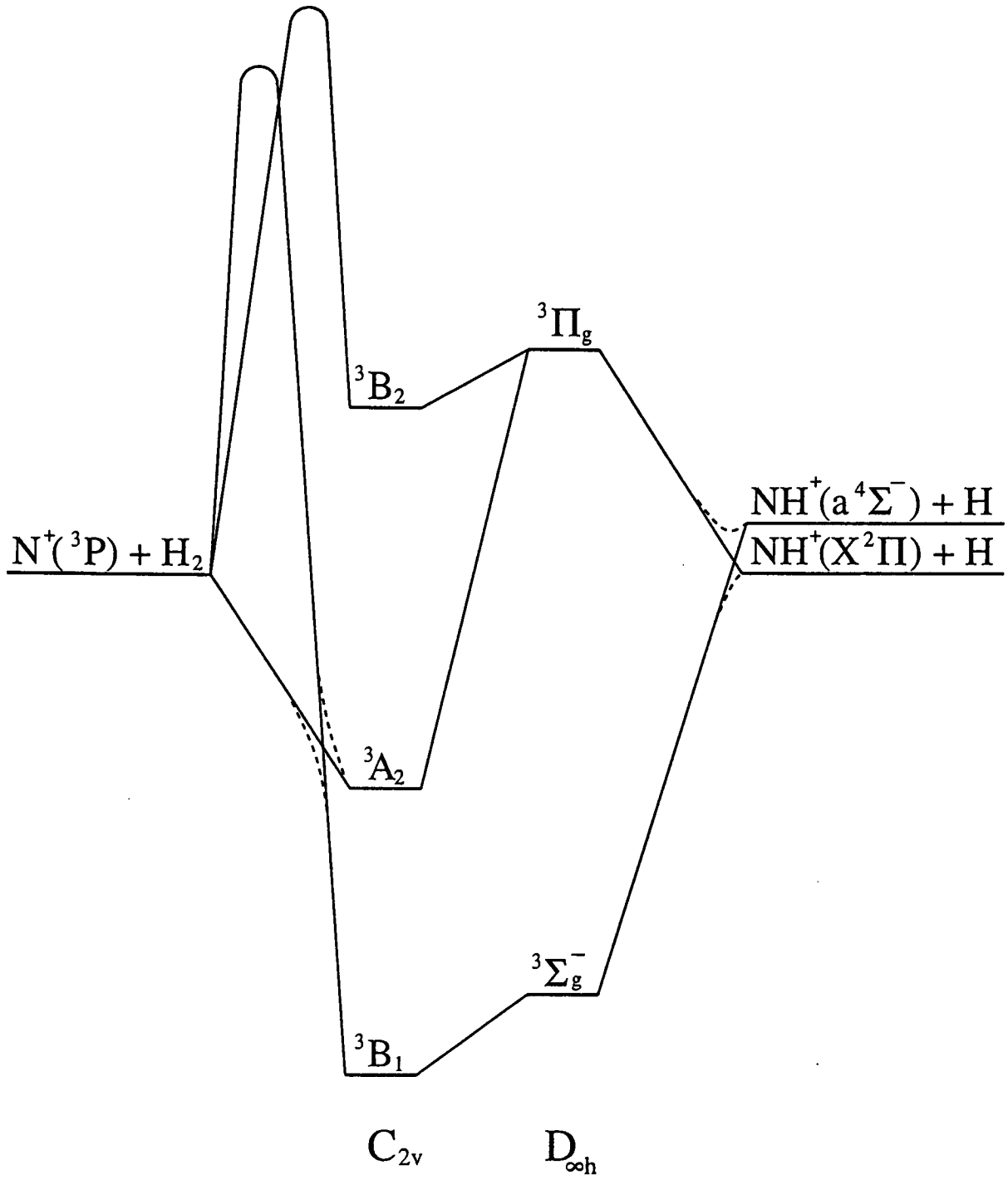


Figure 4.3 A simplified electronic correlation diagram for the reaction $N^+(^3P) + H_2(^1\Sigma_g^+) \longrightarrow NH^+(X^2\Pi) + H(^2S)$ (adapted from [197]). Dashed lines indicate the existence of avoided intersections when the system is relaxed to C_s symmetry.

not included in the ground-state adiabatic WSS PES (the natural limitation of a single-surface calculation). While it is the case that at the very low temperatures of interest in dense interstellar clouds this product state will not be accessible, clearly for higher temperatures only a full multi-surface calculation could account correctly for the effect of this excited state on the reaction of $N^+ + H_2$.

The key features of the WSS surface are:

- Quantum mechanical endothermicity of 0.033 eV,

- Shallow (2.7 eV) $^3A_2$ well at $\tilde{R}$=2.29 bohr, $\tilde{r}$=1.70 bohr, γ=90°,
- Deep (6.15 eV) $^3B_1$ well at $\tilde{R}$=0.62 bohr, $\tilde{r}$=3.67 bohr, γ=90°,
- Collinear (2.05 eV) $^3\Sigma_g^-$ well at $\tilde{R}$=3.12 bohr, $\tilde{r}$=1.70 bohr, γ=0°.

The fact that the WSS PES contains a well which is over 6 eV deep means that it presents a considerable challenge from a computational point of view since it is necessary to have a very small discrete variable representation (DVR) grid-spacing, and therefore a large number of grid points, in the well region.

Representation of the Hamiltonian

The choice of the representation of the Hamiltonian is crucial in determining whether quantum mechanical calculations are feasible for the $N^+ + H_2$ reaction. For the angular coordinate, γ, we used a standard Legendre polynomial basis set, but in order to overcome the computational difficulties caused by the deep well in the PES we needed to optimise the representation used for the radial coordinates R and r. The potential-optimised DVR (PO-DVR) of Echave and Clary [208] was the obvious choice, since it places grid points *where they are needed* on the PES. In other words, for a reaction such as $N^+ + H_2$, the PO-DVR gives a high density of grid points in the region of the wells where the potential is very negative, but it gives a lower density of grid points in the asymptotic reactant and product valleys.

To set up the radial grid PO-DVR we used the following basic steps:

1. Set up a primitive DVR [131] in each of R and r.
2. For each radial coordinate, construct a 1-dimensional reference Hamiltonian matrix using the primitive DVR. For example, for the R coordinate the refer-

ence Hamiltonian is given by

$$H^{\text{ref}}(R) = -\frac{\hbar^2}{2\mu}\frac{\partial^2}{\partial R^2} + V^{\text{ref}}(R), \tag{4.17}$$

where

$$V^{\text{ref}}(R) = \min_{r,\gamma}[V(R,r,\gamma)]. \tag{4.18}$$

3. Diagonalise the reference Hamiltonian matrix, and select only the eigenstates which have eigenvalues less than a cut-off energy, E_{cut}, where the cut-off energy is a convergence parameter in the calculation.

4. Construct and diagonalise the coordinate matrix (R in this case) in the basis of the eigenstates selected above. The eigenvalues from this diagonalisation are the positions of the PO-DVR grid points in R.

5. Finally, use a potential cut-off parameter, V_{max} (another convergence parameter), to keep only the radial grid points which satisfy the criterion:

$$\min_{\gamma}[V(R,r,\gamma)] < V_{\text{max}}. \tag{4.19}$$

The radial grid points that we obtained using this method (converged parameters are given in section 4.2.3) are illustrated in figure 4.4, superimposed onto $V_{\text{min}}(R,r)$, where $V_{\text{min}}(R,r)$ is defined as

$$V_{\text{min}}(R,r) = \min_{\gamma}[V(R,r,\gamma)]. \tag{4.20}$$

It can be seen from figure 4.4 that the PO-DVR works particularly nicely for this system because the deep well in the PES occurs at both a significantly smaller value of R and a significantly larger value of r than is present in the energetically accessible region of the reactant valley. This means that the density of radial grid points is comparatively low in the reactant valley, and thus it is fairly cheap to extend the grid

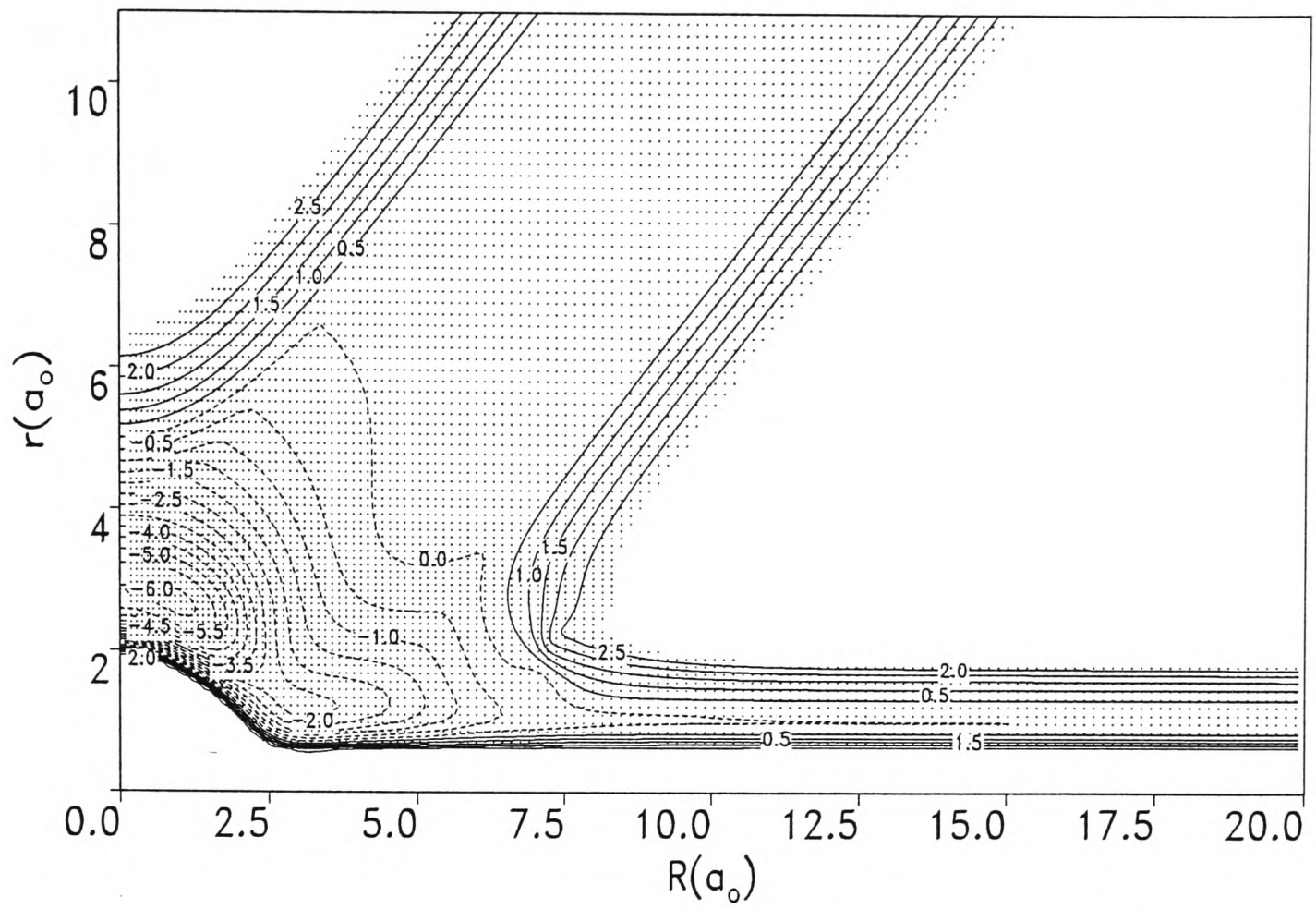


Figure 4.4 Radial grid for the Wilhelmsson, Siegbahn and Schinke PES [193] generated using the potential-optimised discrete variable representation of Echave and Clary [208], superimposed onto $V_{\min}(R, r)$ (defined in the text). Potential contours are in eV, with a solid line denoting a positive energy and a dashed line denoting a negative energy relative to the bottom of the asymptotic reactant valley.

to a large value of R. It is necessary to do this in order to obtain converged results for this reaction since there are long-range, anisotropic, electrostatic interactions in the reactant valley.

Note that it requires only a simple matrix multiplication in order to transform any vector from the primitive DVR onto the PO-DVR. It may be necessary to do this during the set-up of the calculation, for example for the initial wavepacket or for the "flux vectors" which will be discussed below.

Absorbing potential

The next aspect of the method to be discussed is the absorbing potential. As we

described in section 3.3.2, it is necessary during a wavepacket propagation to prevent unphysical reflections of the wavepacket off the edges of the radial grid. To do this in the present calculations we used a numerically-optimised absorbing potential over the last 25% of the grids in R and r; this is discussed in greater detail in appendix A.

Initial wavepacket

The aim of the work described in this chapter was to calculate initial state-selected reaction probabilities (ISSRPs) for various different initial states of the reactants of reaction (4.1), and from these to calculate initial state-selected cross sections and rate constants. Clearly, the initial wavepacket is therefore state-selected in order to represent the initial state of interest. The form of the initial wavepacket which we used was

$$|\phi_{\alpha \mathrm{i}}\rangle = (\pi\delta^2)^{-\frac{1}{4}} e^{[-(R-R_0)^2/2\delta^2]} e^{-ik_0 R} \Theta_{vj}(r,\gamma). \tag{4.21}$$

This wavepacket is the product of a Gaussian in R and a function, $\Theta_{vj}(r,\gamma)$, which describes a particular ro-vibrational state of the reactant H_2 molecule, where v and j are respectively the vibrational and rotational quantum numbers of the diatomic.

The function $\Theta_{vj}(r,\gamma)$ in equation (4.21) is given by the product

$$\Theta_{vj}(r,\gamma) = \theta_{vj}(r)\hat{\mathrm{P}}_j(\cos\gamma), \tag{4.22}$$

where

$$\hat{\mathrm{P}}_j(\cos\gamma) = \sqrt{\left(j+\frac{1}{2}\right)}\mathrm{P}_j(\cos\gamma), \tag{4.23}$$

and $\mathrm{P}_j(\cos\gamma)$ is a Legendre polynomial in $\cos\gamma$. Finally, the function $\theta_{vj}(r)$ is evaluated by diagonalising the appropriate Hamiltonian matrix for internal motion of the H_2 molecule (constructed using a primitive DVR):

$$H^{\mathrm{int}}\theta_{vj}(r) = \epsilon_{vj}\theta_{vj}(r), \tag{4.24}$$

subject to

$$\int_0^\infty \theta_{v'j}(r)\theta_{vj}(r)dr = \delta_{v'v}. \tag{4.25}$$

In the above expression, the Hamiltonian is given by

$$H^{\text{int}} = -\frac{\hbar^2}{2\mu}\frac{d^2}{dr^2} + \frac{\hbar^2 j(j+1)}{2\mu r^2} + V^{\text{int}}(r), \tag{4.26}$$

where $V^{\text{int}}(r)$ is the internal potential function of the H_2 bond.

In addition to specifying the initial state (v, j) of the reactants, three parameters must be chosen in the design of the initial wavepacket: R_0, the centre of the Gaussian in R; δ, the width of the Gaussian; and k_0, the average wave-vector in the R direction. In choosing these parameters the following considerations must be taken into account:

- R_0 must be large enough such that the wavepacket starts off in the truly asymptotic region of the reactant valley (*i.e.*, far enough from the close interaction region that there are no significant interactions between the reactants). R_0 is generally regarded as a convergence parameter in the calculation.
- Care must be taken to ensure that the wavepacket does not start off in the absorbing region of the reactant valley, otherwise the wavepacket will be absorbed before it has a chance to reach the interaction region.
- k_0 and δ must be chosen such that the wavepacket contains a significant component at each energy, E, in the energy range of interest, *i.e.*, the range of energies over which the ISSRP is to be determined. In general, δ will be small so that the wavepacket contains a wide range of energies.
- The ISSRPs which constitute the results of these calculations must be independent of the choice of the parameters for the initial wavepacket.

From equation (4.11) it is clear that in order to calculate the ISSRP we need to

evaluate the coefficient

$$a_{\alpha \mathbf{i}}(E) = \langle \phi^-_{E,\alpha \mathbf{i}} | \phi_{\alpha \mathbf{i}} \rangle, \tag{4.27}$$

in which $\phi^-_{E,\alpha \mathbf{i}}$ is a purely-incoming, energy-dependent wavefunction as given in equations (2.18) and (2.19). The orthonormality of the internal eigenstates of the H_2 molecule means that the integral in equation (4.27) simply becomes a 1-dimensional integral over R, which can be evaluated numerically using a quadrature method.

Propagation method

The propagation of the wavepacket implied in equation (4.12) was achieved in exactly the same way as in the calculations in chapter 3. We used the symmetric split operator method [132, 42] with a partitioning of the Hamiltonian into radial kinetic energy (T) and potential and rotational energy (U) operators as indicated in equations (4.13), (4.14), and (4.15):

$$\begin{aligned} \psi_i(t + \Delta t) &= e^{-iH\Delta t/\hbar} \psi_i(t) \\ &= e^{-iU\Delta t/2\hbar} e^{-iT\Delta t/\hbar} e^{-iU\Delta t/2\hbar} \psi_i(t) + O(\Delta t^3). \end{aligned} \tag{4.28}$$

Flux calculation

The next topic to be discussed is the method used to evaluate the wavepacket flux, *i.e.*, the method used to evaluate the expressions in equations (4.10), (4.11) and (4.12). It is possible to save a great deal of computational storage space by manipulating these equations slightly. To do this we begin by recalling the definition of the flux operator $\hat{F}^\beta$ from equation (2.37) (for clarity we drop the β superscript from this point). In the present calculations, however, we used r, the mass-scaled Jacobi coordinate of the reactant arrangement, to define the flux surface, instead of using R_β as in equation (2.37). The reason for doing this is that it makes no

difference to the results of the calculation but it makes the implementation simpler. Thus,

$$\hat{F} = -\frac{i\hbar}{2\mu}\left[\frac{\partial}{\partial r}\delta(r-\overline{r}) + \delta(r-\overline{r})\frac{\partial}{\partial r}\right], \tag{4.29}$$

where $\overline{r}$ is the value of r at which the flux surface is located (see figure 4.1). Clearly, the flux surface must be placed far enough out in the asymptotic region of the product valley such that no "re-crossing" takes place through it, and therefore the value of $\overline{r}$ is a convergence parameter in the calculation.

Now, consider a matrix representation of $\hat{F}$ in a basis of particle-in-a-box functions:

$$\phi_n(r) = \sqrt{\frac{2}{r_{\max}}}\sin\left(\frac{n\pi r}{r_{\max}}\right), \qquad n = 1, 2 \ldots N, \tag{4.30}$$

where $r_{\max}$ is the maximum value of r on the DVR grid, and N is the number of basis functions for the r dimension. In this basis, a matrix element of the flux operator is given by

$$\begin{aligned} F_{mn}^{\mathrm{FBR}} &= \langle\phi_m|\hat{F}|\phi_n\rangle, \\ &= -\frac{i\hbar}{2\mu}\langle\phi_m|\frac{\partial}{\partial r}\delta(r-\overline{r}) + \delta(r-\overline{r})\frac{\partial}{\partial r}|\phi_n\rangle, \\ &= -\frac{i\hbar}{2\mu}\int_0^{r_{\max}}\phi_m(r)\left[\frac{\partial}{\partial r}\delta(r-\overline{r}) + \delta(r-\overline{r})\frac{\partial}{\partial r}\right]\phi_n(r)dr, \end{aligned} \tag{4.31}$$

and evaluating this integral by parts gives

$$F_{mn}^{\mathrm{FBR}} = \frac{i\hbar}{2\mu}\left[\phi_m'(\overline{r})\phi_n(\overline{r}) - \phi_m(\overline{r})\phi_n'(\overline{r})\right], \tag{4.32}$$

where

$$\phi_n'(\overline{r}) = \left.\frac{\partial}{\partial r}\phi_n(r)\right|_{r=\overline{r}.} \tag{4.33}$$

We now define two real vectors, $\boldsymbol{U}$ and $\boldsymbol{V}$, with elements

$$U_n = \phi_n(\overline{r}), \tag{4.34}$$

$$V_n = \frac{\hbar}{\mu}\phi_n'(\overline{r}). \tag{4.35}$$

The matrix of the flux operator can be expressed in terms of these vectors as

$$\boldsymbol{F}^{\mathrm{FBR}} = \frac{i}{2}\left[\boldsymbol{V}\cdot\boldsymbol{U}^{\mathrm{T}} - \boldsymbol{U}\cdot\boldsymbol{V}^{\mathrm{T}}\right]. \tag{4.36}$$

From equation (4.36) it is clear that $\boldsymbol{F}^{\mathrm{FBR}}$ is a matrix of rank 2. In other words, we need know only the two vectors, $\boldsymbol{U}$ and $\boldsymbol{V}$, in order to know $\boldsymbol{F}^{\mathrm{FBR}}$.

The next step is to recognise that we can transform the representation of the $\hat{F}$ operator from an FBR to a DVR using a simple orthogonal transformation. Thus

$$\boldsymbol{F}^{\mathrm{DVR}} = \boldsymbol{C}\ \boldsymbol{F}^{\mathrm{FBR}}\boldsymbol{C}^{\mathrm{T}}, \tag{4.37}$$

where $\boldsymbol{C}$ is the appropriate transformation matrix† with elements

$$C_{kn} = w_k^{\frac{1}{2}}\phi_n(r_k), \tag{4.38}$$

in which w_k is the appropriate DVR weight for the kth grid point. Clearly,

$$\begin{aligned}\boldsymbol{F}^{\mathrm{DVR}} &= \frac{i}{2}\left[\boldsymbol{C}\ \boldsymbol{V}\cdot\boldsymbol{U}^{\mathrm{T}}\boldsymbol{C}^{\mathrm{T}} - \boldsymbol{C}\ \boldsymbol{U}\cdot\boldsymbol{V}^{\mathrm{T}}\boldsymbol{C}^{\mathrm{T}}\right],\\ &= \frac{i}{2}\left[\boldsymbol{v}\cdot\boldsymbol{u}^{\mathrm{T}} - \boldsymbol{u}\cdot\boldsymbol{v}^{\mathrm{T}}\right],\end{aligned} \tag{4.39}$$

where $\boldsymbol{u}$ and $\boldsymbol{v}$ are the two vectors in the DVR and are given by

$$\boldsymbol{u} = \boldsymbol{C}\ \boldsymbol{U}, \tag{4.40}$$

$$\boldsymbol{v} = \boldsymbol{C}\ \boldsymbol{V}. \tag{4.41}$$

We now turn to consider the expression for the ISSRP given in equations (4.10) and (4.11). The full three-dimensional form of the flux operator in mass-scaled Jacobi coordinates is

$${}^{3\mathrm{D}}\boldsymbol{F}^{\mathrm{DVR}} = \boldsymbol{F}^{\mathrm{DVR}} \otimes \boldsymbol{I}^{R} \otimes \boldsymbol{I}^{\gamma}, \tag{4.42}$$

†Note that C has the property $C^{\mathrm{T}}C = I$, where I is the unit matrix.

where $\boldsymbol{I}^R$ and $\boldsymbol{I}^\gamma$ are unit matrices in the R and γ dimensions respectively. Therefore, if we define the two time-dependent vectors $\boldsymbol{\Upsilon}_{R\gamma}(t)$ and $\boldsymbol{\Sigma}_{R\gamma}(t)$ by

$$\boldsymbol{\Upsilon}_{R\gamma}(t) = \boldsymbol{u}^{\mathrm{T}}|\psi_{\alpha\mathbf{i}}(t)\rangle, \tag{4.43}$$

$$\boldsymbol{\Sigma}_{R\gamma}(t) = \boldsymbol{v}^{\mathrm{T}}|\psi_{\alpha\mathbf{i}}(t)\rangle, \tag{4.44}$$

and then substitute equations (4.39) and (4.42) into equations (4.10) and (4.11), we obtain

$$P_{\alpha\mathbf{i}}(E) = \frac{1}{|a_{\alpha\mathbf{i}}(E)|^2}\mathrm{Im}\left(\boldsymbol{\Upsilon}_{R\gamma}(E)^\dagger \cdot \boldsymbol{\Sigma}_{R\gamma}(E)\right), \tag{4.45}$$

where

$$\boldsymbol{\Upsilon}_{R\gamma}(E) = \int_0^\infty e^{+iEt/\hbar}\boldsymbol{\Upsilon}_{R\gamma}(t)dt, \tag{4.46}$$

and

$$\boldsymbol{\Sigma}_{R\gamma}(E) = \int_0^\infty e^{+iEt/\hbar}\boldsymbol{\Sigma}_{R\gamma}(t)dt. \tag{4.47}$$

Equation (4.45) constitutes the expression for the ISSRP which is implemented in these calculations. It can be seen that it is only necessary to store the two two-dimensional vectors, $\boldsymbol{\Upsilon}_{R\gamma}(E)$ and $\boldsymbol{\Sigma}_{R\gamma}(E)$, in order to calculate the ISSRP. Using this fact prevents the computational storage problems which would arise if it were necessary to store the entire three-dimensional energy-dependent wavefunction $|\psi^+_{E,\alpha\mathbf{i}}\rangle$ at every energy.

Calculations for total angular momentum $J > 0$

Thus far we have described the methodology which is appropriate for wavepacket calculations for total angular momentum $J = 0$. This methodology is used in the calculation of the initial state-selected reaction probabilities (ISSRPs) for $J = 0$ which are presented in section 4.3.1. We shall now go on in this section to describe the implementation of the rotationally adiabatic approximation (RAA) which was

described in section 2.3.7. This is the approximation which we used to calculate ISSRPs for total angular momentum $J > 0$, which were needed in order to calculate the initial state-selected cross sections and rate constants presented in sections 4.3.2 and 4.3.3 respectively.

The reason we used the RAA for this reaction, rather than the well-known centrifugal sudden approximation (CSA), was hinted at in section 2.3.5. In that section we explained that the CSA would be a poor approximation for a reaction whose dynamics was dominated by a deep well, the geometry of which was such that the principal axis associated with the smallest moment of inertia (the $\boldsymbol{a}$ axis) was perpendicular to the $\boldsymbol{R}$ vector (such a geometry is illustrated in figure 2.7). Recall from the discussion of the potential energy surface on page 102, that the PES for reaction (4.1) contains a deep $^3B_1$ well. Figure 4.5 illustrates the geometry of this well, and shows that it falls into the category described above. As a result of this, we decided that the CSA would not be a good approximation for reaction (4.1), and that the RAA would be more appropriate.

The version of the RAA we have implemented is appropriate for the calculation of degeneracy-averaged ISSRPs of the form

$$P^J_{vj}(E) = \frac{1}{(2j+1)} \sum_K P^J_{vjK}(E), \tag{4.48}$$

where K is the initial helicity quantum number of the reactant diatomic. In order to calculate these reaction probabilities we have neglected the dependence of $P^J_{vjK}(E)$ on K and simply assumed that equation (4.48) can be approximated by $P^J_{vj}(E) \approx P^J_{vj0}(E)$. While this is not an additional approximation for a $j = 0$ initial state for which the only available helicity quantum number is $K = 0$, it clearly is an additional approximation for an initial state with $j = 1$, for example, and our

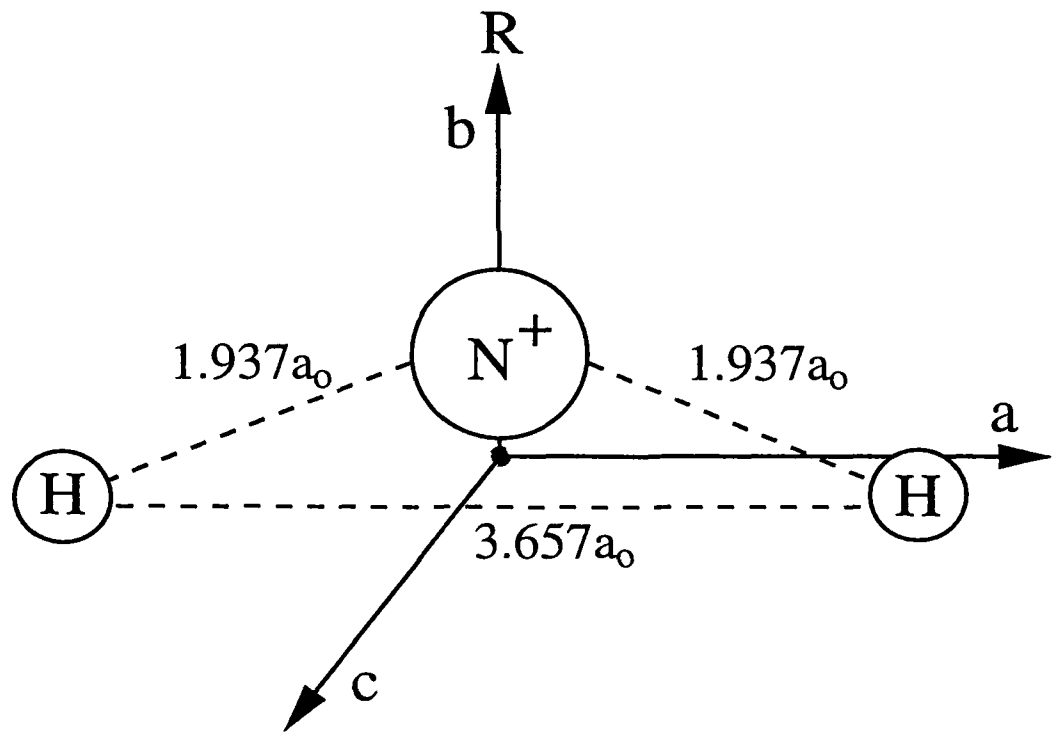


Figure 4.5 Geometry of the deep well in the ground-state adiabatic PES of Wilhelmsson, Siegbahn and Schinke [193] for reaction (4.1). The principal axes of inertia (a, b and c), and the mass-scaled Jacobi $\boldsymbol{R}$ vector are shown.

results in section 4.3 should therefore by viewed with this in mind[†].

Besides reducing the number of calculations that are required to calculate $P^J_{vj}(E)$, another advantage of focusing on the $K = 0$ initial state is that it makes the implementation of the RAA particularly easy. The calculation of $P^J_{vj}(E)$ within this approximation is essentially the same as a $J = 0$ calculation but with a couple of minor modifications. Instead of using the $J = 0$ Hamiltonian given in equations (4.13), (4.14) and (4.15) we use the full Hamiltonian. However, the use of the RAA simplifies the form of the three-dimensional Hamiltonian from that given in equation (2.49) to the following:

$$H^{\mathrm{RAA}} = T + U^{\mathrm{RAA}}, \tag{4.49}$$

[†]We could in principle have not made this additional approximation and implemented equation (4.48) directly within the RAA, but this would have required three separate calculations for the $j = 1$ initial state instead of just one. Given the expense of the calculations and the large number of J values involved we did not feel that this was justified.

where

$$T = -\frac{\hbar^2}{2\mu}\left(\frac{\partial^2}{\partial R^2} + \frac{\partial^2}{\partial r^2}\right), \tag{4.50}$$

and

$$U^{\mathrm{RAA}} = +\frac{1}{2\mu}\left(\frac{1}{R^2} + \frac{1}{r^2}\right)\hat{j}^2 + \mathcal{U}^{\mathrm{RAA}}_{JK_aK_c}(R,r,\gamma) + V(R,r,\gamma). \tag{4.51}$$

In equation (4.51), J is the total angular momentum quantum number, K_a and K_c are quantum numbers associated with the projection of the total angular momentum onto the body-fixed z' axis in the limit of a prolate top and an oblate top respectively, and $V(R,r,\gamma)$ is the potential energy surface as before. The effective rotational energy surface, $\mathcal{U}^{\mathrm{RAA}}_{JK_aK_c}(R,r,\gamma)$, is obtained using the RAA, and in our degeneracy-averaging approximation it corresponds to the lowest eigenvalue for total angular momentum J of the asymmetric top Hamiltonian at the instantaneous geometry (R,r,γ) of the three atoms (see appendix C):

$$\mathcal{U}^{\mathrm{RAA}}_{JK_aK_c}(R,r,\gamma) = E^J_{0J}(R,r,\gamma). \tag{4.52}$$

Within this approximation we can summarise the steps involved in a $J > 0$ calculation in the following way. During the set-up of the calculation of the ISSRP for the total angular momentum quantum number, J, we simply calculate the appropriate effective rotational energy surface, $E^J_{0J}(R,r,\gamma)$, and add it to the potential, $V(R,r,\gamma)$, to form a new surface. Once this has been done, we use this new surface instead of $V(R,r,\gamma)$ in the set-up of the PO-DVR. The calculation of the degeneracy-averaged ISSRP for angular momentum J then proceeds in the same way as that for $J = 0$, except that of course the form of the Hamiltonian used in the split operator propagator is that given in equations (4.50) and (4.51), rather than the $J = 0$ form.

To calculate the initial state-selected cross section over a particular energy range it

is necessary to carry out an ISSRP calculation for every contributing value of J up to a maximum value of the total angular momentum quantum number, J^{max}. This parameter is chosen such that for all values of J greater than J^{max}, the ISSRP is zero throughout the energy range of interest.†

Summary

In this section we have described the methodology used in these calculations on reaction (4.1). We first discussed various aspects of the wavepacket method for $J = 0$ calculations, and then finished by explaining the implementation of the rotationally adiabatic approximation for $J > 0$. In the next section we give some numerical details for the calculations.

4.2.3 Numerical details

Initial state-selected reaction probabilities (ISSRPs) were calculated for the following initial states of the reactants, $N^+ + H_2$ (v, j), in order to determine the effect on the dynamics of the reaction of rotational and vibrational excitation of the reactant H_2:

- $(v = 0, j = 0)$,
- $(v = 0, j = 1)$,
- $(v = 1, j = 0)$,
- $(v = 1, j = 1)$.

For each initial state, the ISSRP was determined at 500 energies over the same translational energy range, 0 eV to 0.52 eV. We ensured that the number of energies was sufficient to resolve the structure in the plots of ISSRP *versus* energy.

†As the total angular momentum increases, the centrifugal barrier to reaction increases [1], and thus the effective energy threshold for reaction also increases.

R_{max}/a_0	r_{max}/a_0	$\overline{r}/a_0$	E_{cut}/eV	$\Delta t/fs$	R_0/a_0	δ/a_0	k_0/a_0^{-1}
20	11	8.25	3.0	0.066	14.6	0.19	8.2

Table 4.1 Convergence parameters for ISSRP calculations.

No. of primitive DVR grid points		No. of PO-DVR grid points	
R	r	R	r
216	118	141	77

Table 4.2 An illustration of the advantage of using the potential optimised DVR instead of a primitive DVR: the number of primitive DVR grid points *versus* the number of PO-DVR grid points for a converged calculation.

The converged parameters for the ISSRP calculations are summarised in table 4.1. In this table, R_{max} is the size of the DVR grid in R (where R ranges from 0 to R_{max}), r_{max} is the size of the DVR grid in r (where r ranges from 0 to r_{max}), E_{cut} is the energy cut-off parameter† which is used in the set-up of the potential optimised DVR, and Δt is the time-step used in the split-operator propagation. The parameters relating to the initial wavepacket are the initial centre of the Gaussian, R_0, the width of the Gaussian, δ, and the average wave-vector, k_0, all of which were described on page 106.

Rigorous convergence tests were carried out for each of the parameters, and the parameters in table 4.1 give converged ISSRP results for all four initial states to graphical accuracy.

The advantage of using the PO-DVR can be seen from table 4.2 which shows the large reduction in the number of radial grid points on changing from a primitive

†We found it best to set V_{max} equal to E_{cut} for these calculations.

Initial state (v, j)	Total propagation time / ps
$(0, 0)$	3.5
$(0, 1)$	2.9
$(1, 0)$	1.4
$(1, 1)$	1.2

Table 4.3 Total propagation times for convergence of the $J = 0$ ISSRP calculations.

DVR [131] to a PO-DVR [208]. Without this reduction these calculations would not have been possible with the computational resources available. For the angular coordinate, γ, we used up to 80 Legendre polynomials. The largest size of the three-dimensional representation for any of the ISSRP calculations was 164,587 (the number of radial grid points for a particular ISSRP calculation obviously depends on the value of J, and decreases with increasing J as a result of the centrifugal barrier $E^J_{0J}(R, r, \gamma)$).

The total propagation times for the $J = 0$ calculations for the four different initial states (v, j) are given in table 4.3. Note that the propagation time for the converged ISSRP calculation decreases with increasing J due to the addition of the effective rotational surface to the potential energy surface which has the effect of making the wells in the surface less deep. This tends to decrease the lifetimes of the metastable states associated with the wells, thus decreasing the total time for which the wavepacket must be propagated.

To calculate the initial state-selected cross sections we required ISSRPs for all values of J which contributed over the energy range of interest. For the initial states $(v = 0, j = 0)$ and $(v = 0, j = 1)$ we needed ISSRPs for $J = 0, 1, \ldots, 60$, while

for the initial states $(v = 1, j = 0)$ and $(v = 1, j = 1)$ we needed ISSRPs for $J = 0, 1, \ldots, 80$.

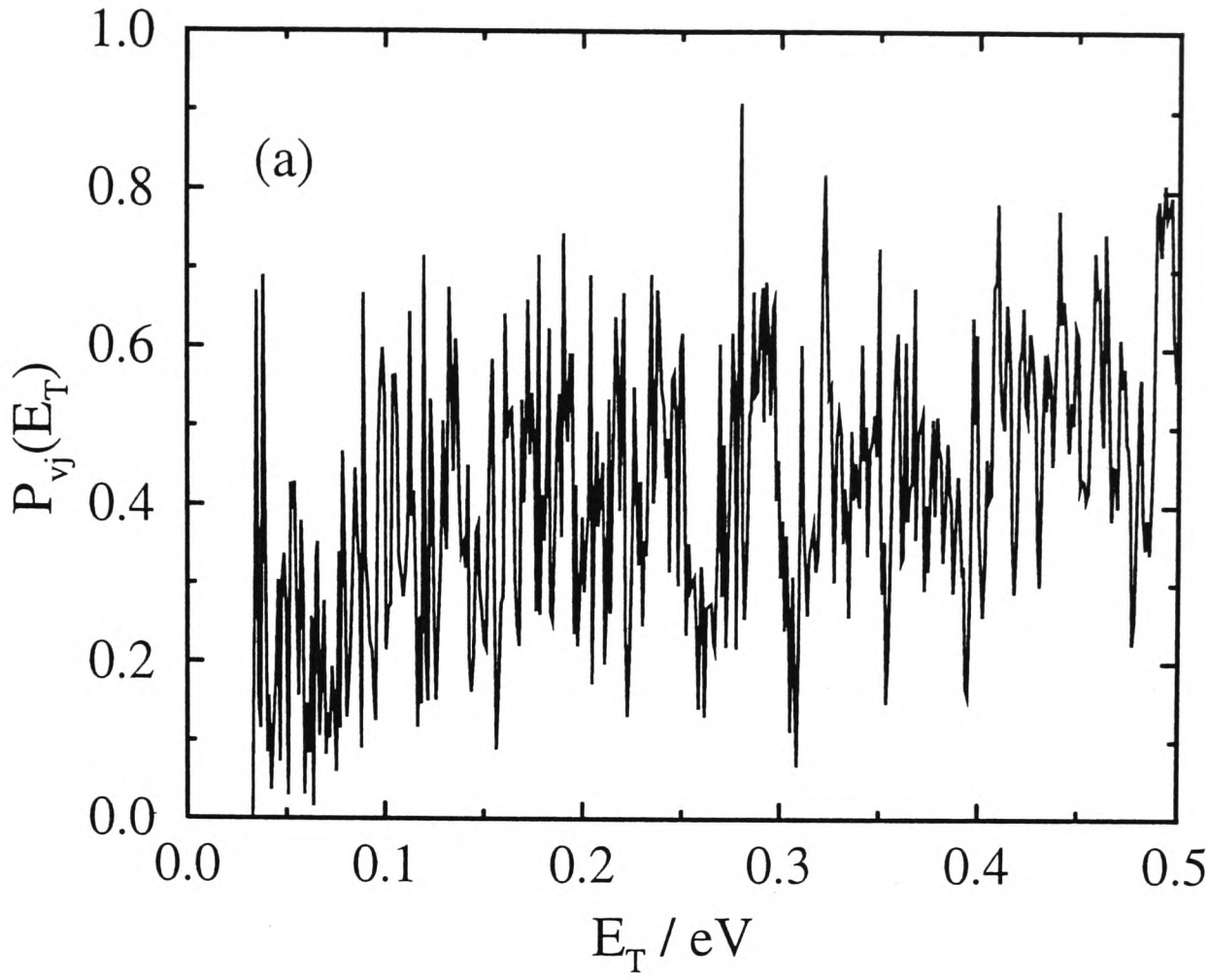
4.3 Results and discussion

4.3.1 Initial state-selected reaction probabilities

In this section we discuss the initial state-selected reaction probabilities (ISSRPs) for total angular momentum $J = 0$ calculated on the WSS surface for reaction (4.1). The results for the four different initial states of the hydrogen molecule are shown in figures 4.6 and 4.7.

Let us begin by considering the results for the $N^+ + H_2(v = 0, j = 0$ and $1)$ reactions in figure 4.6. The first point to be made is that the ISSRPs for these reactions show an extremely dense resonance structure as a function of energy. This structure shows the influence of the deep wells in the PES on the dynamics of the reaction, and provides evidence for the existence of metastable states which lie just above the dissociation limit for the stable species NH_2^+. The fact that the peaks in figure 4.6 are so narrow is one of the factors which contributes to the difficulty of these wavepacket calculations, since not only does the narrowness indicate that the resonances are long-lived and therefore that a long propagation time will be required, but it also means that a dense energy grid is needed in order to resolve the structure satisfactorily. A rough estimate of the average width of the resonances in figure 4.6 implies that the lifetimes of the metastable states in this energy region are of the order of 0.2 ps.

The second point to be made about figure 4.6 is that the reaction probabilities are



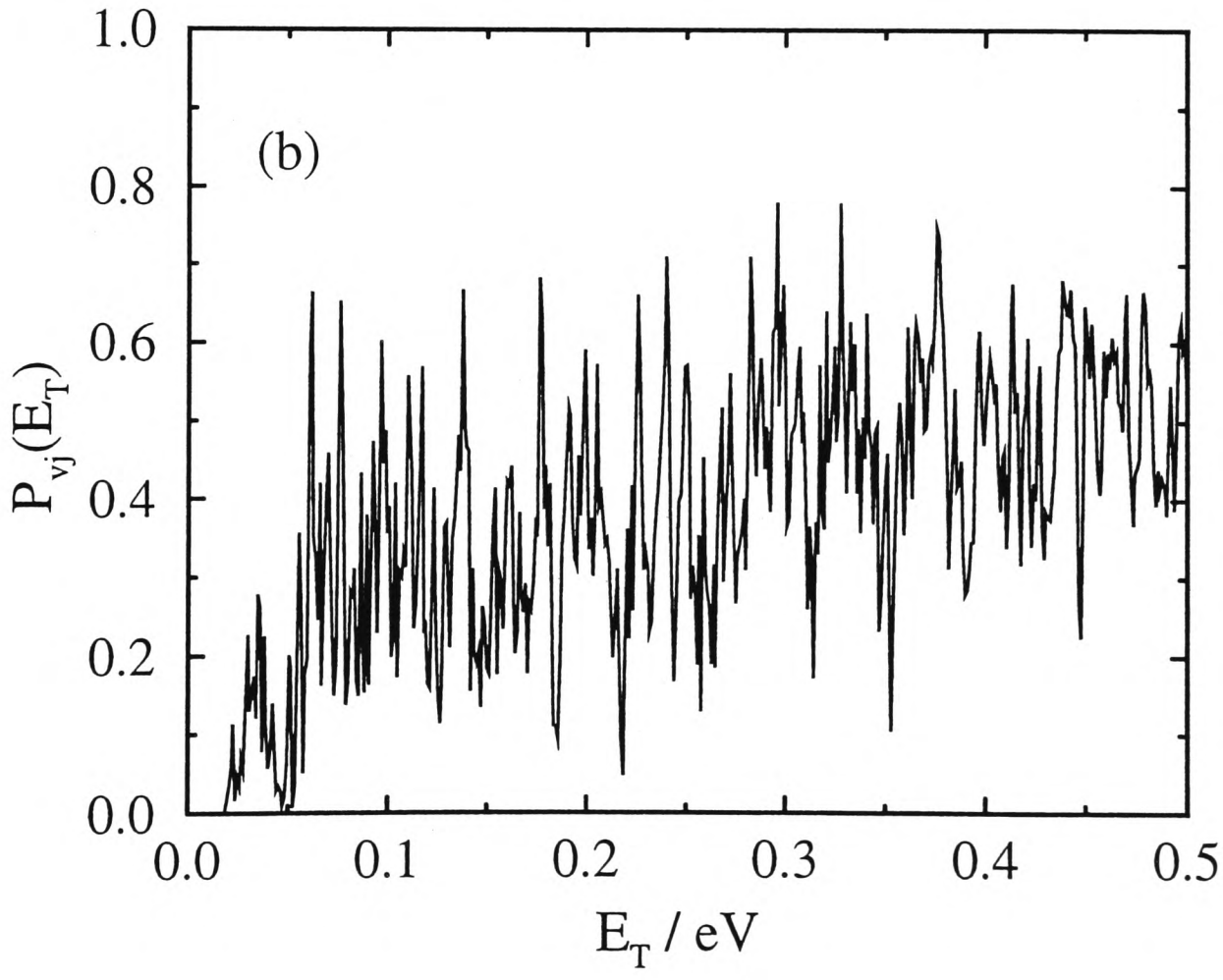
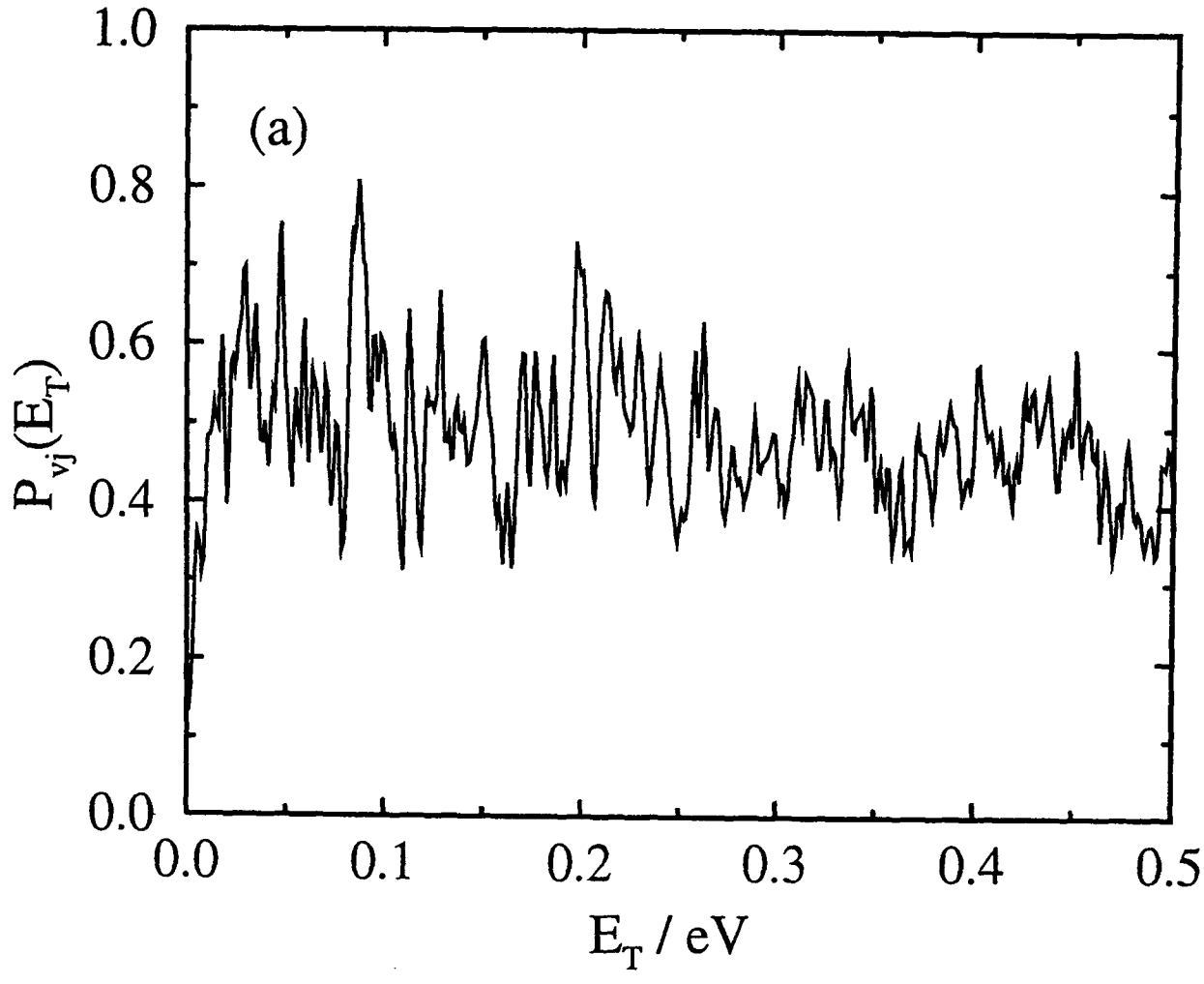


Figure 4.6 Initial state-selected reaction probabilities as a function of translational energy for total angular momentum $J = 0$: (a) $N^+(^3P) + H_2(^1\Sigma_g^+)$ ($v = 0, j = 0$) and (b) $N^+(^3P) + H_2(^1\Sigma_g^+)$ ($v = 0, j = 1$).



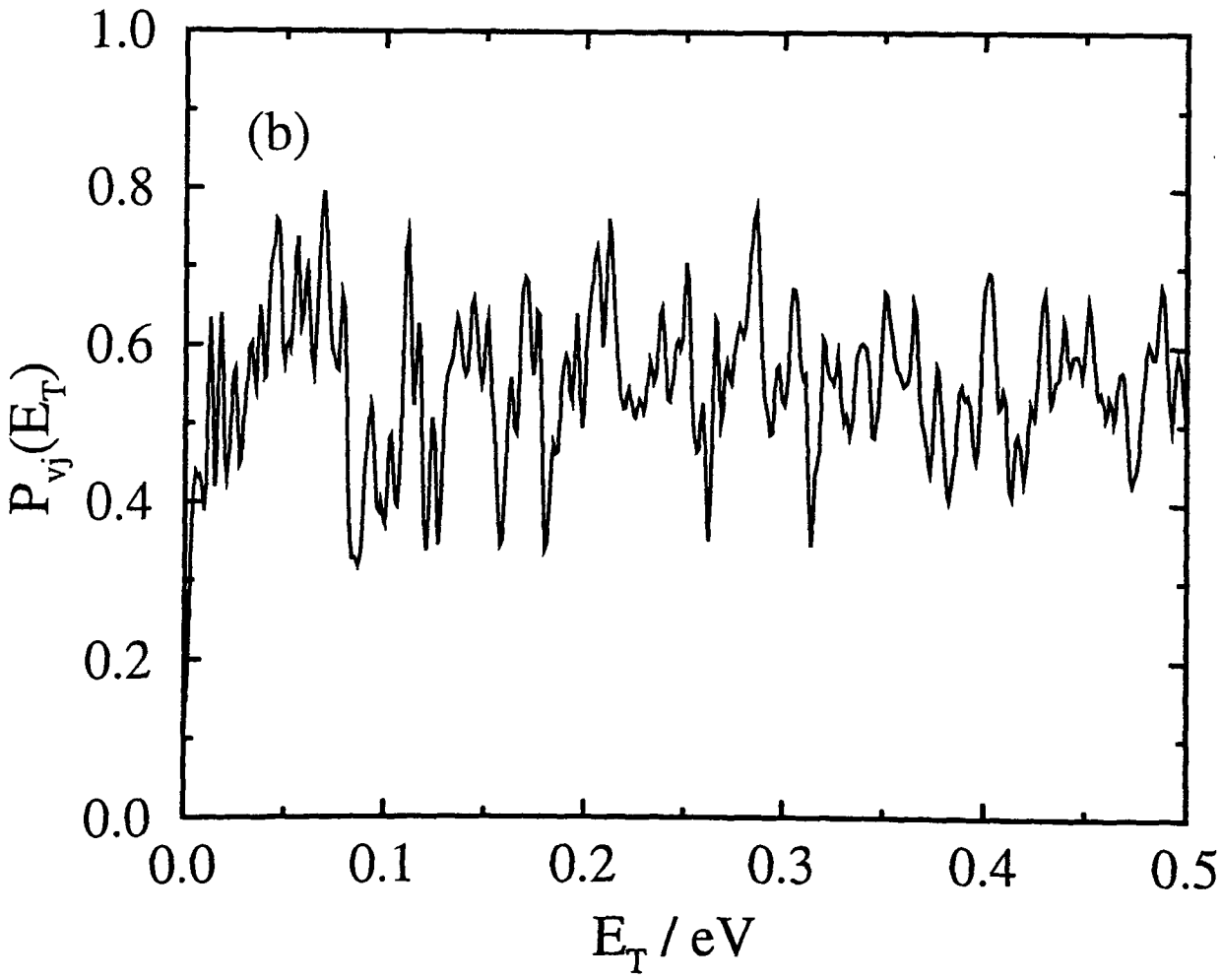


Figure 4.7 Initial state-selected reaction probabilities as a function of translational energy for total angular momentum $J = 0$: (a) $N^+(^3P) + H_2(^1\Sigma_g^+)$ ($v = 1, j = 0$) and (b) $N^+(^3P) + H_2(^1\Sigma_g^+)$ ($v = 1, j = 1$).

zero for both initial states until the translational energy is greater than a certain threshold energy. For the initial state $(v = 0, j = 0)$, this threshold energy corresponds to the quantum mechanical endothermicity of the reaction: 33.0 meV. Despite the fact that the threshold for the reaction is small, it is nevertheless very significant in determining the behaviour of the initial state-selected cross section and reaction rate constant, as will be discussed in section 4.3.2. The calculated ISSRP for the $(v = 0, j = 1)$ initial state in figure 4.6(b) is qualitatively very similar to that for the $(v = 0, j = 0)$ state in figure 4.6(a), the only significant difference being that the threshold energy for the $j = 1$ state is only 18.5 meV due to the higher internal energy of the reactant H_2 molecule. To facilitate the reader's understanding of the energetics of reaction (4.1), a schematic diagram to show the relevant states of the reactants and the ground state of the products on the WSS surface is given in figure 4.8.

We now turn to consider the ISSRP plots for the initial states ($v = 1, j = 0$ and 1) given in figure 4.7. It is immediately apparent that the resonance structure is significantly broader for the ISSRPs in this figure than for those in figure 4.6, and this can be attributed to the higher total energy of the $(v = 1, j)$ initial state compared to that of the $(v = 0, j)$ initial state for the same translational energy. The higher total energy means that the influence of the wells in the PES is less strong for the $v = 1$ states, and this is reflected in broader structure implying that the resonances are shorter-lived at these higher energies. More evidence for the fact that the resonances are shorter-lived for the $v = 1$ calculations is given in table 4.3, where it is clear that converged reaction probabilities are obtained in a much shorter propagation time for these calculations than for those for the $v = 0$ states. An estimate of the average width of the resonances in figure 4.7 implies that the lifetimes are around

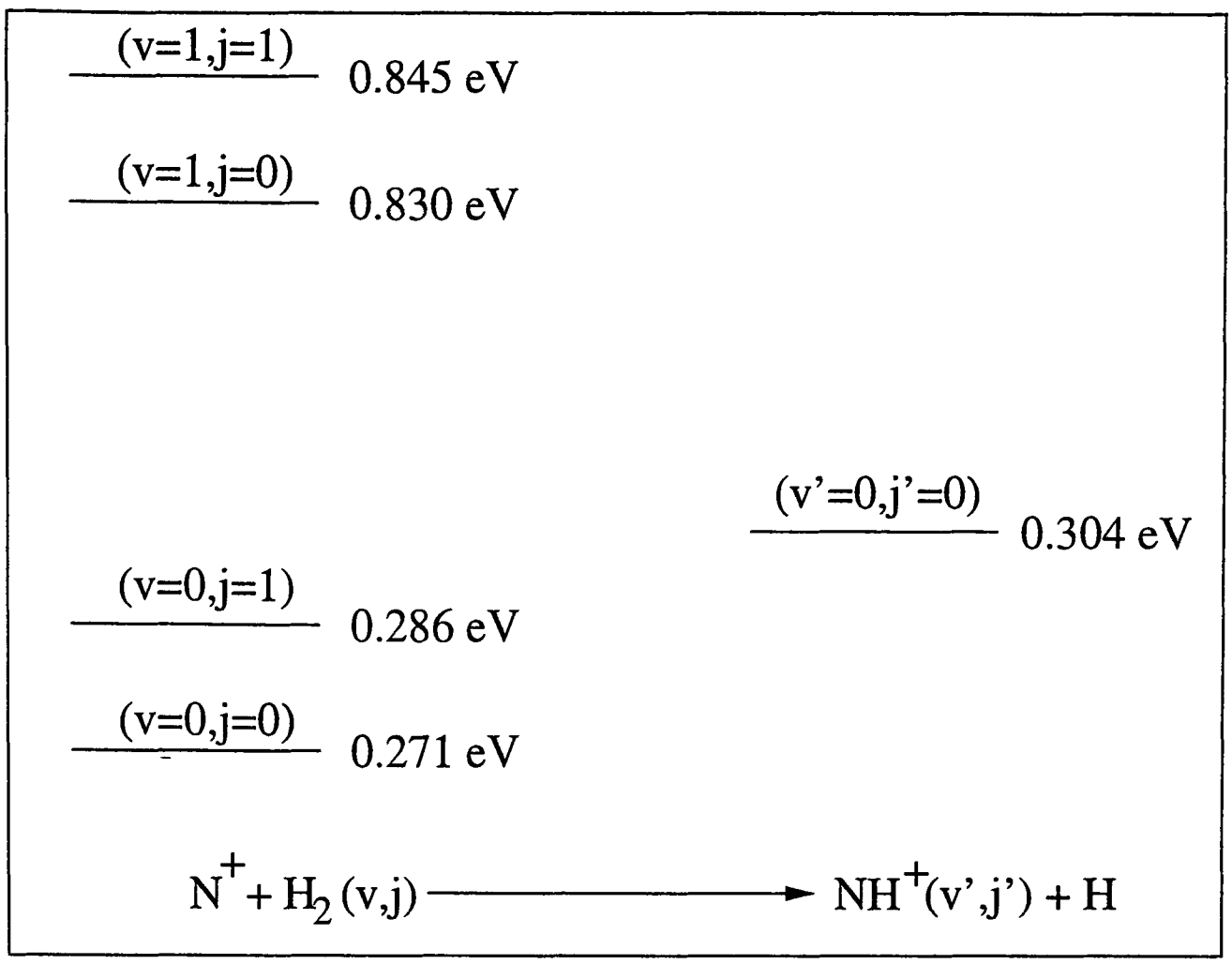


Figure 4.8 Schematic diagram to show the appropriate states of the reactants and the ground state of the products of reaction (4.1). Energies are given relative to the bottom of the asymptotic reactant valley.

0.1 ps in this higher total energy region.

Another important observation to be made from figure 4.7 is that there are no energy thresholds which must be overcome before reaction can take place from the $v = 1$ initial states. The internal energy of H_2 ($v = 1, j = 0$ and 1) is such that reaction (4.1) is exothermic from these initial states, and thus the reaction probabilities can be non-zero for any translational energy $E_T > 0$. The implications of this point will be discussed further in section 4.3.2.

Having completed our discussion of the ISSRPs for total angular momentum $J = 0$, we now move on to illustrate the effect of total angular momentum on the computed reaction probabilities. Figure 4.9 shows the ISSRP as a function of translational energy for the initial state ($v = 0, j = 0$), for several different values of the total

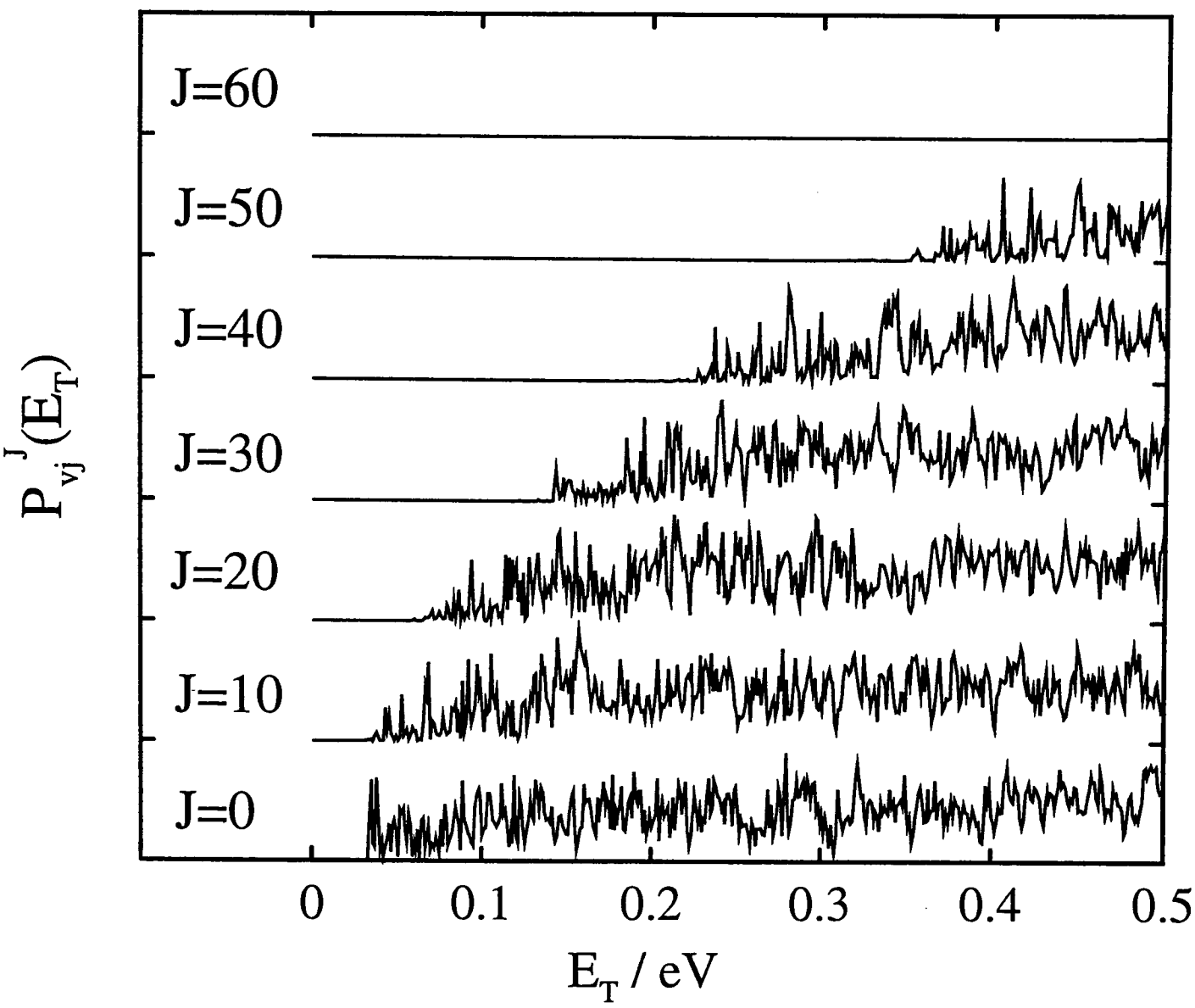


Figure 4.9 Initial state-selected reaction probability as a function of translational energy for $N^+(^3P) + H_2(^1\Sigma_g^+)$ $(v = 0, j = 0)$, at several different values of the total angular momentum quantum number, J, within the rotationally adiabatic approximation.

angular momentum quantum number J. Clearly, as J increases, the energy threshold for the reaction also increases, until by the time J reaches 60 (for this initial state), there is zero reaction probability throughout the energy range of interest. This behaviour is explained by the growth of the centrifugal barrier [1] as the total angular momentum increases, such that it becomes progressively more difficult to react as J gets larger.

This concludes our discussion of the ISSRP results obtained from the wavepacket calculations. In the next section we present the initial state-selected cross sections obtained by summing the appropriate ISSRPs, and compare these cross sections

with those obtained in previous work on this reaction.

4.3.2 Initial state-selected cross sections

Initial state-selected cross sections were obtained from the ISSRPs discussed in the previous section using the expression given in equation (2.43) in conjunction with equation (4.48). In this section we shall present and explain the results obtained from these calculations, and then go on to compare these results with those obtained using a quasi-classical trajectory (QCT) method on the same surface.

The cross sections for the four initial states are shown in figure 4.10. The first point to be made about this figure is that there is clearly a striking difference between the cross sections obtained for the initial states with $v = 0$, and those obtained for the initial states with $v = 1$. The cross sections for the $v = 0$ states are zero until the translational energy is greater than a threshold energy (corresponding to the threshold for $J = 0$ discussed in section 4.3.1), after which they increase as a function of energy until they reach a plateau. In contrast, the cross sections for the $v = 1$ states increase sharply at the lowest translational energies to an extremely large value, and then decrease as a function of energy.

The explanation for this difference in behaviour lies in the fact that the reaction is endothermic if the reactants are in the $(v = 0, j = 0)$ or $(v = 0, j = 1)$ states, but exothermic if the reactants are in the $(v = 1, j = 0)$ or $(v = 1, j = 1)$ states (see figure 4.8). Recall from section 2.3.2 that the behaviour of the cross section at low energies is very different for an endothermic reaction compared with an exothermic reaction which proceeds without a barrier, and that this can be understood in the light of equation (2.43). Bearing this in mind, the strong dependence of the cross

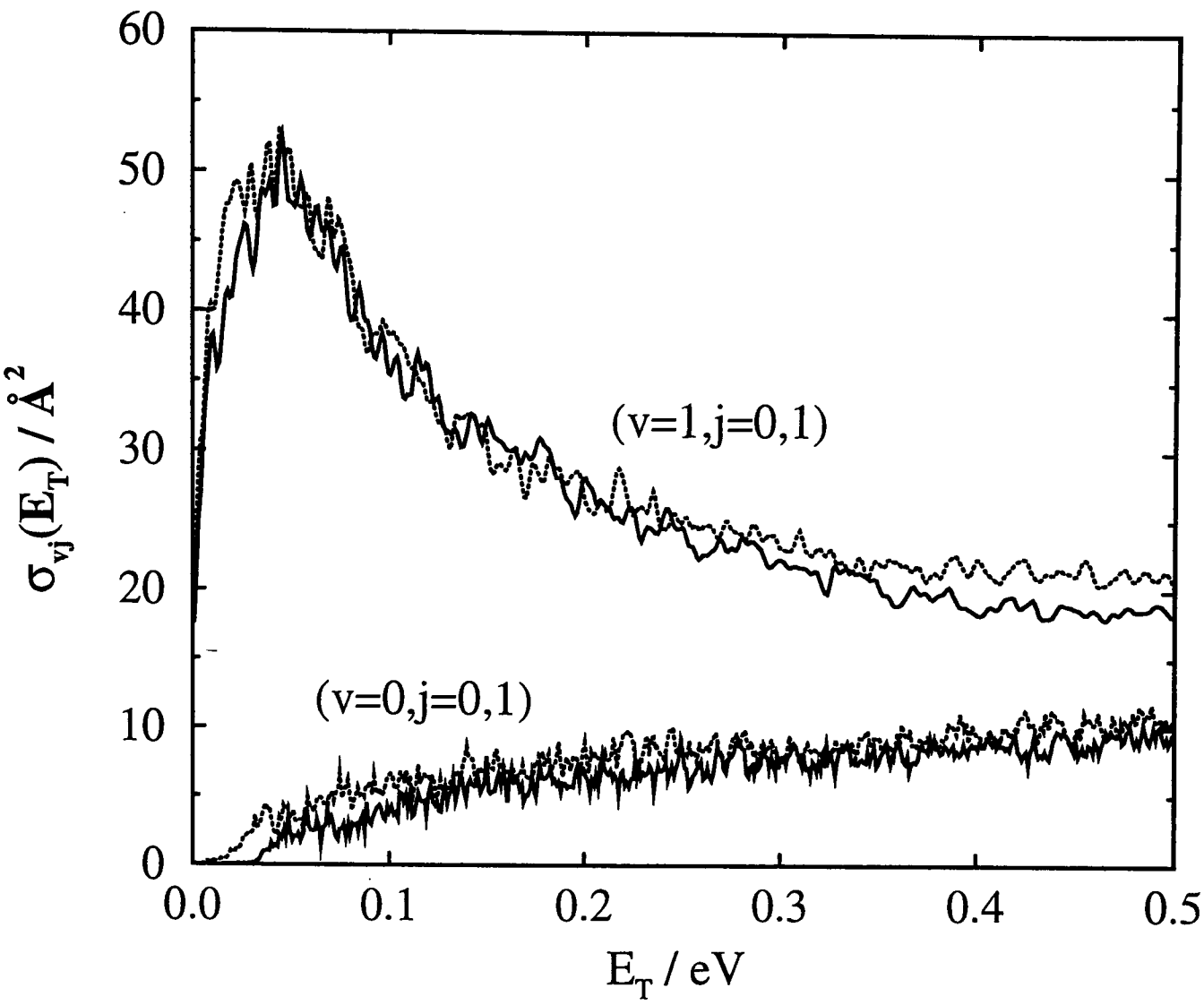


Figure 4.10 Initial state-selected reaction cross sections as a function of translational energy for the reactions $N^+ + H_2(v = 0 \text{ and } 1, j = 0 \text{ and } 1)$, where the solid lines are the results for $j = 0$ and the dotted lines are the results for $j = 1$.

section on the initial vibrational state of the reactants, as illustrated in figure 4.10, becomes easy to understand.

We now focus our attention on the cross sections from the $v = 1$ initial states. In figure 4.11 we show these cross sections along with the classical Langevin capture cross section which was introduced in section 2.3.2 (see equation (2.45)). It can be seen from figure 4.11 that the cross sections calculated in our wavepacket calculations for the $v = 1$ initial states are qualitatively very similar to the results of the simple Langevin theory except at very low translational energies. However, the fact that our reaction cross sections are actually larger than the capture cross section at high

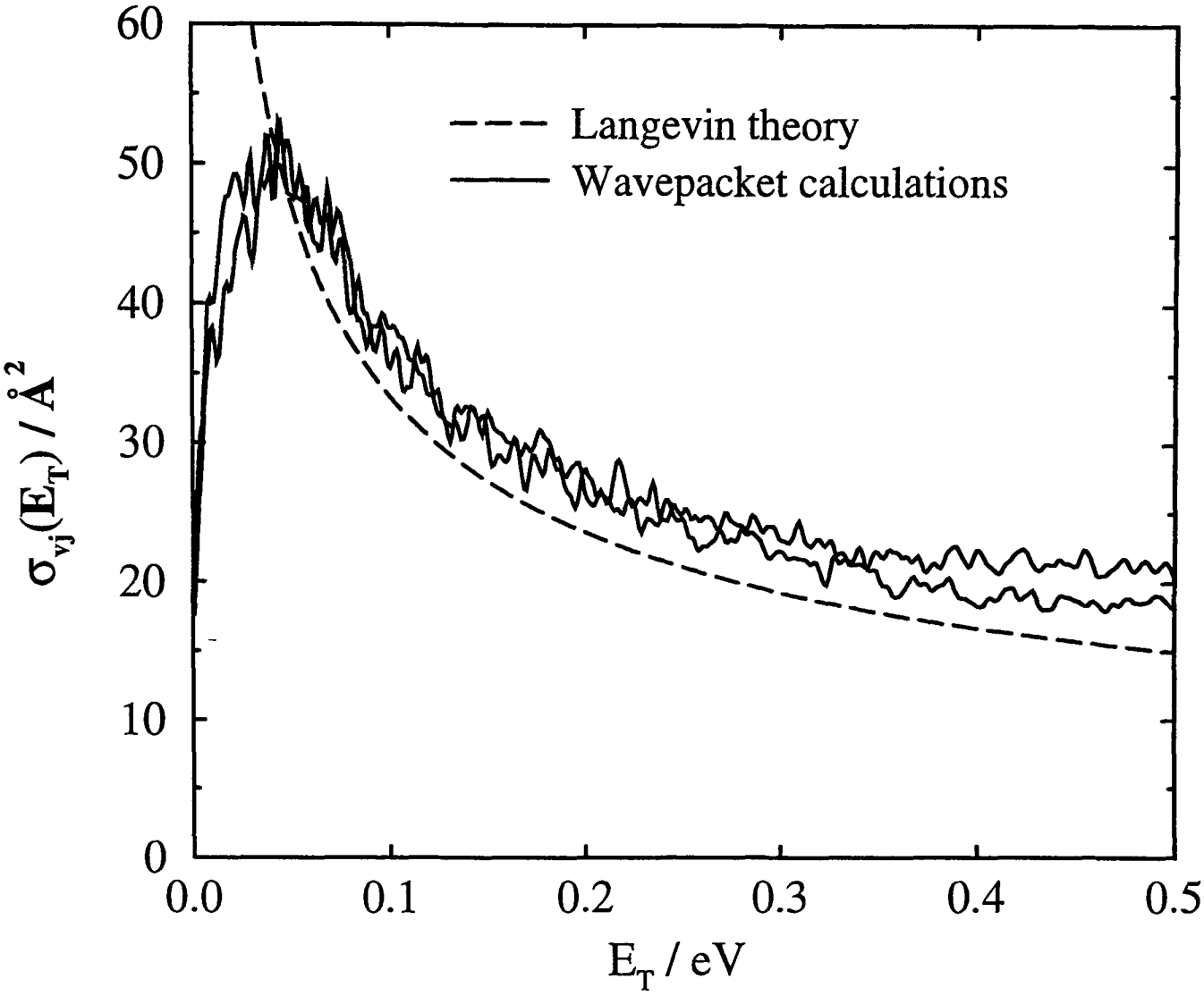


Figure 4.11 Initial state-selected reaction cross sections from the wavepacket calculations for $N^+(^3P)+H_2(^1\Sigma_g^+)$ ($v = 1, j = 0$ and 1), compared with the Langevin classical capture cross section discussed in the text.

energies is somewhat surprising. Presumably this is due either to the excitation of the reactant H_2 molecule, or to the anisotropic (ion-quadrupole and ion-induced-dipole) interactions in the reactant valley of the WSS surface (which are not taken into account properly in simple Langevin theory).

Having presented the cross sections obtained from the wavepacket calculations described in this chapter, we shall now move on to compare our results with those of some earlier calculations carried out on the same WSS potential energy surface. These calculations were carried out by Nyman and Wilhelmsson using a standard quasi-classical trajectory (QCT) method [201]. Among other quantities, these au-

thors calculated the reaction cross section from a particular initial state of the reactants, $(v = 0, j = 1)$, which can be compared directly with the results of our quantum mechanical calculations.

Figure 4.12 shows the initial state-selected cross section for reaction (4.1) from the $(v = 0, j = 1)$ state of the reactants, both from the wavepacket calculations presented in this chapter, and from the QCT calculations of Nyman and Wilhelmsson [201]. It is clear that there is a very large discrepancy between the results of the two calculations. The quantum mechanical (QM) cross section is zero until a threshold energy is reached (18.5 meV for this initial state) and then increases as a function of energy before reaching a plateau. In contrast, the QCT cross section is extremely large at low energies, and then decreases as a function of energy before levelling off to roughly the same plateau as in the QM calculation. How can we explain such a marked difference between the results of the two calculations?

To answer this question we must consider the importance of vibrational zero-point energies (ZPEs) in the light of the near-thermoneutrality of reaction (4.1). The QM calculations treat ZPE correctly throughout the calculation. In other words, the reactants start with the correct vibrational ZPE, the products finish with the correct vibrational ZPE, and the ZPE is treated correctly throughout the entire wavepacket propagation[†]. In contrast, in the QCT calculations described in reference [201], the trajectories start off with the correct amount of vibrational ZPE in the H_2 molecule, but due to the inability of the standard QCT method to "conserve" ZPE [7, 209], the products can be formed without the necessary quantum mechanical ZPE in the NH^+. In reaction (4.1), where the endothermicity is very small, the failure of the

[†]Note that the ZPE of H_2 is 0.269 eV, and the ZPE of NH^+ is 0.187 eV [173].

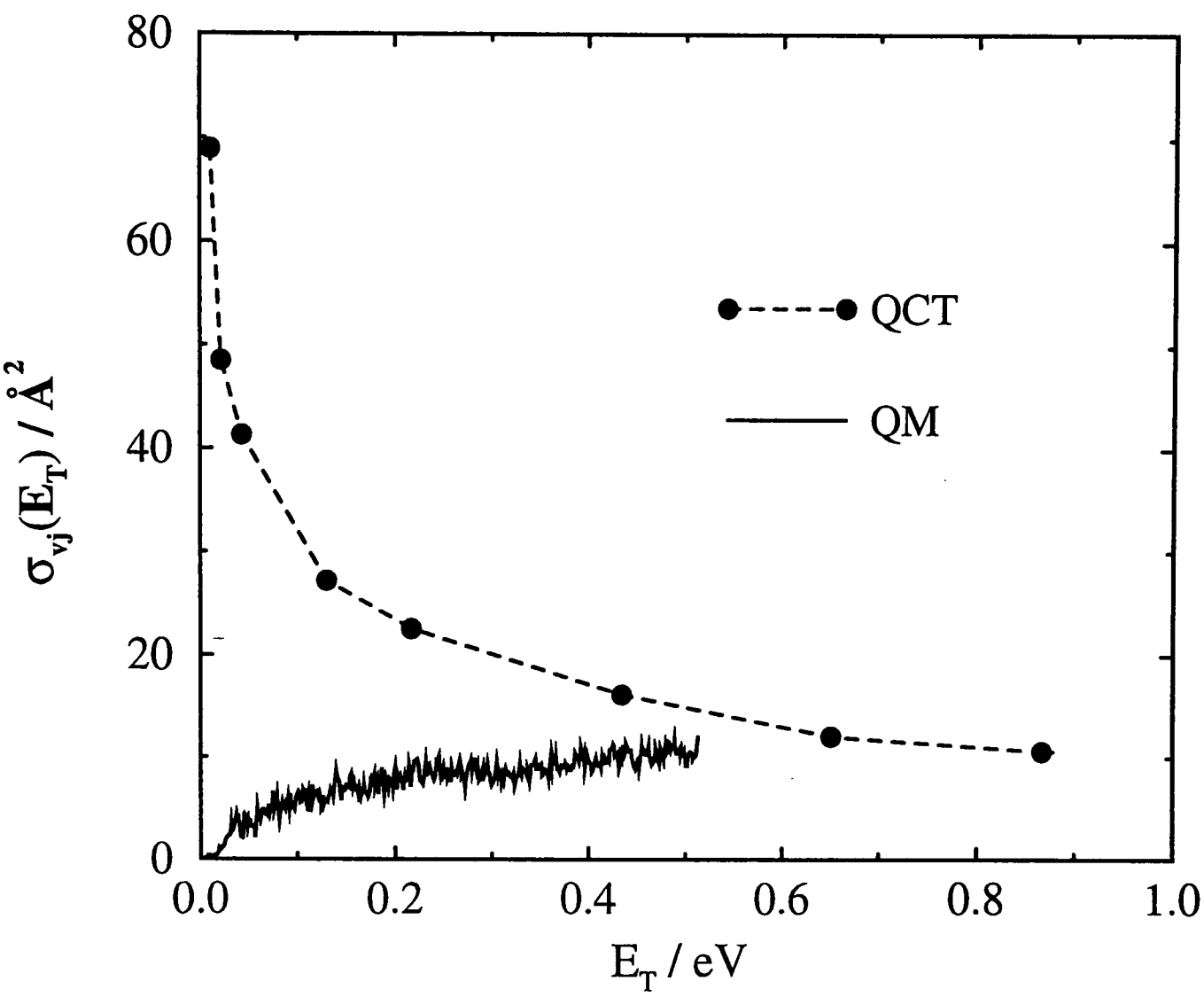


Figure 4.12 Initial state-selected reaction cross sections for the reaction $N^+(^3P)+H_2(^1\Sigma_g^+)$ $(v=0, j=1)$ as calculated both quantum mechanically (QM; this work), and using a quasi-classical trajectory method (QCT; reference [201]).

standard QCT method to ensure that the products are formed with the correct ZPE means that while the QM calculation from the $(v=0, j=1)$ initial state "sees" an endothermic reaction, the QCT calculation "sees" an exothermic reaction, and thus gives the wrong cross section behaviour in the threshold region (*cf.* figure 2.5). This point is illustrated in figure 4.13, which gives a schematic diagram appropriate to the energetics of reaction (4.1) from either of the initial states, $(v=0, j=0)$ or $(v=0, j=1)$.

It is pleasing to note from figure 4.12 that at higher energies the QM and QCT cross sections appear to converge on the same value. This provides a nice illustration

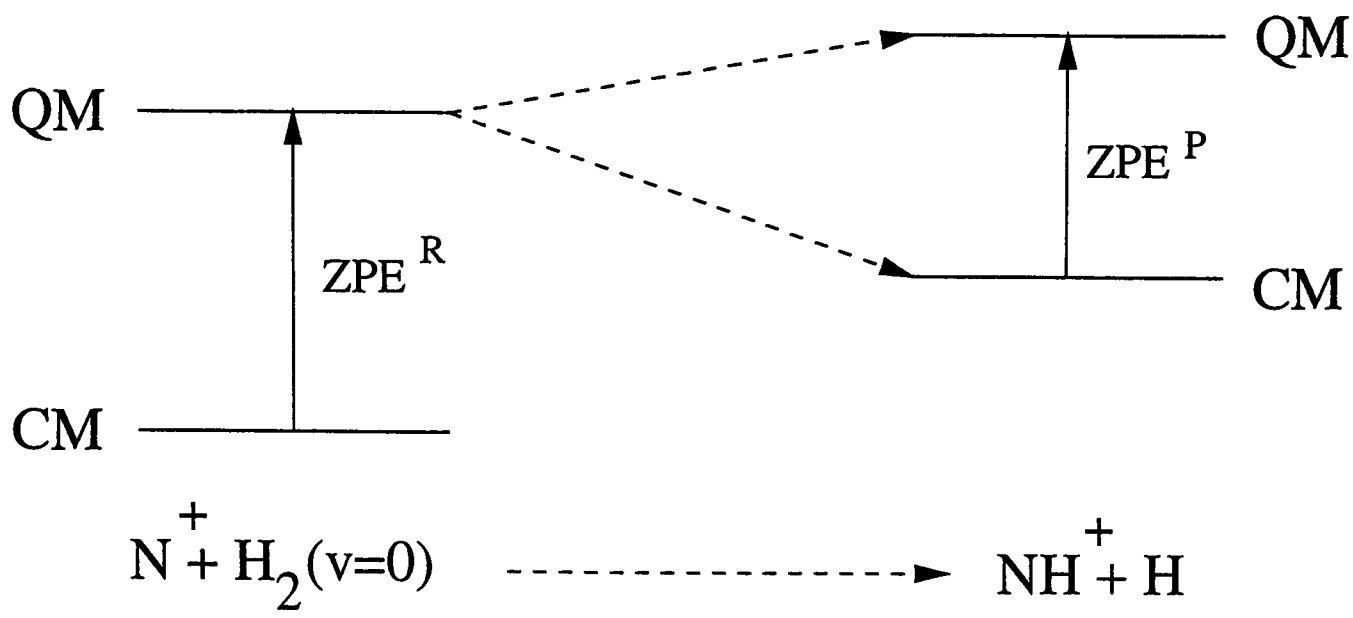


Figure 4.13 Illustration of the importance of vibrational zero-point energies in a nearly-thermoneutral reaction. The classical mechanical (CM) state of the reactants or products lacks the correct zero-point energy of the quantum mechanical (QM) state.

of the correspondance of quantum mechanics and classical mechanics in the high-energy limit where there are many open states, and also encourages confidence in the rotationally adiabatic approximation that was used in the present wavepacket calculations (all the more so because of the additional approximation we made for the $j = 1$ initial state as described in section 4.2.2).

Overall, it appears from a comparison of the low-energy cross sections calculated using the QM and QCT methods, that in order to predict correctly the behaviour of reaction (4.1) in the threshold region, it is essential to use a method which will treat vibrational zero-point energies correctly. This point is particularly important in the context of the astrophysical significance of the reaction (discussed in section 4.1.2), since the astrophysics community is interested in the behaviour of the reaction at the low temperatures (<40 K) of dense interstellar clouds. The low-temperature rate of reaction (4.1) will be dominated by the behaviour of the reaction cross section at low energies, and we have thus shown that for theoretical results to have any bearing on the astrophysical significance of the reaction, they *must* have been obtained using a

method which treats vibrational zero-point energies correctly.

Before moving on to discuss the initial state-selected rate constants which we calculated from our initial state-selected cross sections, one final point remains to be made. While there have been attempts to measure reaction cross sections for the $N^+ + H_2$ reaction experimentally [173, 184, 185, 205], these were severely affected in the threshold region by problems such as energy broadening which made it impossible to determine the "true" cross section. The only measurable quantity was a convolution of the "true" cross section with a broadening function, as a result of which there has been a great deal of difficulty in determining the precise low-energy behaviour of the cross section experimentally. Because of this, we decided to limit ourselves to comparing our cross sections with the QCT cross sections calculated using the WSS surface, and only to make experimental comparisons with rate constant data.

In the next section we proceed to discuss the initial state-selected rate constants obtained from the quantum mechanical cross sections presented above.

4.3.3 Initial state-selected rate constants

The initial state-selected rate constants, $k_{vj}(T)$, were calculated from the cross sections presented above using equation (2.46). The results for the four initial states are given in figure 4.14, where they are presented in the form of an Arrhenius plot.

The first point to be made from this figure is that the rate of the reaction at low temperatures shows a very strong dependence on the initial state of the H_2 molecule. It is clear from figure 4.14 that at low temperatures the rate of reaction from the

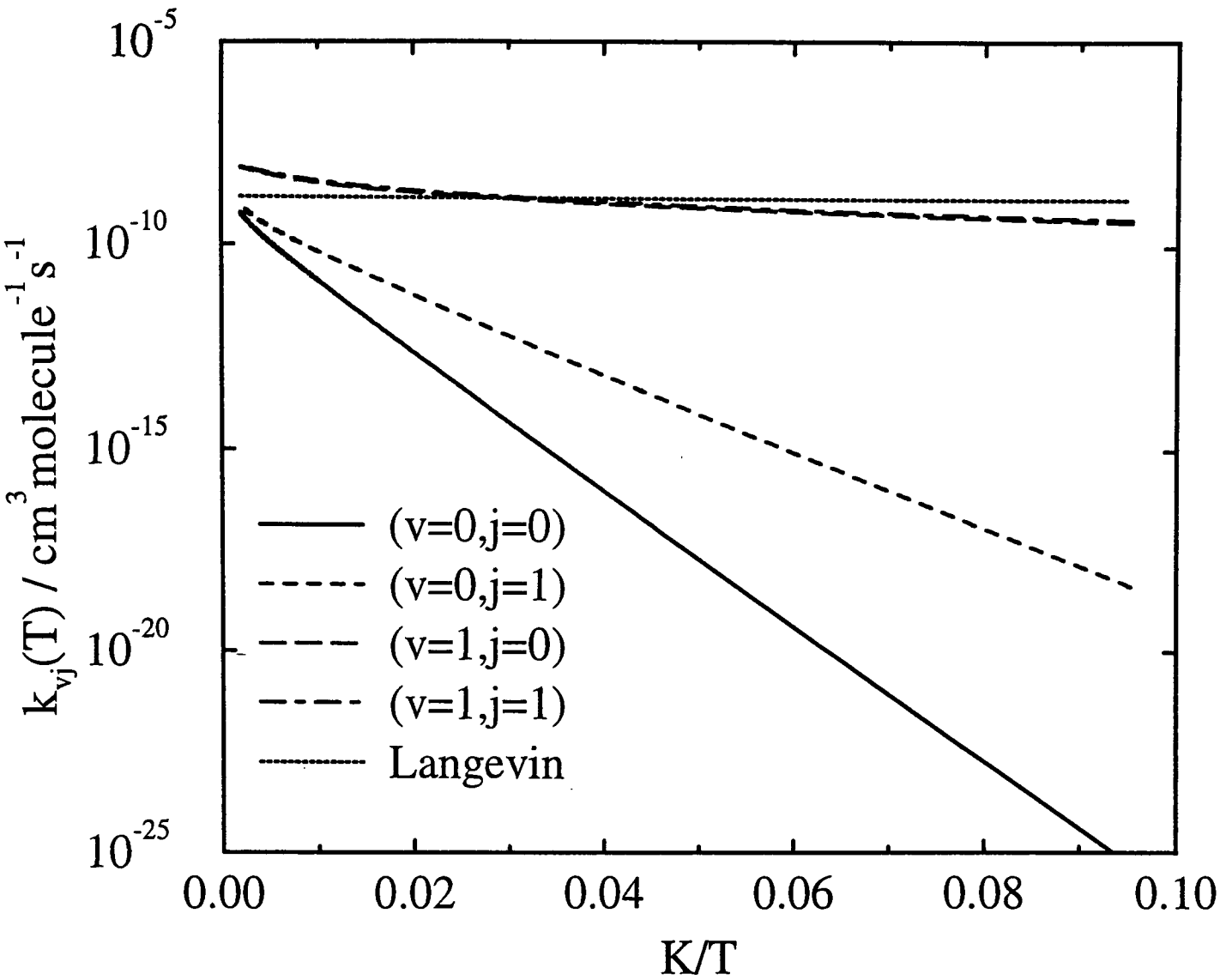


Figure 4.14 Initial state-selected reaction rate constants for the reaction $N^+(^3P) + H_2(^1\Sigma_g^+)$ ($v = 0$ and 1, $j = 0$ and 1), shown along with the temperature-independent Langevin capture rate constant defined in the text.

initial state ($v = 0, j = 0$) is very much lower than that from ($v = 0, j = 1$), and that this in turn is lower than the reaction rate from either of the $v = 1$ states (for which the rate is almost independent of both the temperature and the initial j quantum number). It is clear from this that when the reaction is taking place from an initial state from which it is endothermic, the rate of reaction is strongly dependent on the exact amount of internal energy in the reactants, and also strongly dependent on the temperature. However, once the internal state of the reactants is sufficiently high in energy that the reaction is exothermic, the exact amount of energy in the internal state is less important, and the rate is almost independent of temperature.

We therefore conclude that the dependence of the calculated rate of reaction (4.1) on the initial state of the reactants is predominantly a thermicity effect rather than any more subtle dynamical effect, which is perhaps not too surprising in a reaction which is so nearly thermoneutral.

Recall from section 4.1.2 that it is thought that there may be areas in dense interstellar clouds which contain vibrationally-excited H_2. From figure 4.14 it is obvious that this would have a strong impact on the rate of reaction (4.1), and thus a strong impact on its feasibility as the first step in the interstellar formation of ammonia.

It can be seen from figure 4.14 that an Arrhenius plot produces near-linear behaviour for the rate constants from all four initial states. However, a better fit to the rate constant data from the $(v = 0, j = 0)$ and $(v = 0, j = 1)$ states was obtained using the following model expression for the rate constants:

$$k_{vj}(T) = A\ T^{1/2}\ e^{-E_0/k_B T}, \tag{4.53}$$

where A and E_0 are constants. This is the rate constant expression obtained from simple collision theory [210]. It is pleasing to note that when using equation (4.53), the values for E_0 obtained in the fitting procedure correspond very nearly to the endothermicity of the reaction from the initial state in question (E_0 is 32 meV for $(v = 0, j = 0)$ and 18 meV for $(v = 0, j = 1)$).

There has been a good deal of discussion in the literature about whether rotational energy in the reactant H_2 molecule is as efficient as relative translational energy in promoting the rate of the reaction [173, 182, 183, 184, 185]. In order to investigate this question using our results we took our cross section for $(v = 0, j = 0)$ and shifted it along the translational energy axis by -14.5 meV (corresponding to the

difference in energy between the ($v = 0, j = 0$) and ($v = 0, j = 1$) states). We then calculated the rate constant from this shifted cross section, and compared it to the ($v = 0, j = 1$) data shown in figure 4.14, and we found that the two sets of rate constants were virtually identical to graphical accuracy. This suggests that rotational energy in the reactant H_2 *is* as effective as relative translational energy in promoting the rate of reaction (4.1) when one is considering initial states from which the reaction is endothermic.

We have included in figure 4.14 the value for the Langevin theory prediction of the rate constant. This classical capture theory, which was introduced in section 2.3.2, predicts a temperature-independent rate constant for reaction (4.1) of 1.58×10^{-9} cm^3 molecule^{-1} s^{-1}, and it can be seen that the results of our wavepacket calculations for the $v = 1$ initial states are close to this value. The small differences between our rate constants and the Langevin rate constant can be accounted for by looking back at the cross sections in figure 4.11. It can be seen in this figure that classical Langevin theory underestimates the cross sections from the wavepacket calculations at all but the very lowest energies, which explains why the Langevin rate constant is lower than the rate constants obtained in our wavepacket calculations at all but the lowest temperatures. At the very lowest energies, the Langevin cross section overestimates the cross sections from the wavepacket calculations, which explains why the Langevin rate constant is greater than our rate constants at very low temperatures.

We have now concluded our discussion of the initial state-selected rate constants. In the next section we discuss the calculation of thermal rate constants from these initial state-selected rate constants.

4.3.4 Thermal rate constants

As we mentioned in section 2.3.3, initial state-selected rate constants are not the same as thermal rate constants because thermal rate constants involve an average over all the initial states of the reactants. In this section we discuss the issues involved in the calculation of thermal rate constants for reaction (4.1), and then present the results we obtained using two different models. Finally, we compare these results with some experimental work which has been carried out, and make some suggestions concerning the endothermicity of the reaction.

The wavepacket calculations presented in this chapter were carried out on the WSS ground-state adiabatic PES [193], which can be interpreted as corresponding to reaction between the lowest spin-orbit state of $N^+(^3P)$ (the $^3P_0$ state), and $H_2(^1\Sigma_g^+)(v,j)$. However, in order to calculate thermal rate constants for the reaction, we must take into consideration *all* of the possible states of the reactants which are accessible over the temperature range of interest. This means we must consider not only the excited rotational states of the H_2 molecule (in a thermal distribution, excited vibrational states are not occupied over the temperature range of interest), but also the excited spin-orbit states of the $N^+(^3P)$ ion (see figure 4.15).

The electronic near-degeneracy of the $N^+(^3P)$ ion means that the expression for the thermal rate constant for reaction (4.1) is not quite as simple as the one given in equations (2.47) and (2.48). Instead we have

$$k(T) = \frac{\sum_j g_j e^{-E_j/k_B T} k^j(T)}{\sum_j g_j e^{-E_j/k_B T}}, \tag{4.54}$$

with

$$k^j(T) = \frac{\sum_i g_i e^{-\Delta_{0i}/k_B T} k_i^j(T)}{\sum_i g_i e^{-\Delta_{0i}/k_B T}}. \tag{4.55}$$

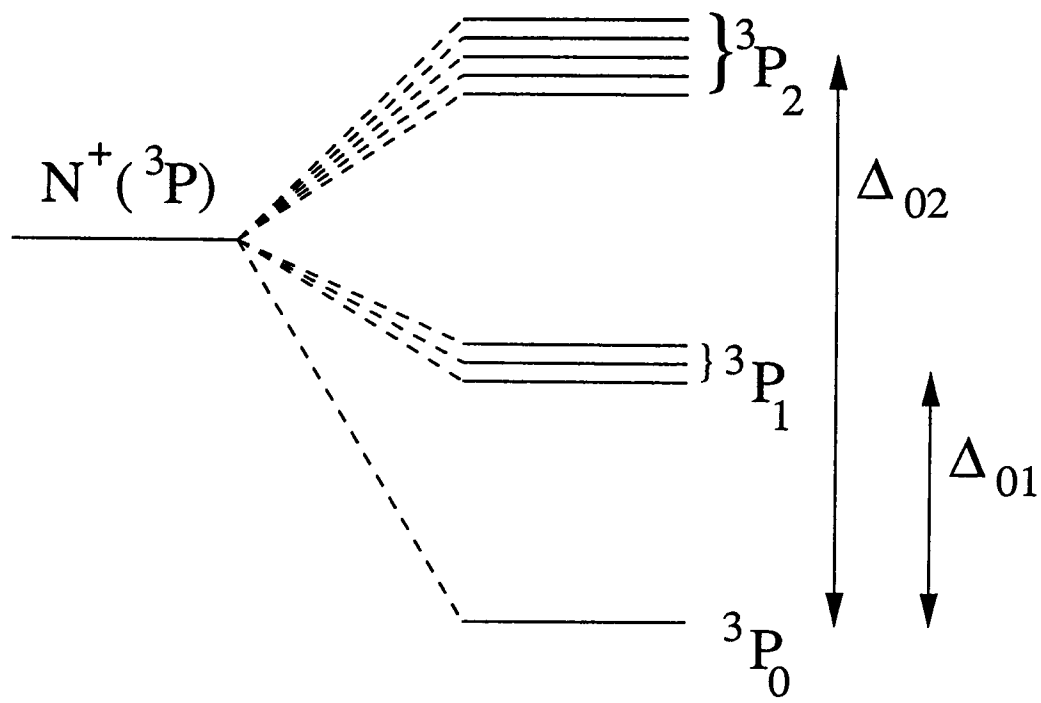


Figure 4.15 Spin-orbit states of the $N^+(^3P)$ ion, where $\Delta_{01} = 0.0061$ eV, and $\Delta_{02} = 0.0162$ eV.

Here, $k_i^j(T)$ is the initial state-selected rate constant for reaction between the rotational state j of the H_2 ($v = 0$) molecule and the spin-orbit state i of the N^+ ion (i can take the values 0,1,2), g_i and g_j are the degeneracies of the ith spin-orbit state and the jth rotational state respectively, Δ_{0i} is the energy of the ith spin-orbit state relative to the ground spin-orbit state, and E_j is the energy of the jth rotational state relative to the ground rotational state.

In order to implement equations (4.54) and (4.55) it is necessary to make some assumptions. From our wavepacket calculations we know $k_0^j(T)$ for $j = 0$ and 1, but we have no values for $k_1^j(T)$ or $k_2^j(T)$. The effect of excited spin-orbit states on this reaction has been the subject of a considerable amount of debate in the literature [158, 182, 183, 186, 200, 211], but as yet there have not been any *ab initio* calculations or experiments carried out which determine this effect conclusively.

In our work we shall follow Wilhelmsson and Nyman [200] in assuming that of the nine spin-orbit states of the $N^+(^3P)$ ion, only the three lowest are reactive. This model can be justified to some extent by studying the electronic correlation diagram

given in figure 4.3. It is clear from this diagram that of the three triplet surfaces which correlate with the reactants, only one surface allows access to the wells in the PES without going *via* a large barrier. As a result, it is reasonable to assume that only this surface is reactive at the low energies we are interested in. In this picture, therefore, only three of the nine $N^+(^3P)$ spin-orbit states are reactive, these being the lowest three adiabatically, *i.e.*, the $^3P_0$ and two of the three $^3P_1$ states.

In addition to deciding which of the spin-orbit states of the N^+ ion are reactive, it is also necessary to know the effect of spin-orbit energy on the rate of the reaction. In our case, we need to know $k_1^j(T)$, given that in our wavepacket calculations we only obtained $k_0^j(T)$. All that we can reasonably hope to do about this here is to examine the following two limiting models:

1. Spin-orbit energy is not available to promote the reaction,
2. Spin-orbit energy is as efficient as relative translational energy in promoting the reaction.

We now describe how to implement each of these before presenting the results.

For the first case, in which spin-orbit energy is not available to promote the reaction, the value of $k_1^j(T)$ is equal to $k_0^j(T)$. In this case, equation (4.55) reduces to the same multi-surface correction factor as was employed by Wilhelmsson and Nyman [200]:

$$k^j(T) = \frac{1 + 2e^{-\Delta_{01}/k_BT}}{1 + 3e^{-\Delta_{01}/k_BT} + 5e^{-\Delta_{02}/k_BT}} k_0^j(T). \tag{4.56}$$

In the second case, in which spin-orbit energy is fully available to promote the reaction, $k_1^j(T)$ is not equal to $k_0^j(T)$, and thus equation (4.55) becomes:

$$k^j(T) = \frac{k_0^j(T) + 2e^{-\Delta_{01}/k_BT} k_1^j(T)}{1 + 3e^{-\Delta_{01}/k_BT} + 5e^{-\Delta_{02}/k_BT}}. \tag{4.57}$$

In order (approximately) to calculate $k_1^j(T)$, we simply shift the appropriate reaction cross section (*i.e.*, the cross section for the initial state $(v = 0, j)$) along the translational energy axis by the value $-\Delta_{01}$, and then use this shifted cross section to calculate the rate constant by thermally averaging it with a Maxwell-Boltzmann distribution in the usual way.

Note that over the temperature range we studied, a thermal distribution of rotational states of H_2 indicates that there are small populations in $j = 2$ and $j = 3$. For the WSS surface, reaction (4.1) is exothermic from each of these two rotational states, so we assumed the rate constant to be equal to the Langevin value in these cases, namely 1.58×10^{-9} cm^3 molecule^{-1} s^{-1}.

The results from the two models described above are shown in figure 4.16 for the temperature range 10 K< T < 100 K. Our results are shown with Gerlich's recent experimental results for $N^+ + n$-H_2 which were obtained using a variable-temperature 22-pole ion-trap [184]. We chose to compare our results with Gerlich's data because they are the best and most recent experimental results available for the reaction[†].

It is immediately obvious from figure 4.16 that the thermal rate constants predicted by our wavepacket calculations are far too small compared with the experimental results. The results from model 2, in which spin-orbit energy is fully available to promote the reaction, are slightly larger than those from model 1, but the effect of this is by no means large enough to bring the theoretical results in line with

[†]Note that the data plotted in figure 4.16 were obtained from the raw experimental data provided by Prof. Gerlich by first binning together all the data points within a 5 K range (since the estimated uncertainty in the temperature was 5 K), and then finding the mean and standard deviation of the rate coefficient within each temperature bin containing four or more data points.

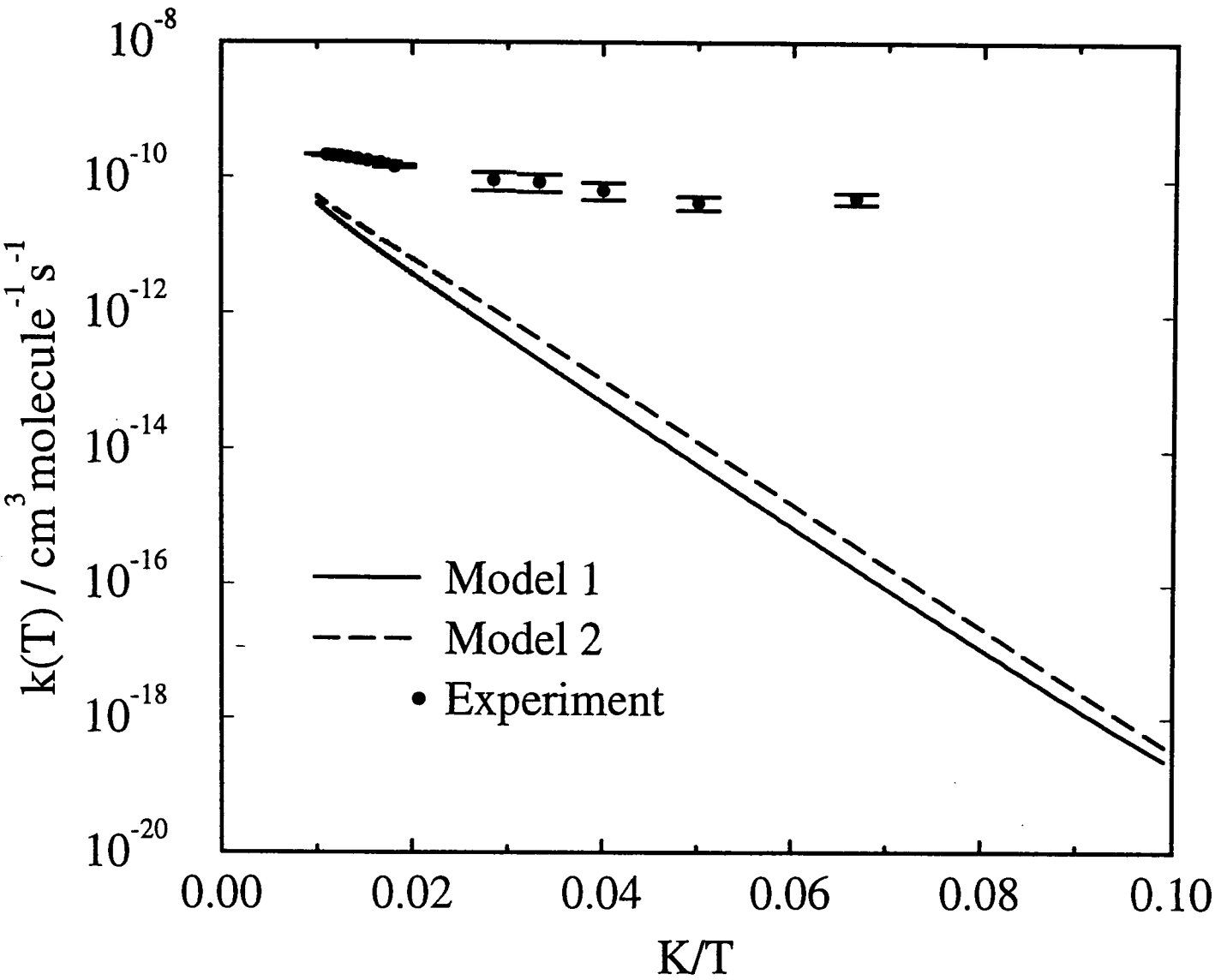


Figure 4.16 Thermal rate constants for $N^+ + n\text{-}H_2$ as calculated from our wavepacket results using two different models for the effect of $N^+(^3P)$ spin-orbit excitation, compared with Gerlich's variable-temperature ion trap experimental data [184].

experiment. The conclusion which can be drawn from this is that the endothermicity of the WSS surface (33 meV) is probably too large, and that this makes the rate constants generated on the surface smaller than those measured experimentally. As we mentioned previously, recent experimental estimates of the endothermicity of reaction (4.1) have ranged from 11 meV to 33 meV, with the consensus now tending towards a value of around 17 meV, thus it is perhaps not too surprising that the WSS surface yields rate constants which are rather too low.

For interest's sake we decided to calculate the thermal rate constants which we

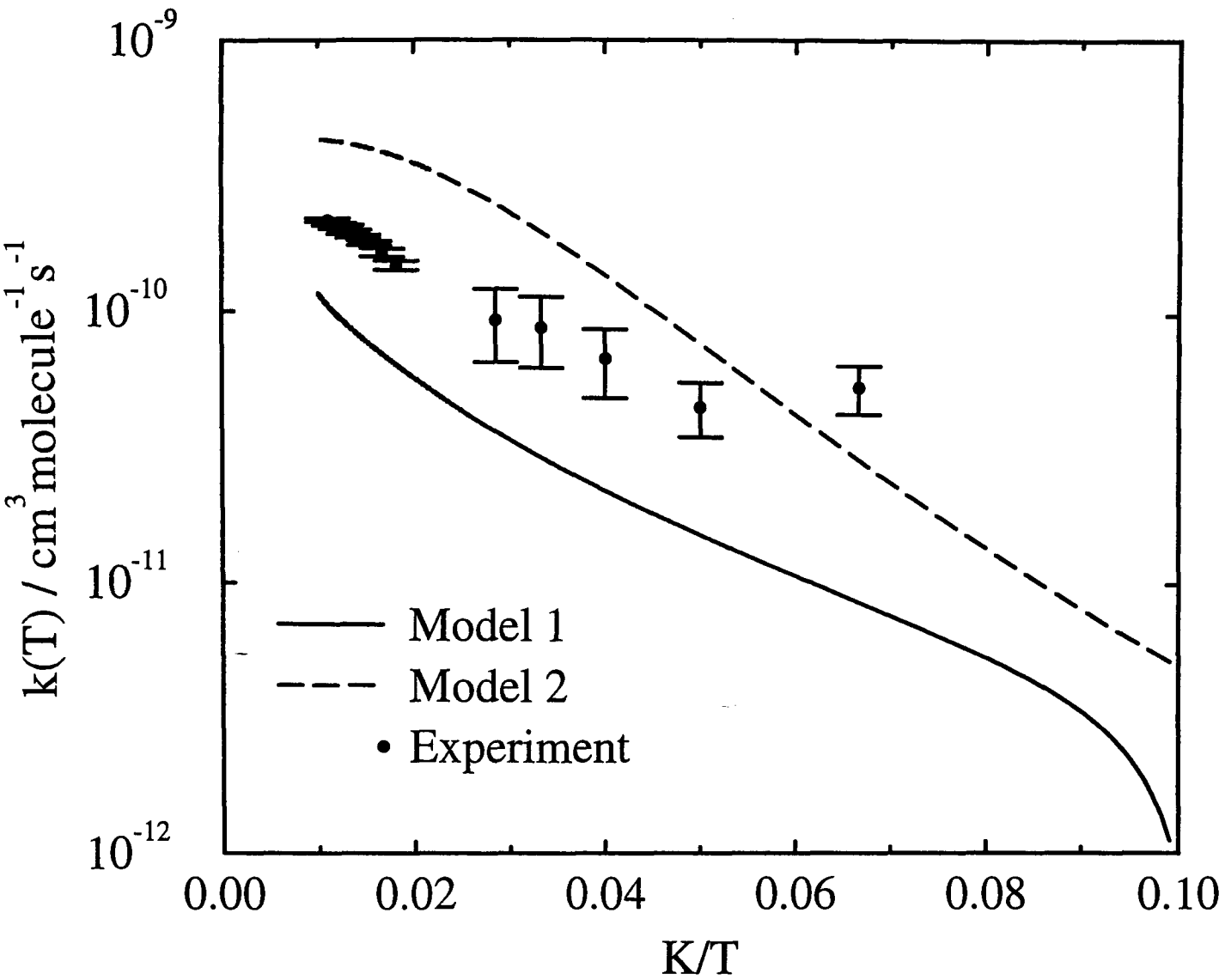


Figure 4.17 Approximate thermal rate constants for the $N^+ + n\text{-}H_2$ reaction with a simulated endothermicity of 17 meV, again calculated using two models for the effect of spin-orbit excitation and compared with Gerlich's experimental data [184].

obtain from our data if we shift the cross sections along the energy axis by -16 meV, such that we approximate a reaction endothermicity of 17 meV. The results of this calculation, again for the two models described above, are given in figure 4.17.

It is clear from figure 4.17 that the approximate thermal rate constants obtained for a reaction endothermicity of 17 meV are much closer to the experimental results than those shown in figure 4.16 for which the endothermicity was 33 meV. The effect of including or excluding spin-orbit energy can be seen by comparing the results of models 1 and 2, but it is not possible to determine which (if either) of these limiting

models is correct from these data. It is important to note in passing, however, that one can obtain some interesting differences in behaviour between models 1 and 2. For example, when model 2 is used in conjunction with a reaction endothermicity of 17 meV, the reaction from the initial state $N^+(^3P_1) + H_2(v = 0, j = 1)$ is exothermic, thus one can expect its rate constant to be around that of the Langevin value. In model 1, where spin-orbit energy is not available to promote the reaction, the reaction from this state is endothermic, and thus its rate constant in this model will be significantly smaller.

From the above discussion it should be clear that in order to be able to predict correctly the low-temperature rate constant of reaction (4.1) so as to determine its contribution to the formation of ammonia in dense interstellar clouds, it is essential to know the following:

- The exact endothermicity for the reaction,
- The effect of excited spin-orbit states on the rate of the reaction,
- The population distributions for the reactants under interstellar conditions (these can be strongly non-thermal).

It is also important to bear in mind that the work presented in this chapter is a single-surface calculation, and that multi-surface effects may be important for reaction (4.1). Further theoretical work will be needed in order to determine the importance of such phenomena.

To summarise our discussion, in this section we have explained the issues involved in calculating thermal rate constants for reaction (4.1) from the initial state-selected cross sections we calculated on the WSS surface. We presented two models for incorporating the effect of excited $N^+(^3P)$ spin-orbit states on the rate of the reaction,

and compared the results obtained from these models with some recent experimental data. Finally, we used an approximate method to simulate the results we might expect if the surface's endothermicity were 17 meV instead of 33 meV, and found that these results were closer to the experimental values, thus implying that the WSS surface's endothermicity of 33 meV is probably too high. This concludes our discussion of the calculation of thermal rate constants for reaction (4.1).

4.4 Conclusions

In this chapter we have presented the first fully quantum mechanical dynamics calculations on the reaction

$$N^+(^3P) + H_2(^1\Sigma_g^+) \longrightarrow NH^+(X^2\Pi) + H(^2S),$$

using the ground adiabatic potential energy surface of Wilhelmsson, Siegbahn and Schinke [193].

We began in section 4.1 with an overview of the literature for the reaction, both in the field of astrophysics and in chemical physics. Then, in section 4.2, we went on to describe the wavepacket method used in our calculations.

In section 4.3, we presented the results of the calculations. Initial state-selected reaction probabilities (ISSRPs) were given in section 4.3.1 for four different initial states of the reactants. These provided evidence for the importance of quantum mechanical resonances associated with the deep wells in the PES in determining the dynamics of the reaction.

From the ISSRPs we calculated initial state-selected cross sections, which we presented in section 4.3.2. The form of these cross sections was found to be strongly

dependent on the initial state. The cross sections for initial states from which the reaction is endothermic (*i.e.*, states with $v = 0$), show very different behaviour to those for states from which the reaction is exothermic (*i.e.*, states with $v = 1$), thus demonstrating the importance of energetic considerations in this nearly thermoneutral reaction. We also compared our cross sections with those calculated on the same WSS surface using a standard quasi-classical trajectory (QCT) method, and showed that the failure of the QCT method to treat vibrational zero-point energy correctly leads it to predict the wrong cross section behaviour in the threshold region. We concluded from this that it is essential to use a method (such as our quantum mechanical wavepacket method) which treats zero-point energy correctly in order to understand the dynamics of nearly-thermoneutral reactions.

We have also calculated initial state-selected rate constants from the cross sections and presented these in section 4.3.3. The rate constants from the states with $v = 0$ show a roughly Arrhenius-like behaviour, with the activation energy nearly equal to the endothermicity of the reaction from the initial state in question. The rate constants from the initial states with $v = 1$ are nearly independent of temperature, and correspond quite closely to the Langevin value.

Finally, in section 4.3.4, we discussed the issues involved in calculating *thermal* rate constants using the initial state-selected rate constants obtained in our wavepacket calculations. We explained the importance of determining the effect of excited spin-orbit states on the rate of the reaction, and proposed two limiting models for investigating this question. We compared the results we obtained using these models with some recent experimental data, and found that the endothermicity of the surface we used is probably too high.

For future work, we suggest that it will be important to determine the exact endothermicity of the reaction, and also to carry out an *ab initio* calculation in the reactant valley in order to determine which of the spin-orbit states of the $N^+(^3P)$ ion are reactive and which are not. Ultimately, a full multi-surface calculation will be needed in order to see how important non-adiabatic effects are for this reaction.

Chapter 5 Summary

In chapter 1 of this thesis we gave a brief introduction to the field of chemical dynamics. This was followed by a discussion of the Born-Oppenheimer approximation, and a brief overview of the different types of method which can be used in theoretical studies of chemical dynamics. The remaining part of this chapter consisted of a general introduction to the method which was used for the calculations presented in the subsequent chapters of the thesis: the quantum mechanical time-dependent wavepacket method.

The quantum mechanical theory of molecular photodissociation was presented in the first part of chapter 2. Starting from the Fermi Golden Rule expression for the absorption cross section of a molecule undergoing an electronic transition within the Born-Oppenheimer approximation, we derived a time-dependent expression for the absorption spectrum of a species undergoing a bound-continuum transition.

In the second part of chapter 2 we presented the quantum mechanical theory of reactive scattering. In particular, we derived a time-dependent expression for the S-matrix (placing particular emphasis on causality arguments), before introducing the flux formulation for the calculation of initial state-selected reaction probabilities (ISSRPs), and showing that this formulation for the ISSRP is equivalent to summing over appropriate S-matrix elements.

The final section of chapter 2 contained an introduction to reaction cross sections

and rate constants, and showed how these can be calculated from reaction probabilities. We concluded with a discussion of some approximate methods which can be used to carry out reactive scattering calculations for total angular momenta $J > 0$, describing the centrifugal sudden, optimum centrifugal sudden, and rotationally adiabatic approximations.

In chapter 3, the quantum mechanical time-dependent wavepacket theory of molecular photodissociation was applied to the calculation of the photodetachment spectrum of the FH_2^- anion. We began by introducing the concept of transition state spectroscopy, and then gave a brief overview of the literature of the $F + H_2$ reaction. After describing the method used in the calculations, we went on to present the results: photodetachment spectra for *o*-FH_2^- and *p*-FH_2^- calculated at two different energy resolutions.

The low-resolution FH_2^- spectra were found to reproduce results which have been obtained previously using a time-independent method, and to match the best available experimental spectra very successfully. These low-resolution spectra show broad peaks which are attributed to direct scattering states associated with $F + H_2$ hindered-rotor levels in the transition-state region of the neutral reaction. The high-resolution spectra reported in chapter 3 constitute the new results of this study. They show previously-unobserved narrow peaks superimposed onto the broad peaks of the low-resolution spectra. The high-resolution spectra were analysed by calculating energy-dependent wavefunctions corresponding to each peak in the spectrum. The broad peaks were assigned to direct scattering states, while the narrow peaks were shown to be due to quantum mechanical resonance states localised in the reactant and product valleys of the potential energy surface.

In the final section of chapter 3 we discussed briefly the work which has been carried out on the F + H_2 reaction since the publication of our work, and concluded with some suggestions for future work on this system.

In chapter 4 we presented an application of the quantum mechanical time-dependent wavepacket theory of reactive scattering to the nearly thermoneutral ion-molecule reaction

$$N^+(^3P) + H_2(^1\Sigma_g^+) \longrightarrow NH^+(X^2\Pi) + H(^2S).$$

We began with a review of the literature for this reaction, covering both its significance in the ongoing astrophysical debate concerning the interstellar synthesis of ammonia, and its interest to the chemical dynamics community. Having provided the motivation for the current work, we described the methodology used in our calculations before going on to present the results.

The results of this study were divided into three main sections: initial state-selected reaction probabilities (ISSRPs), cross sections, and rate constants. We calculated ISSRPs for four different rovibrational states of the reactant H_2 molecule. These were found to show a dense resonance structure as a function of energy, with the average width of the resonances depending on the initial state under study. The resonances were attributed to the influence of the deep wells in the potential energy surface on the dynamics of the reaction.

The initial state-selected cross sections were found to show a strong dependence on the initial state of the H_2, with the most important factor being whether the reaction is endothermic or exothermic from the initial state in question. A comparison of the cross section for the $(v = 0, j = 1)$ initial state obtained in our quantum mechanical

calculations with that obtained in an earlier quasiclassical trajectory (QCT) study showed that the QCT calculation gave the wrong behaviour for the cross section in the threshold region owing to its inability to treat vibrational zero-point energies correctly.

Our calculated initial state-selected rate constants for the $N^+ + H_2$ reaction were found to demonstrate the strong dependence of the rate of the reaction on the initial state of the reactants, and to suggest that rotational energy in the H_2 molecule is as efficient as relative translational energy in promoting the reaction. We also used these initial state-selected rate constants to calculate approximate thermal rate constants using two different models to account for the rôle of excited spin-orbit states of the $N^+(^3P)$ ion. A comparison of these calculated thermal rate constants with experimental data led us to conclude that the endothermicity of the surface used in our calculations is probably too high. Finally, chapter 4 ended with some suggestions for future work on the $N^+ + H_2$ reaction.

In summary, the quantum mechanical time-dependent wavepacket method has been presented in this thesis for calculations in the field of chemical dynamics, and two contrasting applications of the method to interesting chemical physics problems have been described.

Appendix A Absorbing potentials

Grid-based dynamics calculations such as those described in this thesis are carried out using a *finite* coordinate-space grid to simulate an event which, in reality, takes place in an *infinite* space. For example, in a real photodissociation event the photofragments can finish up at infinite separation from each other, and in a real reactive scattering event the reactants can approach each other from infinite separation and the products can disperse to infinite separation. However, in order to model these events computationally we must use a finite grid in coordinate space. It is this discrepancy between the physical reality and the need for something computationally viable which is the origin of the need for "absorbing potentials".

In a time-dependent wavepacket calculation, the problem of using a finite grid manifests itself in the fact that when the wavepacket (or part of it) reaches the end of the grid it will be reflected off what is essentially an infinite potential wall, and will thus re-enter the region of physical interest – the region in which $\psi(t)$ is being analysed to give information on the dynamics under study. Unphysical reflections of this nature invalidate the dynamics calculation and must thus be prevented: outgoing boundary conditions must be enforced.

The way in which this is commonly achieved in wavepacket calculations is by adding a coordinate-dependent absorbing potential (or "optical potential")

$$V_{\text{abs}} = -i\epsilon, \tag{A.1}$$

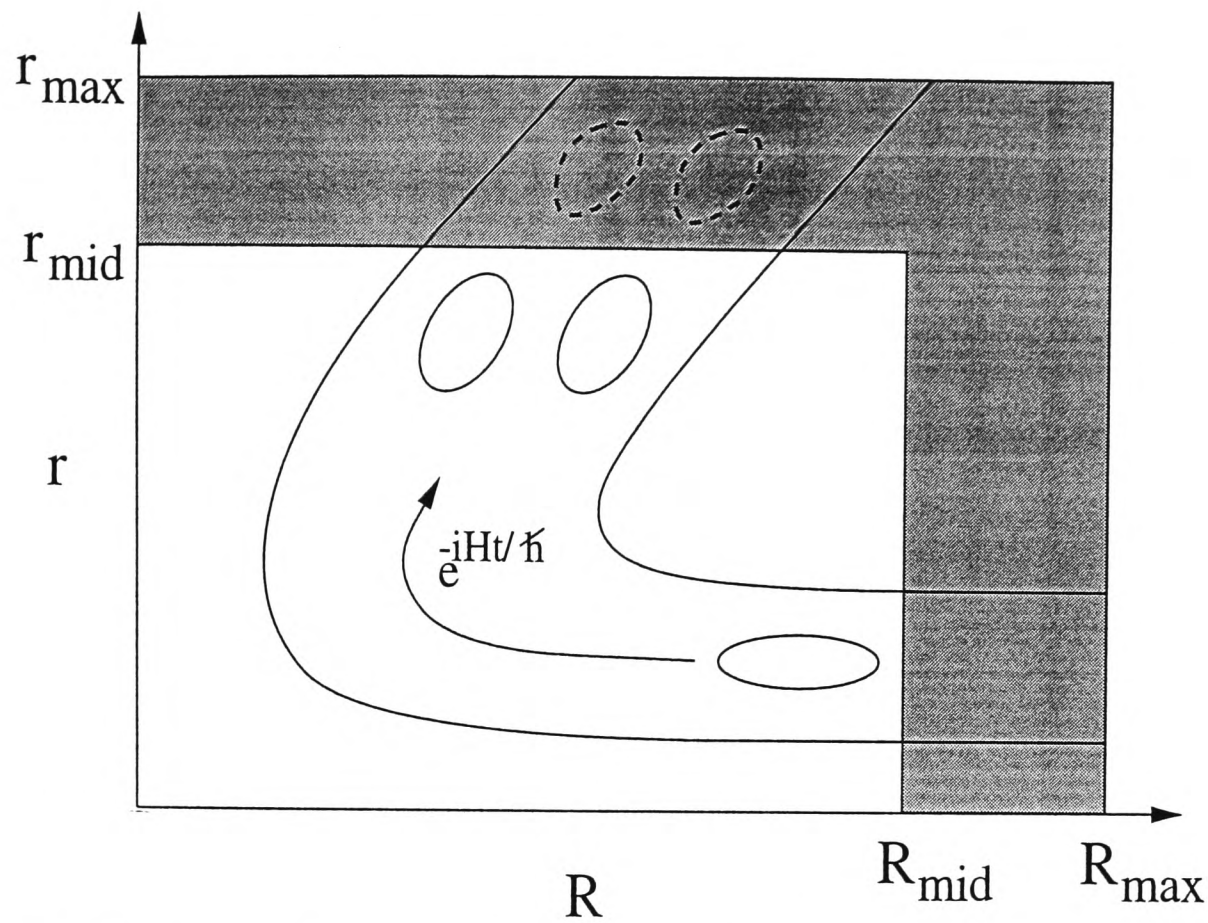


Figure A.1 Schematic diagram for a collinear atom plus diatom reaction to illustrate the absorption of the wavepacket by an absorbing potential (shown as the shaded region) before it reaches the edge of a finite grid in (Jacobi) coordinate space.

to the potential energy surface outside the region of physical interest (*i.e.*, at the edges of the coordinate-space grid), such that the time-propagation of the wavepacket becomes

$$|\psi(t+\Delta t)\rangle = e^{-i(H-i\epsilon)\Delta t/\hbar}|\psi(t)\rangle. \tag{A.2}$$

The absorbing potential acts as a damping factor, $e^{-\epsilon\Delta t/\hbar}$, on the wavepacket in the region of space over which ϵ is non-zero (see figure A.1), and thus ensures the convergence of the time-integral in equations such as (2.13), (3.2), (2.28) and (2.41), without interfering with the dynamics which are being studied.

The question of how to construct the absorbing potential for a particular application has been the subject of a considerable amount of work [212, 213, 214]. The components of the wavepacket with low translational energy (*i.e.*, long de Broglie

wavelengths) are more difficult to absorb than the fast-moving components, and the absorbing potential must be capable of absorbing over the whole energy range contained within the wavepacket. It must be strong enough to absorb the whole of the wavepacket before it is reflected, but in addition to this it must also turn on slowly enough such that the wavepacket does not get reflected off the absorbing potential itself. For the calculations which we describe in this thesis we use Manolopoulos' numerically-optimised absorbing potential [3], and in the following we describe briefly how this was obtained.

Consider the situation illustrated schematically in figure A.2, in which an incident wave, e^{+ikR}, is scattered off an infinite potential wall at R_{max}. In the absence of an absorbing potential, the probability of reflection as a function of translational energy, $|S(E_T)|^2$, is unity for all energies. However, if an absorbing potential is placed in front of the wall, we can expect this probability to decrease and, in the ideal case of a perfectly-efficient absorbing potential, to go to zero across the range of energies of interest. Therefore, in order to optimise the absorbing potential, Manolopoulos set up the calculation depicted in figure A.2, and numerically minimised the average reflection probability

$$P = \frac{1}{E_{T,\mathrm{max}}} \int_0^{E_{T,\mathrm{max}}} |S(E_T)|^2 \; dE_T, \tag{A.3}$$

with respect to the parameters in a suitably-chosen absorbing potential. Note that $E_{T,\mathrm{max}}$ is the maximum translational energy which must be absorbed.

After trying several functional forms for the absorbing potential, it was found that the best results were obtained using

$$\frac{V_{\mathrm{abs}}(R)}{E_{T,\mathrm{max}}} = V_R e^{-\alpha_R q(R)} + i V_I e^{-\alpha_I q(R)}, \tag{A.4}$$

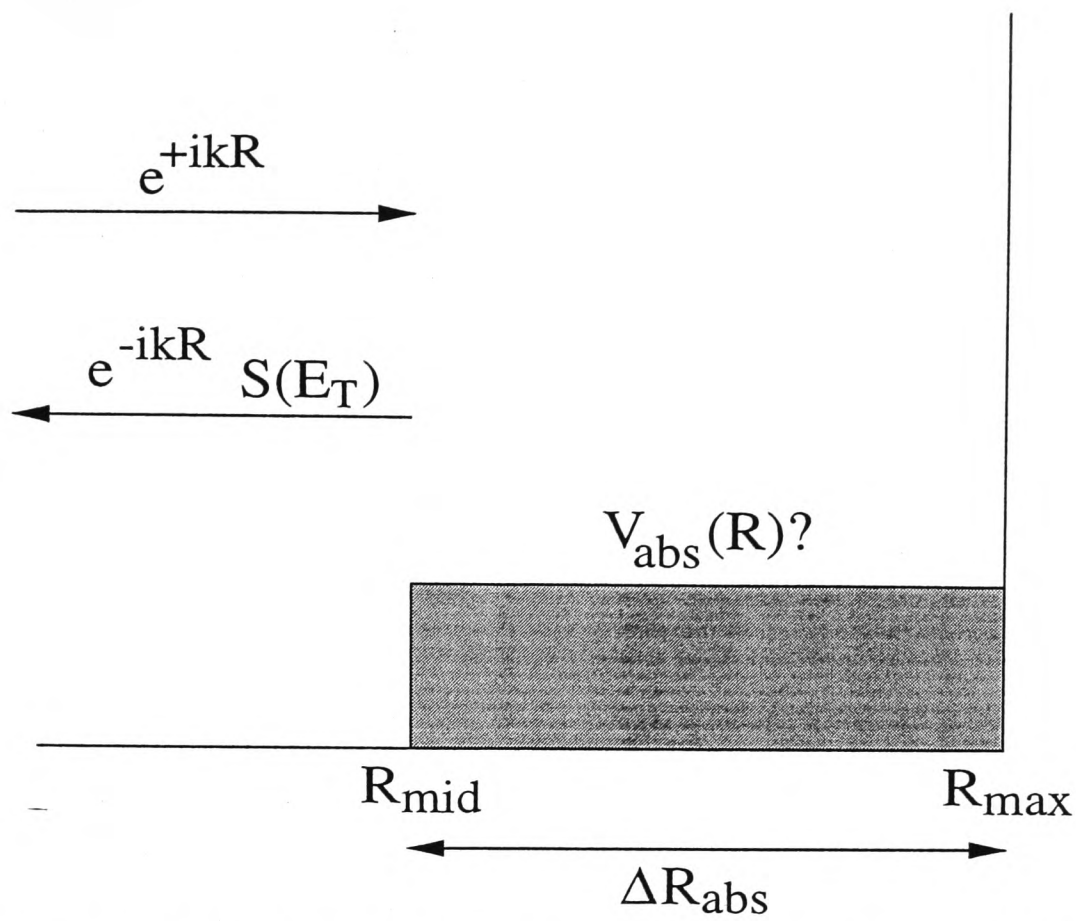


Figure A.2 Schematic diagram of the potential scattering calculation carried out in order to optimise V_{abs}.

where

$$q(R) = \frac{R_{\text{max}} - R}{R - R_{\text{mid}}}, \tag{A.5}$$

and R_{max} and R_{mid} are defined in figure A.2. The constraint was imposed that the parameters α_R and α_I must be positive, but V_R and V_I were allowed to take any values.

The resulting optimised parameters are given in table A.1, and the absorbing potential itself is shown in figure A.3. Note that in addition to the expected negative imaginary part to the potential there is also a negative real part. This helps in the absorption of the low-energy components of the wavepacket by speeding them up (and consequently decreasing their de Broglie wavelength), thus making it easier for the imaginary part to absorb them.

Figure A.4 shows the reflection properties of the optimised absorbing potential for

Parameter	Optimised value
V_R	-0.127
V_I	-0.994
α_R	0.739
α_I	3.071

Table A.1 Optimised parameters for the absorbing potential, V_{abs}, used in the calculations in this thesis.

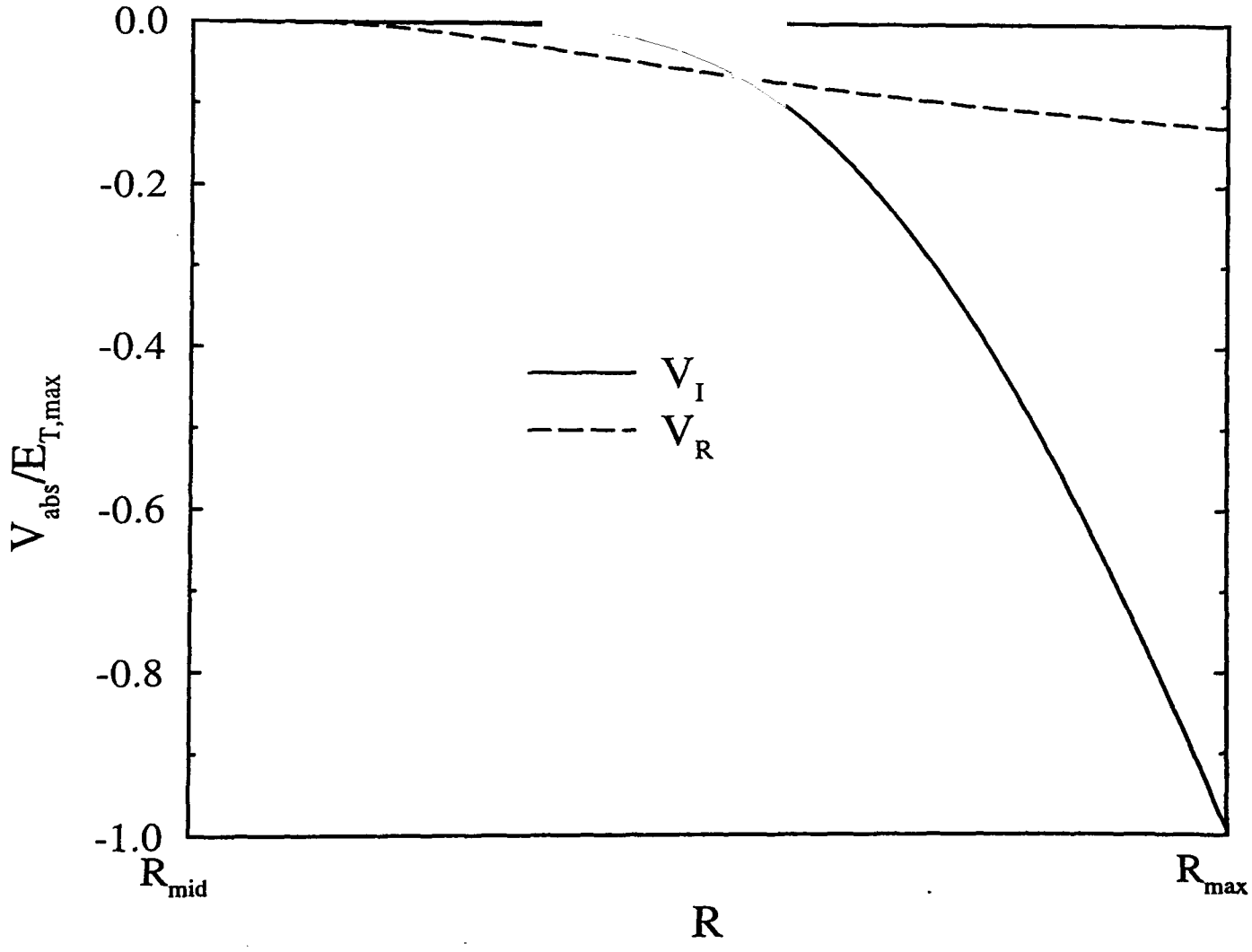


Figure A.3 Numerically-optimised complex absorbing potential used for the calculations in this thesis.

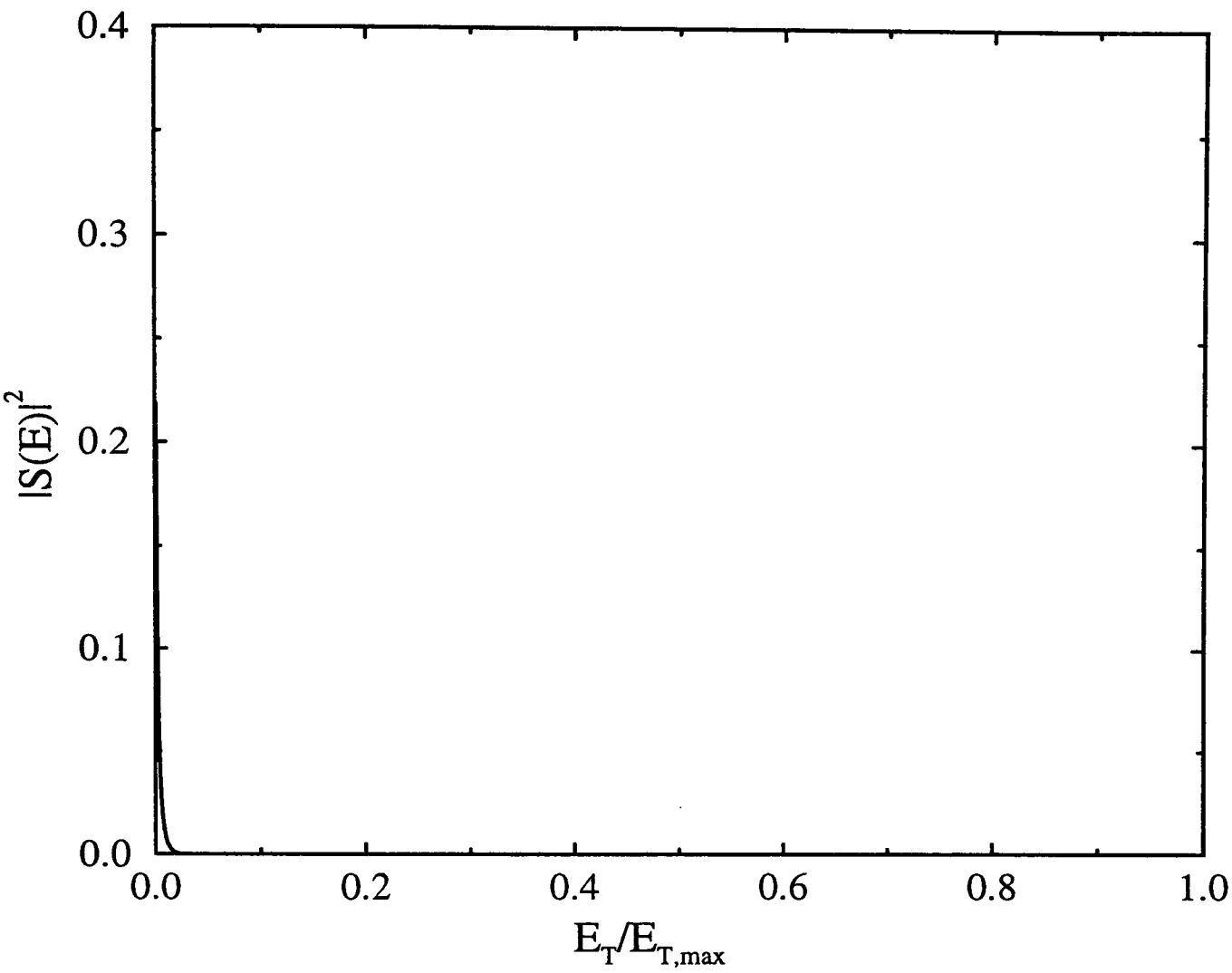


Figure A.4 The reflection probability from the numerically-optimised complex absorbing potential shown in figure A.3.

the case where ΔR_{abs} equals the de Broglie wavelength when $E_T = 0.2 \times E_{T,\text{max}}$. It is clear that the potential is perfectly absorbing over all but the very lowest energies, and of course its efficiency is increased simply by increasing the length of the absorbing strip, ΔR_{abs}.

We used the absorbing potential discussed in this appendix for all of the calculations presented in the thesis by applying it over the last 25% of the grids in R and r (see appendix B for a description of the Jacobi coordinates for a three-atom system). In this way, the convergence of the absorbing potential was ensured simply by converging the size of the radial grid.

Appendix B Jacobi coordinates for a three-atom system

Consider three atoms A, B, and C, which have masses m_τ (τ = A,B,C). The column vectors of the coordinates of the atoms relative to a laboratory-fixed origin are $\boldsymbol{x}_\tau$. After separation of the motion of the centre-of-mass of the system, the Jacobi coordinates, $(\tilde{\boldsymbol{R}}, \tilde{\boldsymbol{r}})$, for this system are [97]:

$$\tilde{\boldsymbol{R}}_\tau = \boldsymbol{x}_\tau - \frac{m_{\tau+1}\boldsymbol{x}_{\tau+1} + m_{\tau+2}\boldsymbol{x}_{\tau+2}}{m_{\tau+1} + m_{\tau+2}}, \tag{B.1}$$

$$\tilde{\boldsymbol{r}}_\tau = \boldsymbol{x}_{\tau+2} - \boldsymbol{x}_{\tau+1}, \tag{B.2}$$

where τ, $\tau+1$, and $\tau+2$ are cyclic permutations of A, B and C. The corresponding *mass-scaled* Jacobi coordinates, $(\boldsymbol{R}, \boldsymbol{r})$, are

$$\boldsymbol{R}_\tau = d_\tau \tilde{\boldsymbol{R}}_\tau, \tag{B.3}$$

$$\boldsymbol{r}_\tau = \frac{1}{d_\tau}\tilde{\boldsymbol{r}}_\tau, \tag{B.4}$$

where the dimensionless scaling factors are given by

$$d_\tau = \left[\frac{m_\tau}{\mu}\left(1 - \frac{m_\tau}{M}\right)\right]^{\frac{1}{2}}, \tag{B.5}$$

with

$$\mu = \left[\frac{m_A m_B m_C}{M}\right]^{\frac{1}{2}}, \tag{B.6}$$

and

$$M = m_A + m_B + m_C. \tag{B.7}$$

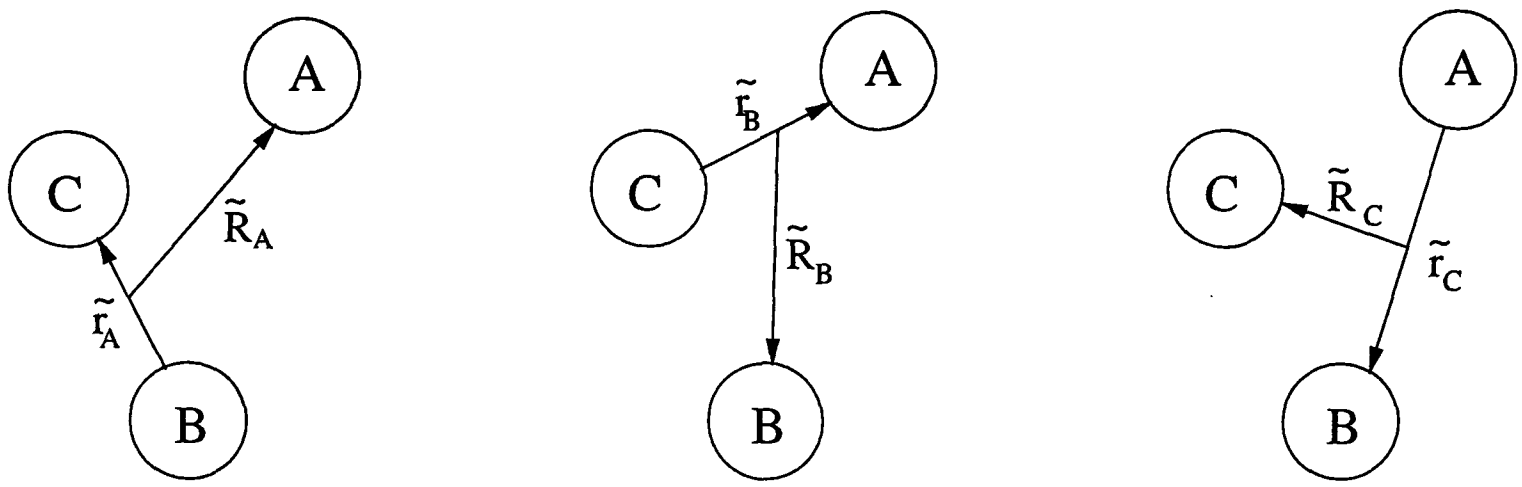


Figure B.1 The three sets of Jacobi coordinates for a particular configuration of atoms, for the case in which $m_A = m_B = m_C$.

Note that with atomic masses the scaling factors d_τ are always of the order of unity, and therefore that for the purposes of visualisation there is not much difference between the unscaled and the scaled coordinate systems. Figure B.1 illustrates the three sets of Jacobi coordinates for the system described above, and it is clear from this figure that the τth set of coordinates is the convenient coordinate system to use when the τth particle is a long way away from the other two.

Appendix C Energy levels of an asymmetric top

To carry out calculations on a triatomic system using the rotationally adiabatic approximation described in chapter 2, we need to find the rigid rotor energy levels associated with any particular geometrical arrangement of the three atoms. The Hamiltonian in the body-fixed frame for a rigid rotor is given by [215],

$$\hat{H} = \frac{\hat{J}_{x'}^2}{2I_{x'}} + \frac{\hat{J}_{y'}^2}{2I_{y'}} + \frac{\hat{J}_{z'}^2}{2I_{z'}}, \tag{C.1}$$

where $(\hat{J}_{x'},\hat{J}_{y'},\hat{J}_{z'})$ are the quantum-mechanical angular momentum operator components along the body-fixed axes (x', y', z') shown in figure 2.6, and $(I_{x'}, I_{y'}, I_{z'})$ are the moments of inertia associated with these axes. In order to diagonalise the Hamiltonian in equation (C.1) to find its energy eigenvalues we require the matrix elements of the squared angular momentum operators $\hat{J}_{x'}^2$, $\hat{J}_{y'}^2$, and $\hat{J}_{z'}^2$:

$$\begin{aligned}\left\langle JKM|\hat{J}_{x'}^2|J'K'M'\right\rangle &= \frac{\hbar^2}{2}\Big\{\left[J(J+1)-K^2\right]\delta_{KK'} \\ &+ \frac{1}{2}C_{JK}^{\mp}C_{JK\mp1}^{\mp}\delta_{KK'\pm2}\Big\}\delta_{JJ'}\delta_{MM'}, \end{aligned}\tag{C.2}$$

$$\begin{aligned}\left\langle JKM|\hat{J}_{y'}^2|J'K'M'\right\rangle &= \frac{\hbar^2}{2}\Big\{\left[J(J+1)-K^2\right]\delta_{KK'} \\ &- \frac{1}{2}C_{JK}^{\mp}C_{JK\mp1}^{\mp}\delta_{KK'\pm2}\Big\}\delta_{JJ'}\delta_{MM'}, \end{aligned}\tag{C.3}$$

$$\left\langle JKM|\hat{J}_{z'}^2|J'K'M'\right\rangle = \hbar^2K^2\delta_{KK'}\delta_{JJ'}\delta_{MM'}, \tag{C.4}$$

where $C_{ij}^{\mp}$ is defined in equation (2.75) and M is the quantum number for the projection of J along the space-fixed z axis. Note that M is a good quantum

J	K_a (Prolate top limit)	K_c (Oblate top limit)
0	0	0
1	1	0
	1	1
	0	1
2	2	0
	2	1
	1	1
	1	2
	0	2

Table C.1 Asymmetric top quantum numbers for total angular momenta $J \leq 2$.

number and that the $(2J + 1)$ states associated with the projection of the total angular momentum onto the space-fixed z axis are degenerate.

In contrast with the M quantum number, K (the quantum number for the projection of the total angular momentum along the body-fixed z' axis) is not a good quantum number, and therefore it is not possible to label rotational states of an asymmetric top by a K value. Instead we use (K_a, K_c) [216], where K_a is the value of $|K|$ in the limit of a prolate top, and K_c is the value of $|K|$ in the limit of an oblate top. Table C.1 shows the first few rotational states of an asymmetric top, and figure C.1 shows an energy level diagram for states with $J \leq 2$.

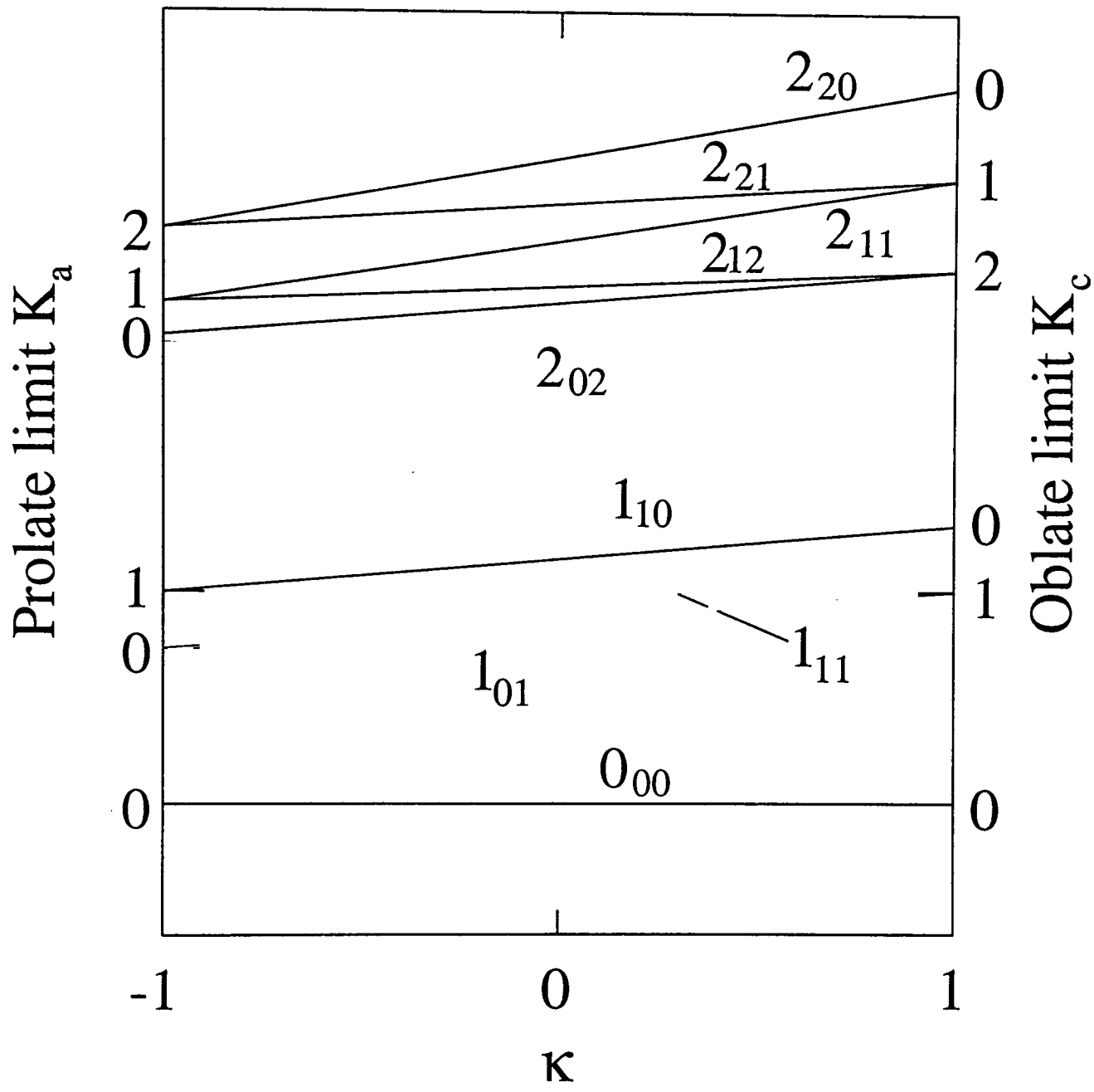


Figure C.1 Rotational levels, $J_{K_a K_c}$, of an asymmetric top as a function of the asymmetry parameter $\kappa = (2\tilde{B} - \tilde{A} - \tilde{C})/(\tilde{A} - \tilde{C})$, where $\tilde{A}$, $\tilde{B}$ and $\tilde{C}$ are the rotational constants associated with the a, b and c principal axes. (Adapted from Zare [216].)

References

[1] R.D.Levine and R.B.Bernstein, *Molecular reaction dynamics and chemical reactivity*, Oxford University Press, (1987).

[2] R.Schinke, *Photodissociation dynamics*, Cambridge University Press, Cambridge, (1993).

[3] D.E.Manolopoulos, *Quantum theory of molecular photodissociation*, Lecture notes from Charles Coulson Summer School in Theoretical Chemistry, Oxford, (1996).

[4] M.Head-Gordon, J. Phys. Chem. 100 (1996) 13213.

[5] P.Pechukas, J.C.Light and C.Rankin, J. Chem. Phys. 44 (1966) 794.

[6] W.H.Miller, J. Chem. Phys. 52 (1970) 543.

[7] M.Karplus, R.N.Porter and R.D.Sharma, J. Chem. Phys. 43 (1965) 3259.

[8] R.N.Porter and L.M.Raff in *Dynamics of molecular collisions, Part B*, ed. W.H.Miller, Plenum Press, New York, (1976), p. 1.

[9] F.J.Aoiz, L.Bañares and V.J.Herrero, J. Chem. Soc. Faraday Trans. 94 (1998) 2483.

[10] M.S.Child, *Semiclassical mechanics with molecular applications*, Oxford University Press, (1991).

[11] M.S.Child, *Molecular collision theory*, Dover Publications Inc., New York, (1996).

[12] D.C.Clary, Science 279 (1998) 1879.

[13] G.C.Schatz, J. Phys. Chem. 100 (1996) 12839.

[14] D.E.Manolopoulos in *Encyclopedia of computational chemistry, Vol. IV*, ed. H.F.Schaefer III, Wiley, (1998).

[15] N.Balakrishnan, C.Kalyanaraman and N.Sathyamurthy, Physics Reports 280 (1997) 79.

[16] E.J.Heller, Acc. Chem. Res. 14 (1981) 368.

[17] E.J.Heller, J. Chem. Phys. 68 (1978) 2066.

[18] K.C.Kulander and E.J.Heller, J. Chem. Phys. 69 (1978) 2439.

[19] E.J.Heller, J. Chem. Phys. 68 (1978) 3891.

[20] M.von Dirke and R.Schinke, Chem. Phys. Lett. 196 (1992) 51.

[21] M.von Dirke, B.Heumann, K.Kühl, T.Schröder and R.Schinke, J. Chem. Phys. 101 (1994) 2051.

[22] R.N.Dixon, J. Chem. Phys. 102 (1995) 301.

[23] M.L.Doublet, G.J.Kroes, E.J.Baerends and A.Rosa, J. Chem. Phys. 103 (1995) 2538.

[24] D.Y.Wang, W.Zhu, J.Z.H.Zhang and D.J.Kouri, J. Chem. Phys. 107 (1997) 751.

[25] F.Le Quéré and C.Leforestier, J. Chem. Phys. 94 (1991) 1118.

[26] N.Balakrishnan and G.D.Billing, J. Chem. Phys. 101 (1994) 2968.

[27] C.Leforestier, F.Lequere, K.Yamashita and K.Morokuma, J. Chem. Phys. 101 (1994) 3806.

[28] H.Flothmann, C.Beck, R.Schinke, C.Woywod and W.Domcke, J. Chem. Phys. 107 (1997) 7296.

[29] C.Y.Yang and S.K.Gray, J. Chem. Phys. 107 (1997) 7773.

[30] A.Loettgers, A.Untch, H.M.Keller, R.Schinke, H.-J.Werner, C.Bauer and P.Rosmus, J. Chem. Phys. 106 (1997) 3186.

[31] A.R.Offer and G.G.Balint-Kurti, J. Chem. Phys. 101 (1994) 10416.

[32] A.R.Offer and G.G.Balint-Kurti, Chem. Phys. Lett. 228 (1994) 200.

[33] A.R.Offer and G.G.Balint-Kurti, J. Chem. Phys. 105 (1996) 8615.

[34] A.R.Offer and G.G.Balint-Kurti, J. Chem. Phys. 104 (1996) 563.

[35] G.-J.Kroes, E.F.van Dishoeck, R.A.Beärda and M.C.van Hemert, J. Chem. Phys. 99 (1993) 228.

[36] R.A.Beärda, G.-J.Kroes, M.C.van Hemert, B.Heumann, R.Schinke and E.F.van Dishoeck, J. Chem. Phys. 100 (1994) 1113.

[37] G.-J.Kroes, M.C.van Hemert, G.D.Billing and D.Neuhauser, J. Chem. Phys. 107 (1997) 5757.

[38] G.-J.Kroes, M.C.van Hemert, G.D.Billing and D.Neuhauser, Chem. Phys. Lett. 271 (1997) 311.

[39] D.H.Zhang and J.Z.H.Zhang, J. Chem. Phys. 98 (1993) 6276.

[40] Z.T.Cai, D.H.Zhang and J.Z.H.Zhang, J. Chem. Phys. 100 (1994) 5631.

[41] E.A.McCullough Jr. and R.E.Wyatt, J. Chem. Phys. 51 (1969) 1253.

[42] D.H.Zhang and J.Z.H.Zhang, J. Chem. Phys. 101 (1994) 3671.

[43] J.Q.Dai and J.Z.H.Zhang, J. Phys. Chem. 100 (1996) 6898.

[44] J.Dai and J.Z.H.Zhang, J. Chem. Phys. 104 (1996) 3664.

[45] F.Gögtas, G.G.Balint-Kurti and A.R.Offer, J. Chem. Phys. 104 (1996) 7927.

[46] W.Zhu, D.Wang and J.Z.H.Zhang, Theor. Chem. Acc. 96 (1997) 31.

[47] T.Peng, D.H.Zhang, J.Z.H.Zhang and R.Schinke, Chem. Phys. Lett. 248 (1996) 37.

[48] J.Dai, J. Chem. Phys. 107 (1997) 4934.

[49] J.Z.H.Zhang, J.Dai and W.Zhu, J. Phys. Chem.A 101 (1997) 2746.

[50] D.C.Clary, J. Phys. Chem. 98 (1994) 10678, and references therein.

[51] S.K.Pogrebnya, J.Echave and D.C.Clary, J. Chem. Phys. 107 (1997) 8975, and references therein.

[52] D.H.Zhang and J.Z.H.Zhang, J. Chem. Phys. 99 (1993) 5615.

[53] D.H.Zhang and J.Z.H.Zhang, J. Chem. Phys. 100 (1994) 2697.

[54] D.Neuhauser, J. Chem. Phys. 100 (1994) 9272.

[55] D.H.Zhang and J.Z.H.Zhang, J. Chem. Phys. 101 (1994) 1146.

[56] J.Dai, W.Zhu and J.Z.H.Zhang, J. Phys. Chem. 100 (1996) 13901.

[57] W.Zhu, J.Dai, J.Z.H.Zhang and D.H.Zhang, J. Chem. Phys. 105 (1996) 4881.

[58] D.H.Zhang and J.Z.H.Zhang, Chem. Phys. Lett. 232 (1995) 370.

[59] D.H.Zhang, J.Z.H.Zhang, Y.Zhang, D.Wang and Q.Zhang, J. Chem. Phys. 102 (1995) 7400.

[60] Y.Zhang, D.Zhang, W.Li, Q.Zhang, D.Wang, D.H.Zhang and J.Z.H.Zhang, J. Phys. Chem. 99 (1995) 16824.

[61] D.H.Zhang and J.C.Light, J. Chem. Phys. 104 (1996) 4544.

[62] D.H.Zhang and J.C.Light, J. Chem. Phys. 105 (1996) 1291.

[63] D.H.Zhang and J.C.Light, J. Chem. Soc. Faraday Trans. 93 (1997) 691.

[64] E.M.Goldfield, S.K.Gray and G.C.Schatz, J. Chem. Phys. 102 (1995) 8807.

[65] D.H.Zhang and J.Z.H.Zhang, J. Chem. Phys. 103 (1995) 6512.

[66] W.Zhu, J.Z.H.Zhang, Y.C.Zhang, Y.B.Zhang, L.X.Zhan and S.L.Zhang, J. Chem. Phys. 108 (1998) 3509.

[67] E.M.Goldfield and S.K.Gray, J. Chem. Soc. Faraday Trans. 93 (1997) 909.

[68] P.J.Krause and D.C.Clary, Mol. Phys. 93 (1998) 619.

[69] G.J.Kroes, E.J.Baerends and R.C.Mowrey, J. Chem. Phys. 107 (1997) 3309.

[70] J.Dai and J.C.Light, J. Chem. Phys. 107 (1997) 1676.

[71] J.Dai and J.C.Light, J. Chem. Phys. 108 (1998) 7816.

[72] E.Fermi, *Nuclear physics*, University of Chicago Press, Chicago, (1950), p. 142.

[73] R.G.Gordon, Adv. Magn. Res. 3 (1968) 1.

[74] A.Kuppermann and G.C.Schatz, J. Chem. Phys. 65 (1976) 4668.

[75] M.P.de Miranda and D.C.Clary, J. Chem. Phys. 106 (1997) 4506.

[76] J.R.Taylor, *Scattering theory*, Wiley, New York, (1972).

[77] R.G.Newton, *Scattering theory of waves and particles*, McGraw-Hill, New York, (1966).

[78] D.J.Tannor and D.E.Weeks, J. Chem. Phys. 98 (1993) 3884.

[79] D.J.Kouri, Y.H.Huang, W.Zhu and D.K.Hoffman, J. Chem. Phys. 100 (1994) 3662.

[80] G.J.Kroes and D.Neuhauser, J. Chem. Phys. 105 (1996) 8690.

[81] C.W.McCurdy, T.N.Rescigno, W.A.Isaacs and D.E.Manolopoulos, Phys. Rev. A, 57 (1998) 3511.

[82] L.I.Schiff, *Quantum mechanics*, McGraw-Hill, pp.25-27, (1949).

[83] W.H.Miller, J. Chem. Phys. 61 (1974) 1823.

[84] W.H.Miller, S.D.Schwartz and J.W.Tromp, J. Chem. Phys. 79 (1983) 4889.

[85] M.S.Child in *Modern gas kinetics: Theory, experiment and application*, ed. M.J.Pilling and I.W.M.Smith, Blackwell Scientific Publications (1987).

[86] G.Giomousis and D.P.Stevenson, J. Chem. Phys. 29 (1958) 294.

[87] J.M.Bowman, J. Phys. Chem. 95 (1991) 4960.

[88] R.T Pack, J. Chem. Phys. 60 (1974) 633.

[89] G.C.Schatz and A.Kuppermann, J. Chem. Phys. 65 (1976) 4642.

[90] C.W.McCurdy and W.H.Miller, ACS Symposium Series, ed. P.R.Brooks and E.F.Hayes, American Chemical Society, Washington D.C., 56 (1977) pp. 239-242.

[91] J.M.Bowman, Chem. Phys. Lett. 217 (1994) 36.

[92] J.Qi and J.M.Bowman, J. Chem. Phys. 105 (1996) 9884.

[93] D.Wang and J.M.Bowman, J. Phys. Chem. 98 (1994) 7994.

[94] J.Qi and J.M.Bowman, J. Chem. Phys. 107 (1997) 9960.

[95] F.N.Dzegilenko and J.M.Bowman, J. Chem. Phys. 108 (1998) 511.

[96] J.M.Bowman, J. Phys. Chem. 102 (1998) 3006.

[97] R.T Pack and G.A.Parker, J. Chem. Phys. 87 (1987) 3888.

[98] D.M.Brink and G.R.Satchler, *Angular momentum*, Oxford Science Publications, Clarendon Press, Oxford, (1994).

[99] D.De Fazio and J.F.Castillo, to be published.

[100] C.L.Russell and D.E.Manolopoulos, Chem. Phys. Lett. 256 (1996) 465.

[101] D.M.Neumark, Ann. Rev. Phys. Chem. 43 (1992) 153.

[102] L.J.Butler and D.M.Neumark, J. Phys. Chem. 100 (1996) 12801.

[103] A.Weaver and D.M.Neumark, Faraday Discuss. Chem. Soc. 91 (1991) 5.

[104] S.E.Bradforth, A.Weaver, D.W.Arnold, R.B.Metz and D.M.Neumark, J. Chem. Phys. 92 (1990) 7205.

[105] R.B.Metz, A.Weaver, S.E.Bradforth, T.N.Kitsopoulos and D.M.Neumark, J. Phys. Chem. 94 (1990) 1377.

[106] D.E.Manolopoulos, J. Chem. Soc., Faraday Trans. 93 (1997) 673.

[107] S.E.Bradforth, D.W.Arnold, D.M.Neumark and D.E.Manolopoulos, J. Chem. Phys. 99 (1993) 6345.

[108] D.E.Manolopoulos, K.Stark, H.-J.Werner, D.W.Arnold, S.E.Bradforth and D.M.Neumark, Science 262 (1993) 1852.

[109] M.Faubel, L.Rusin, S.Schlemmer, F.Sondermann, U.Tappe and J.P.Toennies, J. Chem. Phys. 101 (1994) 2106.

[110] M.Faubel, B.Martinez-Haya, L.Y.Rusin, U.Tappe and J.P.Toennies, Chem. Phys. Lett. 232 (1995) 197.

[111] K.Stark and H.-J.Werner, J. Chem. Phys. 104 (1996) 6515.

[112] J.Z.H.Zhang and W.H.Miller, J. Chem. Phys. 92 (1990) 1811.

[113] F.J.Aoiz, L.Banares, V.J.Herrero, V.Saez Rabanos, K.Stark and H.-J.Werner, Chem. Phys. Lett. 223 (1994) 215.

[114] F.J.Aoiz, L.Banares, V.J.Herrero, V.Saez Rabanos, K.Stark and H.-J.Werner, J. Phys. Chem. 98 (1994) 10665.

[115] F.J.Aoiz, L.Banares, V.J.Herrero, V.Saez Rabanos, K.Stark and H.-J.Werner, J. Chem. Phys. 102 (1995) 9248.

[116] F.J.Aoiz, L.Banares, V.J.Herrero, K.Stark and H.-J.Werner, Chem. Phys. Lett. 254 (1996) 341.

[117] M.Baer, M.Faubel, B.Martinez-Haya, L.Y.Rusin, U.Tappe, J.P.Toennies, K.Stark and H.-J.Werner, J. Chem. Phys. 104 (1996) 2743.

[118] J.F.Castillo, D.E.Manolopoulos, K.Stark and H.-J.Werner, J. Chem. Phys. 104 (1996) 6531.

[119] G.C.Schatz, Science 262 (1993) 1828.

[120] D.M.Neumark, A.M.Wodtke, G.N.Robinson, C.C.Hayden and Y.T.Lee, J. Chem. Phys. 82 (1985) 3045.

[121] J.C.Nieh and J.J.Valentini, Phys. Rev. Letters 60 (1988) 519.

[122] J.Z.H.Zhang and W.H.Miller, Chem. Phys. Lett. 153 (1988) 465.

[123] D.A.V.Kliner, D.E.Adelman and R.N.Zare, J. Chem. Phys. 94 (1991) 1069.

[124] W.H.Miller and J.Z.H.Zhang, J. Phys. Chem. 95 (1991) 12.

[125] D.C.Clary and J.N.L.Connor, J. Phys. Chem. 88 (1984) 2758.

[126] G.C.Schatz, J. Chem. Phys. 90 (1989) 4847.

[127] B.Gazdy and J.M.Bowman, J. Chem. Phys. 91 (1989) 4615.

[128] I.M.Waller, T.N.Kitsopoulos and D.M.Neumark, J. Phys. Chem. 94 (1990) 2241.

[129] J.A.Nichols, R.A.Kendall, S.J.Cole and J.Simons, J. Phys. Chem. 95 (1991) 1074.

[130] G.C.Schatz, J. Phys. Chem. 94 (1990) 6157.

[131] D.T.Colbert and W.H.Miller, J. Chem. Phys. 96 (1992) 1982.

[132] M.D.Feit and J.A.Fleck, J. Chem. Phys. 78 (1983) 301.

[133] W.H.Press, S.A.Teukolsky, W.T.Vetterling and B.P.Flannery, *Numerical recipes in FORTRAN: the art of scientific computing*, Cambridge University Press, (1992).

[134] M.J.Davis, H.Koizumi, G.C.Schatz, S.E.Bradforth and D.M.Neumark, J. Chem. Phys. 101 (1994) 4708.

[135] J.D.Kress and E.F.Hayes, J. Chem. Phys. 97 (1992) 4881.

[136] A.Persky and H.Kornweitz, Int. J. Chem. Kinetics 29 (1997) 67.

[137] G.Dharmasena, T.R.Phillips, K.N.Shokhirev, G.A.Parker and M.Keil, J. Chem. Phys. 106 (1997) 9950.

[138] G.Dharmasena, K.Copeland, J.H.Young, R.A.Lasell, T.R.Phillips, G.A.Parker and M.Keil, J. Phys. Chem.A 101 (1997) 6429.

[139] W.B.Chapman, B.W.Blackmon and D.J.Nesbitt, J. Chem. Phys. 107 (1997) 8193.

[140] M.Faubel, B.MartinezHaya, L.Y.Rusin, U.Tappe and J.P.Toennies, J. Phys. Chem.A 101 (1997) 6415.

[141] F.J.Aoiz, M.Brouard, V.J.Herrero, V.S.Rabanos and K.Stark, Chem. Phys. Lett. 264 (1997) 487.

[142] F.J.Aoiz, L.Banares, B.MartinezHaya, J.F.Castillo, D.E.Manolopoulos, K.Stark and H.J.Werner, J. Phys. Chem.A 101 (1997) 6403.

[143] R.T.Skodje, R.Sadeghi and J.L.Krause, J. Chem. Soc. Faraday Trans. 93 (1997) 765.

[144] K.A.Peterson and T.H.Dunning, Jr., J. Phys. Chem.A 101 (1997) 6280.

[145] M.Founargiotakis, S.C.Farantos, Ch.Skokos and G.Contopoulos, Chem. Phys. Lett. 277 (1997) 456.

[146] G.C.Lynch, R.Steckle, D.W.Schwenke, A.J.C.Varandas, D.G.Truhlar and B.C.Garrett, J. Chem. Phys. 94 (1991) 7136.

[147] B.Hartke and H.-J.Werner, Chem. Phys. Lett. 280 (1997) 430.

[148] B.Hartke, K.Stark and H.-J.Werner, in preparation.

[149] M.H.Alexander, H.-J.Werner and D.E.Manolopoulos, accepted for publication in J. Chem. Phys..

[150] C.L.Russell and D.E.Manolopoulos, accepted for publication in J. Chem. Phys..

[151] G.A.Blake, G.Sandell, E.F.Van Dishoeck, T.D.Groesbeck, L.G.Mundy and C.Aspin, Astrophys. J. 441 (1995) 689.

[152] E.Herbst, Ann. Rev. Phys. Chem. 46 (1995) 27.

[153] W.Klemperer, Ann. Rev. Phys. Chem. 46 (1995) 1.

[154] E.A.Bergin and W.D.Langer, Astrophys. J. 486 (1997) 316.

[155] L.A.M.Nejad, D.A.Williams and S.B.Charnley, Mon. Not. R. Astr. Soc. 246 (1990) 183.

[156] E.Herbst and W.Klemperer, Astrophys. J. 185 (1973) 505.

[157] G.B.I.Scott, C.G.Freeman and M.J.McEwan, Mon. Not. R. Astr. Soc. 290 (1997) 636.

[158] E.T.Galloway and E.Herbst, Astron. Astrophys. 211 (1989) 413.

[159] E.Herbst, D.J.DeFrees and A.D.McLean, Astrophys. J. 321 (1987) 898.

[160] J.H.Yee, S.Lepp and A.Dalgarno, Mon. Not. R. Astr. Soc. 227 (1987) 461.

[161] J.Le Bourlot, Astron. Astrophys. 242 (1991) 235.

[162] N.G.Adams, D.Smith and T.J.Millar, Mon. Not. R. Astr. Soc. 211 (1984) 857.

[163] E.Herbst and C.M.Leung, Mon. Not. R. Astr. Soc. 222 (1986) 689.

[164] E.Herbst and C.M.Leung, Astrophys. J. 310 (1986) 378.

[165] G.B.I.Scott, D.A.Fairley, C.G.Freeman and M.J.McEwan, Chem. Phys. Lett. 269 (1997) 88.

[166] A.Dalgarno, *Interaction between ions and molecules*, Plenum Press, New York, (1975).

[167] G.Pineau des Forets, E.Roueff and D.R.Flowers, Mon. Not. R. Astr. Soc. 244 (1990) 668.

[168] T.R.Geballe and T.Oka, Nature 384 (1996) 334.

[169] F.C.Fehsenfeld, A.L.Schmeltekopf and E.E.Ferguson, J. Chem. Phys. 46 (1967) 2802.

[170] W.T.Huntress Jr., Astrophys. J. Suppl. Ser. 33 (1977) 495.

[171] M.Tichy, A.B.Rakshit, D.G.Lister, N.D.Twiddy, N.G.Adams and D.Smith, Int. J. Mass Spectrom. Ion Phys. 29 (1979) 231.

[172] N.G.Adams and D.Smith, Chem. Phys. Lett. 117 (1985) 67.

[173] K.M.Ervin and P.B.Armentrout, J. Chem. Phys. 86 (1987) 2659.

[174] R.Tarroni, P.Palmieri, A.Mitrushenkov, P.Tosi and D.Bassi, J. Chem. Phys. 106 (1997) 10265, and references therein..

[175] W.R.Anderson, J. Phys. Chem. 93 (1989) 530.

[176] K.Kawaguchi and T.Amano, J. Chem. Phys. 88 (1988) 4584.

[177] E.A.Gislason, B.H.Mahan, C.W.Tsao and A.S.Werner, J. Chem. Phys. 54 (1971) 3897.

[178] J.A.Fair and B.H.Mahan, J. Chem. Phys. 62 (1975) 515.

[179] J.M.Farrar, S.G.Hansen and B.H.Mahan, J. Chem. Phys. 65 (1976) 2908.

[180] B.H.Mahan and W.E.W.Ruska, J. Chem. Phys. 65 (1976) 5044.

[181] S.G.Hansen, J.M.Farrar and B.H.Mahan, J. Chem. Phys. 73 (1980) 3750.

[182] J.B.Marquette, C.Rebrion and B.R.Rowe, J. Chem. Phys. 89 (1988) 2041.

[183] P.Tosi, O.Dmitriev, D.Bassi, O.Wick and D.Gerlich, J. Chem. Phys. 100 (1994) 4300.

[184] D.Gerlich, J. Chem. Soc. Faraday Trans. 89 (1993) 2199.

[185] L.S.Sunderlin and P.B.Armentrout, J. Chem. Phys. 100 (1994) 5639.

[186] P.Tosi, Chem. Rev. 92 (1992) 1667.

[187] D.C.Clary, Mol. Phys. 53 (1984) 3.

[188] M.A.Gittins and D.M.Hirst, Chem. Phys. Lett. 35 (1975) 534.

[189] M.A.Gittins, D.M.Hirst and M.F.Guest, Faraday Discuss. Chem. Soc. 62 (1977) 67.

[190] C.F.Bender, J.H.Meadows and H.F.Schaefer III, Faraday Discuss. Chem. Soc. 62 (1977) 59.

[191] S.D.Peyerimhoff and R.J.Buenker, Chem. Phys. 42 (1979) 167.

[192] D.M.Hirst, Mol. Phys. 35 (1978) 1559.

[193] U.Wilhelmsson, P.E.M.Siegbahn and R.Schinke, J. Chem. Phys. 96 (1992) 8202.

[194] M.A.Gittins and D.M.Hirst, Chem. Phys. Lett. 65 (1979) 507.

[195] K.S.Sorbie and J.N.Murrell, Mol. Phys. 29 (1975) 1387.

[196] M.Gonzalez, A.Aguilar and R.Sayos, Chem. Phys. 132 (1989) 137.

[197] M.Gonzalez, A.Aguilar and Y.Fernandez, Chem. Phys. 104 (1986) 57.

[198] M.Gonzalez, A.Aguilar and Y.Fernandez, Chem. Phys. 106 (1986) 477.

[199] M.Gonzalez, A.Aguilar and J.Virgili, Chem. Phys. Lett. 113 (1985) 179.

[200] U.Wilhelmsson and G.Nyman, J. Chem. Phys. 96 (1992) 1886.

[201] G.Nyman and U.Wilhelmsson, J. Chem. Phys. 96 (1992) 5198.

[202] D.Gerlich, J. Chem. Phys. 90 (1989) 3574.

[203] G.Nyman, J. Chem. Phys. 96 (1992) 3603.

[204] T.J.Millar, P.R.Ã.Farquhar and K.Willacy, Astron. Astrophys. 121 (1997) 139.

[205] J.A.Luine and G.H.Dunn, Astrophys. J. 299 (1985) L67.

[206] D.R.Bates, Phys. Rev. A 34 (1986) 1878.

[207] J.B.Marquette, B.R.Rowe, G.Dupeyrat and E.Roueff, Astron. Astrophys. 147 (1985) 115.

[208] J.Echave and D.C.Clary, Chem. Phys. Lett. 190 (1992) 225.

[209] Y.Guo, D.L.Thompson and T.D.Sewell, J. Chem. Phys. 104 (1996) 576.

[210] K.J.Laidler, *Chemical kinetics: Third edition*, Harper Collins, (1987).

[211] D.C.Clary, C.E.Dateo and D.Smith, Chem. Phys. Lett. 167 (1990) 1.

[212] D.Neuhauser and M.Baer, J. Chem. Phys. 90 (1989) 4351.

[213] M.Child, Mol. Phys. 72 (1991) 89.

[214] T.Seideman and W.H.Miller, J. Chem. Phys. 96 (1992) 4412.

[215] W.J.Thompson, *Angular momentum: An illustrated guide to rotational symmetries for physical systems*, Wiley Interscience, (1994).

[216] R.N.Zare, *Angular momentum: Understanding spatial aspects in chemistry and physics*, Wiley Interscience, (1987).